Title
Interacting Ultracold Bosonic Atoms in Geometrically Frustrated Lattices

Author
Leung, Tsz Him

Publication Date
2020

Peer reviewed|Thesis/dissertation

Interacting Ultracold Bosonic Atoms in Geometrically Frustrated Lattices

by

Tsz Him Leung

A dissertation submitted in partial satisfaction of the

requirements for the degree of

Doctor of Philosophy

in

Physics

in the

Graduate Division

of the

University of California, Berkeley

Committee in charge:

Professor Dan Stamper-Kurn, Chair
Professor Ehud Altman
Professor Markita del Carpio Landry

Fall 2020

Interacting Ultracold Bosonic Atoms in Geometrically Frustrated Lattices

Abstract

Interacting Ultracold Bosonic Atoms in Geometrically Frustrated Lattices

by

Tsz Him Leung

Doctor of Philosophy in Physics

University of California, Berkeley

Professor Dan Stamper-Kurn, Chair

Geometric frustration is a phenomenon where local energy constraints cannot be simultaneously satisfied because of geometric reasons. This leads to a manifold of degenerate ground states in which ordering can be highly nontrivial and exotic phases of matter could emerge. In a kagome lattice, both interaction energies of spins and kinetic energies of particles can be frustrated. In the latter case, a single-particle band structure with a flat (dispersionless) energy band results.

In this dissertation, we report our experimental studies of interacting bosonic systems in kagome lattices. Such studies are performed with a quantum simulator based on ultracold atoms in optical lattices. We describe upgrades and development of the apparatus that constructs optical kagome lattices in our experiment. We briefly discuss results of an experiment studying the Bose-Hubbard model in a trimerized kagome lattice. We then report the details of an experiment investigating the interplay of kinetic frustration and interactions by probing the band structure of an optical kagome lattice with interacting ultracold bosonic atoms. Finally, we propose experimental ideas for exploring the properties of the singular band touching point in the kagome flat band.

Contents

List of Figures

List of Tables

Acknowledgments

First and foremost, I would like to thank my advisor Dan Stamper-Kurn. Everyone knows how smart and how good a physicist he is. I have the privilege of being his student, and what I see in him is not only an exemplary physicist, but also a patient, understanding and encouraging advisor. I am extremely grateful for the time and room he has given me to grow.

I would also like to thank everyone who worked on E5 with me. Special thanks go to Claire Thomas and Thomas Barter, the two graduates who mentored me during my junior years. Claire gave me a lot of pro tips on various subjects ranging from soldering, aligning optics to going on a date. I remember the one time when I had a really bad day in my first year of grad school, and I walked into the lab to tell Claire what I went through hoping to receive some condolences. "It's okay Zephy. It will get worse. This is just the beginning of your grad school," said Claire. Such words of wisdom became my motto and gave me mental strength to finish my PhD. Tom had a great influence on my way of thinking. Through our daily conversation and collaboration over the course of five years, I learned how to think and argue like a physicist from him. To both of you, thank you for having faith and confidence in me, even when I was struggling so bad at the beginning of my PhD. Also, thank you for not killing me when I accidentally deleted all the experimental settings and sequences on the control computer (later recovered by Tom).

To new graduate students Malte Schwarz and Shao Wen Chang, visiting students Vincent Klinkhamer, Severin Daiss, Luca Bayha, Yee Ming Tso and Govind Unnikrishnan, postdocs Masayuki Okano and Charles Brown, thank you for making the lab a fun place to work and a stimulating environment to learn. To some of you, thank you for sharing my passion for boba.

Throughout my PhD, literally everyone I met in the Stamper-Kurn group is friendly, helpful and supportive. Thank you all for the help, advice and suggestions you offered me when I needed them, and all the lenses and IR cards that I borrowed but never returned.

To all my friends I met at Berkeley, thank you for the laughter we have shared. To all my friends in Hong Kong, thank you for keeping me feel connected to the place I belong.

To my family, thank you for your unconditional support. I have never managed to explain very well what ultracold atoms and optical lattices are to them. But they never doubt my decision to travel to a place 11 thousand kilometers (fine, 7 thousand miles) away to study something that sounds strange. Thank you for letting me know no matter what there is always a place for me to go back to.

At last, I want to thank a special one who loved and supported me in my final years of grad school in her unique way. She has been by my side through my downs and further downs (there are no ups in grad school). Thank you, Emily Chung.

Chapter 1

Introduction

In this introductory chapter, we present the main themes of the research work reported in this dissertation, namely geometric frustration and flat bands. We also describe how a quantum simulator based on ultracold atoms and optical lattices works and is used in our experiment.

1.1 Geometric frustration and flat band

Geometric Frustration

Geometric frustration is a phenomenon where a system fails to minimize local energy constraints simultaneously because of geometric reasons. Consider a Ising model with three antiferromagnetically coupled spins placed at the corners of a triangular plaquette, as shown in Fig. 1.1. The Hamiltonian of the system is $H = J\sum_{i>j}\sigma_i^z\sigma_j^z$, where J is the interaction energy, is a Pauli operator, and the summation runs over all the bonds between spins. This system represent a classic example of a geometrically frustration – because of the triangular geometry, there is no possible spin configuration where the antiferromagnetic coupling is satisfied for all pairs of neighboring spins. In contrast, a system of four spins placed at the corners of a square plaquette does not show geometric frustration.

An important consequence of geometric frustration is that the system does not have a unique ground state. Denoting the two possible spin states as $\uparrow$ and $\downarrow$, we have six degenerate spin configurations: $|\downarrow\uparrow\uparrow\rangle, |\uparrow\downarrow\uparrow\rangle, |\uparrow\uparrow\downarrow\rangle, |\uparrow\downarrow\downarrow, \downarrow\uparrow\downarrow\rangle$ and $|\downarrow\downarrow\uparrow\rangle$, all having the same energy $-J$.

Geometric frustration also occurs at the macroscopic scale, i.e. in extended lattices. Lattices in which frustrated spin models can be defined are referred to as *geometrically frustrated lattices*. For example, a triangular lattice is geometrically frustrated for the Ising model, and a kagome lattice is geometrically frustrated for both the Ising model and the Heisenberg model (Fig. 1.2). In such macroscopic frustrated magnetic systems, the large degeneracy of ground states can lead to a spin liquid, where spins are highly correlated and entangled but long-range order is inhibited even at zero temperature because of quantum fluctuations [1,

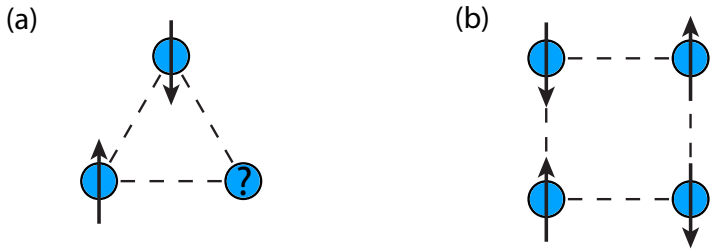

Figure 1.1: Antiferromagnetically coupled Ising spins in a (a) triangular plaquette and (b) a square plaquette. In (a), the system is frustrated and does not have a unique ground state. In (b) the system is not frustrated.

2, 3].

Frustrated magnetism is extensively studied both numerically [4, 5] and experimentally [6, 7]. Yet, the topic is very challenging and there are still a lot of open questions in this field of research [8]. For example, the exact details of the ground state of a Heisenberg kagome antiferromagnet is still unresolved [7]. One reason is that a spin liquid is susceptible to any kind of "perturbations" and sample imperfections, as there is no other energy scale present in the degenerate ground-state manifold. Finding a faithful realization of the ideal kagome antiferromagnet is therefore difficult. Also, a spin liquid is a highly correlated state, which makes it difficult to simulate on a classical computer.

Flat band

A flat band is an energy band with no dispersion. The origin of a flat band is quantum destructive interference. A lattice model leads to a flat band if and only if a set of eigenstates known as compact localized states (CLS) can be constructed [9]. These CLS are localized in real space, as tunneling paths leading to the outside of the localized region cancel one another out by interference.

Take the kagome lattice as an example. The kagome lattice possesses a flat band in the tight-binding model (see chapter 2). We can define the creation operator $\hat{A}$ for a CLS as

$$\hat{A} = \frac{1}{\sqrt{6}} \sum_{i \in \hexagon} (-1)^i \hat{c}_i \tag{1.1}$$

$\hat{c}_i$ is a creation operator for site i, and i runs over the six sites around a hexagonal plaquette. Each CLS occupies one hexagonal plaquette, and has alternating phases around the plaquette's vertices (Fig. 1.3). Tunneling to a nearby site outside the plaquette takes place through two out-of-phase paths, resulting in destructive interference. As a result, the CLS states are localized in real space. The CLS states are actual eigenstates for a flat band. This is in contrast to Wannier states, which can be defined for a flat band (or a set of bands involving a flat band) and are also localized in real space but are not eigenstates.

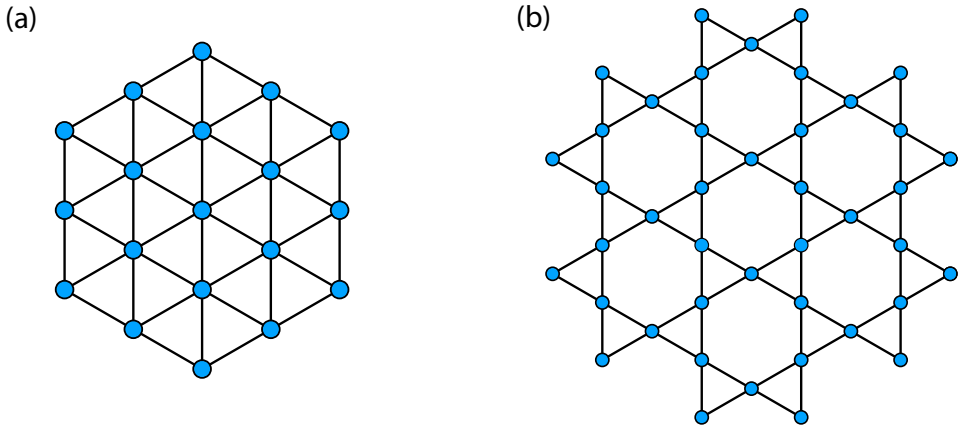

Figure 1.2: Two examples of geometrically frustrated lattices: (a) the triangular lattice, and (b) the kagome lattice.

While being geometrically frustrated does not always imply the possession of flat bands, and vice versa, for the kagome lattice, the two are actually related. For example, a frustrated Heisenberg model can be derived from a tight-binding model with frustrated tunneling in the strongly interacting regime [10]. In both cases, a degenerate manifold is present, either due to a set of degenerate Bloch states/CLS, or a set of degenerate spin configurations.

Because of the absence of kinetic energy (dispersion), the physics of a system of particles in a flat band is dictated solely by their interactions (and/or disorder). This makes flat band systems an ideal setting for studying interaction-driven physics. For bosons, a number of exotic phases of matter have been proposed to be hosted in a flat band, for instance Wigner crystals, supersolids and trion superfluids [11, 12]. For fermions, flat bands are considered as a setting to realize ferromagnetism [13, 14] and superconductivity with enhanced critical temperature by taking advantage of the high density of states for coupling between fermions [15]. Very recently, superconductivity is observed in twisted bilayer graphene systems and it is attributed to an emergent flat band that shows up when the twisted angle is right at the magic angle [16, 17, 18].

Another exciting possibility is the realization of strongly interacting topological states. A topological (nearly-) flat band resembles a Landau level. When partially filled, such a band is predicted to host fractional quantum hall states at room temperature [19, 20, 21].

For a more comprehensive review of the subject, see [22, 23].

1.2 Quantum simulation

We have seen that the kagome lattice offers exciting opportunities for studying exotic physics and realizing novel phases of matter. To test out various theoretical models, we perform

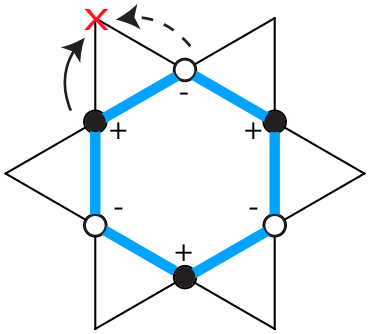

Figure 1.3: Wavefunction of a compact localized state. Because of its alternating phases around the hexagonal plaquette, tunneling to a neighboring site has zero probability due to destructive interference.

quantum simulations. There are two types of quantum simulation, namely digital and analog quantum simulation [24]. We will focus on analog quantum simulation, where a controllable and (relatively) simple quantum system that is accurately described by the theoretical model we want to learn about is created and studied.

Analog quantum simulation has been performed on various experimental platforms (quantum simulators), including ultracold atoms in optical lattices [25, 26, 27], trapped ions [28], superconducting circuits [29], photonic circuits [30] etc. The work reported in this thesis is performed with ultracold atoms in optical lattices.

Ultracold atoms in optical lattices

Employing various laser cooling and trapping techniques developed over decades in the field of atomic physics, neutral atoms can be cooled down to extremely low (ultracold) temperatures – only a few billionth of a degree [**chu09**, 31, 32, 33, 34]. At such low temperatures, the quantum nature of the atoms is fully manifested. Bosons occupy the ground state of the system macroscopically, forming a Bose-Einstein condensate [32, 35, 36]. Fermions atoms fill up all the energy states from the ground state up to an energy (Fermi energy), as allowed by Pauli-exclusion principle, forming a Fermi degenerate gas [37].

Ultracold atoms can be loaded into an optical lattice – a periodic intensity pattern formed by interference of laser light. Light field induces a dipole moments in atoms, which in turn interacts with the light field, creating a periodic potential that bears the same geometry as the intensity pattern and traps the atoms. This constructs a conceptually simple system where identical quantum particles reside in a discretized lattice. Naturally, it can be used to perform quantum simulations of theoretical models for solid-state materials. In such models, materials are often abstracted as a system of electrons residing in a discrete lattice originated from a periodic ionic potential.

This ultacold-atom quantum simulator has a number of remarkable features. For example, it is free of detects and impurities, making interpretations of experimental data more straightforward. Also, it is highly controllable and tunable. For example, the depth of the lattice atoms reside in can be adjusted easily by tuning the power of laser beams. The lattice structure itself can be modulated dynamically, say by changing the frequencies of the laser beams. Many of the experiments that have been demonstrated with ultrcold atoms in optical lattices are difficult, if not impossible, to be performed with solid-state materials.

Optical lattices with different geometries and dimensionality can be created by arranging laser beams in different ways. In addition to the one-dimensional lattice [38] and the three-dimensional cubic lattice [39], a number of two-dimensional geometries have been realized in the field, including square lattice, the triangular lattice [40], the honeycomb lattice [41], the double-well lattice [42], the Lieb lattice [43] and the kagome lattice [44] (by our group).

For a detailed review of the field of quantum simulation using ultracold atoms in optical lattices, see Ref. [25, 26, 27].

1.3 Outline

The main theme of the research work reported in this dissertation is the quantum simulation of quantum models for bosonic particles in geometrically frustrated kagome lattices. Below are summaries of the content in each chapter:

Chapter 2 We explain the basic theory that underlies the work reported in the rest of the dissertation. We also explain the experimental scheme for the construction of optical kagome lattices, both regular and trimerized.

Chapter 3 We describe the experimental apparatus for performing quantum simulation, with a focus on the setup that creates optical lattices. We describe in details two major upgrades of the apparatus – a new optical system that creates a triangular lattice at 532-nm, and an upgrade phase feedback system that allows arbitrary and dynamic control of the optical superlattice geometry.

Chapter 4 This short chapter concerns an experiment simulating the Bose Hubbard model in an optical trimerized kagome lattice in the strongly interacting regime. This work represents the first realization of an optical lattice with such geometry. We discuss some important aspects of data analysis in this work.

Chapter 5 This chapter concerns an experiment studying the effects of mean-field interactions in the tight-binding model. In this work measure the band dispersion of the kagome flat band and show its distortion due to interactions. We discuss details on experimental protocol, data analysis and numerical simulations.

Chapter 6 We develop an idea on exploring the quadratic band touching point in the kagome band structure. Preliminary experimental results and some calculations based on interacting mean-field model that might guide future research directions are discussed.

Both works in chapter 4 and 5 are already reported in academic journals [45, 46]. Instead of restating the results that can be found in the published materials, we focus on explaining in details some aspects of the experimental procedure and data analysis that are not reported elsewhere.

Chapter 2

Kagome lattice and Its Optical Representation

This chapter serves to lay the foundation for discussions in the rest of this dissertation. We first introduce the kagome lattice and describe its features. We then study and solve the tight-binding model of this lattice, and point out several important aspects of the band structure. Finally, we explain our experimental scheme for realizing an optical kagome lattice. We calculate the band structure of the optical kagome lattice at realistic experimental parameters and compare it to the tight-binding one.

2.1 Basics

The kagome lattice, shown in Fig. 1.2, can be viewed as a lattice of corner-sharing triangles, or a lattice of hexagrams. It has a triangular Bravais lattice with three sites per unit cell. This lattice has a number of different symmetries. They include (a) three-fold rotational (C_3) symmetry about the hexagram centers, (b) inversion (I) symmetry with inversion centers located at both the hexagram centers and all the lattice sites, as well as (c) mirror (M) symmetries for six different symmetry lines that bisect the hexagons through either their vertices or edges.

We define the primitive lattice vectors and the corresponding reciprocal vectors of the kagome lattice as below,

$$\mathbf{a}_1 = a \begin{pmatrix} 0 \\ 1 \end{pmatrix}, \qquad \mathbf{a}_2 = a \begin{pmatrix} -\sqrt{3}/2 \\ 1/2 \end{pmatrix} \tag{2.1}$$

$$\mathbf{G}_1 = G \begin{pmatrix} 1/2 \\ \sqrt{3}/2 \end{pmatrix}, \qquad \mathbf{G}_2 = G \begin{pmatrix} -1 \\ 0 \end{pmatrix} \tag{2.2}$$

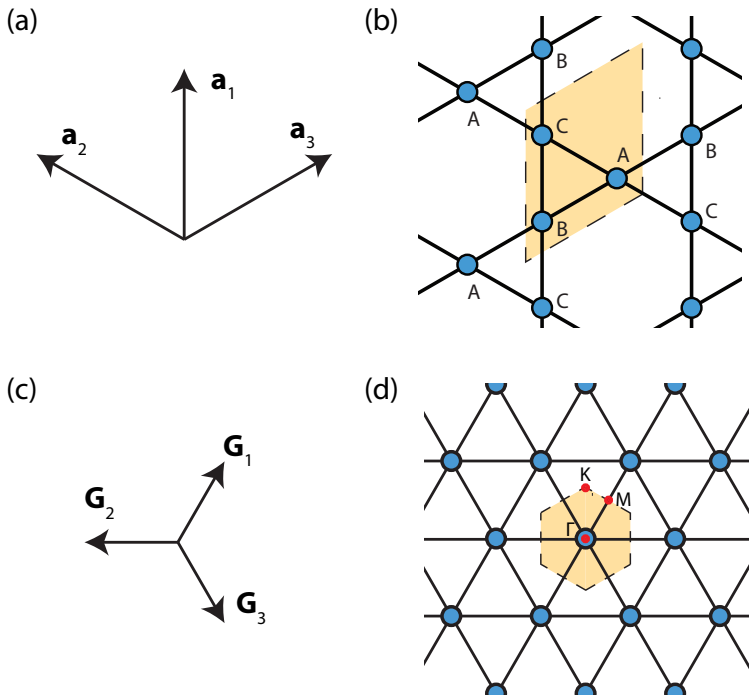

Figure 2.1: (a) Definitions of the primitive unit vectors. (b) A close up of the kagome lattice with labelled sites. A unit cell formed by $\mathbf{a}_1$ and $\mathbf{a}_2$ is indicated by a shaded yellow region. (c) Definitions of the reciprocal lattice vectors. (d) Reciprocal lattice. The first Brilluoin zone is indicated by a shaded yellow region. Symmetry points Γ, K and M are labelled.

where a is the lattice spacing, and $G = 4\pi/(\sqrt{3}a)$. From the definitions above, we have the relations $\mathbf{a}_i \cdot \mathbf{G}_j = 2\pi\delta_{i,j}$. For convenience in later discussions, we also define $\mathbf{a}_3 = \mathbf{a}_1 - \mathbf{a}_2$ and $\mathbf{G}_3 = -\mathbf{G}_1 - \mathbf{G}_2$. We also write down the positions of the lattice sites in a unit cell as,

$$\mathbf{R}_A = (1/2)\mathbf{a}_3, \qquad \mathbf{R}_B = \mathbf{0}, \qquad \mathbf{R}_C = (1/2)\mathbf{a}_1 \tag{2.3}$$

The position of any site can be written using the unit cell index $s = (s_1, s_2)$ and site index i as $\mathbf{R}_{s,i} = \mathbf{R}_s + \mathbf{R}_i = (s_1\mathbf{a}_1 + s_2\mathbf{a}_2) + \mathbf{R}_i$, for $i \in \{A, B, C\}$.

In the reciprocal lattice shown in Fig. 5.1 (b), a few important symmetric points are marked. They are

$$\Gamma : \begin{pmatrix} 0 \\ 0 \end{pmatrix}, \qquad K : \begin{pmatrix} 1 \\ 0 \end{pmatrix} q_K \qquad M : \begin{pmatrix} \sqrt{3}/4 \\ 3/4 \end{pmatrix} q_K \tag{2.4}$$

where q_K is defined as the distance from Γ to K in the reciprocal space. Note that there are similar locations in the first Brilluoin zone where K and M can be defined. They are either

related to the one chosen above by a reciprocal lattice vector and are thus equivalent, or by time reversal symmetry, which is not always guaranteed.

2.2 Tight-binding model

In this section, we introduce the tight-binding model defined on the kagome lattice. Going to the momentum space, the Hamiltonian of the system is reduced to a 3×3, quasimomentum-dependent matrix. Solving this matrix at all quasimomenta, the kagome band structure can be obtained.

In the tight-binding model, we work in the basis of Wannier states $W(\mathbf{r}-\mathbf{R}_{s,i})$, which has spatially localized wavefunction centered at the lattice site with position $\mathbf{R}_{s,i}$. For clarity, we define $a_s^\dagger$ ($b_s^\dagger$, $c_s^\dagger$) as the creation operator that creates a particle in the Wannier basis in the lattice site A (B, C) of unit cell s. In the following, we refer to intra- and inter-trimer tunneling energy as J and J' respectively, such that the derivation applies to a more generic setting. For the normal (trimerized) kagome lattice $J = J'(J \neq J')$. The tight-binding Hamiltonian is given by

$$\begin{aligned} H &= -J\sum_s \left(c_s^\dagger a_s + b_s^\dagger c_s + a_s^\dagger b_s + \text{H.C.}\right) \\ &\quad -J'\sum_s \left(c_{(s_1,s_2-1)}^\dagger a_s + b_{(s_1+1,s_2)}^\dagger c_s + a_{(s_1-1,s_2+1)}^\dagger b_s + \text{H.C.}\right) \end{aligned} \tag{2.5}$$

In the equation, the first sum includes coupling within a single unit cell m, and the second sum includes coupling between different neighboring cells. The second sum is written in a way such that only half of the inter-trimer bonds are taken into account. When such a term is enumerated for all unit cells, there is no double counting.

After writing down the Hamiltonian in the Wannier basis, we go into the momentum space by performing Fourier Transform $\hat{a}_m^\dagger = \sqrt{N}^{-1}\sum_{\mathbf{k}} \exp[i\mathbf{k}\cdot(\mathbf{R}_m + \mathbf{R}_a)]\tilde{a}_{\mathbf{k}}^\dagger$ [1] and similarly for $\hat{b}_m^\dagger$ and $\hat{c}_m^\dagger$. Consider the first summation,

[1] Conventionally, the Fourier transform should be written as $\hat{a}_m^\dagger = \sqrt{N}^{-1}\sum_{\mathbf{k}} \exp[i\mathbf{k}\cdot\mathbf{R}_m]\tilde{a}_{\mathbf{k}}^\dagger$ where the phase factor $i\mathbf{k}\cdot\mathbf{R}_a$ is not included. However, we can perform a gauge transformation $\tilde{a}_{\mathbf{k}}^\dagger \to \exp[i\mathbf{k}\cdot\mathbf{R}_A]\tilde{a}_{\mathbf{k}}^\dagger$ and obtain the expression written in the text.

$$
\begin{aligned}
& -J\sum_{s}\left(c_m^\dagger a_m + b_m^\dagger c_m + a_m^\dagger b_m + \text{H.C.}\right) \\
= \; & -J\sum_{s}\left(N^{-1}\sum_{\mathbf{k},\mathbf{k}'}\exp[i\mathbf{k}\cdot(\mathbf{R}_s+\mathbf{R}_\text{C})]\exp[-i\mathbf{k}'\cdot(\mathbf{R}_s+\mathbf{R}_\text{A})]\tilde{c}_\mathbf{k}^\dagger\tilde{a}_{\mathbf{k}'} + ... + \text{H.C.}\right) \\
= \; & -J\sum_{\mathbf{k},\mathbf{k}'}\Bigg(\underbrace{\left(N^{-1}\sum_{s}\exp[i(\mathbf{k}-\mathbf{k}')\cdot\mathbf{R}_s]\right)}_{\delta_{\mathbf{k},\mathbf{k}'}}\exp[i(\mathbf{k}\cdot\mathbf{R}_\text{C}-\mathbf{k}'\cdot\mathbf{R}_\text{A})]\tilde{c}_\mathbf{k}^\dagger\tilde{a}_{\mathbf{k}'} + ... + \text{H.C.}\Bigg) \\
= \; & -J\sum_{\mathbf{k}}\left(\exp[i\mathbf{k}\cdot\mathbf{R}_\text{CA}]\tilde{c}_\mathbf{k}^\dagger\tilde{a}_\mathbf{k} + \exp[i\mathbf{k}\cdot\mathbf{R}_\text{BC}]\tilde{b}_\mathbf{k}^\dagger\tilde{c}_\mathbf{k} + \exp[i\mathbf{k}\cdot\mathbf{R}_\text{AB}]\tilde{a}_\mathbf{k}^\dagger\tilde{b}_\mathbf{k} + \text{H.C.}\right) \qquad (2.6)
\end{aligned}
$$

Here, $\mathbf{R}_\text{CA} = \mathbf{R}_\text{C} - \mathbf{R}_\text{A}$ and so on. Similarly, for the inter-trimer terms,

$$
\begin{aligned}
& -J'\sum_{m}\left(c_{(s_1,s_2-1)}^\dagger a_m + b_{(s_1+1,s_2)}^\dagger c_m + a_{(s_1-1,s_2+1)}^\dagger b_m + \text{H.C.}\right) \\
= \; & -J'\sum_{\mathbf{k}}\Big(\exp[i\mathbf{k}\cdot(\mathbf{R}_\text{CA}-\mathbf{a}_2)]\tilde{c}_\mathbf{k}^\dagger\tilde{a}_\mathbf{k} + \exp[i\mathbf{k}\cdot(\mathbf{R}_\text{BC}+\mathbf{a}_1)]\tilde{b}_\mathbf{k}^\dagger\tilde{c}_\mathbf{k} + \exp[i\mathbf{k}\cdot(\mathbf{R}_\text{AB}-\mathbf{a}_3)]\tilde{a}_\mathbf{k}^\dagger\tilde{b}_\mathbf{k} \\
& \qquad +\text{H.C.}\Big) \\
= \; & -J'\sum_{\mathbf{k}}\left(\exp[-i\mathbf{k}\cdot\mathbf{R}_\text{CA}]\tilde{c}_\mathbf{k}^\dagger\tilde{a}_\mathbf{k} + \exp[-i\mathbf{k}\cdot\mathbf{R}_\text{BC}]\tilde{b}_\mathbf{k}^\dagger\tilde{c}_\mathbf{k} + \exp[-i\mathbf{k}\cdot\mathbf{R}_\text{AB}]\tilde{a}_\mathbf{k}^\dagger\tilde{b}_\mathbf{k} + \text{H.C.}\right)
\end{aligned} \qquad (2.7)
$$

Combining the results,

$$
\begin{aligned}
H &= -\sum_{\mathbf{k}} J\left((\exp[i\mathbf{k}\cdot\mathbf{R}_\text{CA}] + r\exp[-i\mathbf{k}\cdot\mathbf{R}_\text{CA}])\tilde{c}_\mathbf{k}^\dagger\tilde{a}_\mathbf{k} + ... + \text{H.C.}\right) \\
&= \sum_{\mathbf{k}}\psi_\mathbf{k}^\dagger H_\mathbf{k}\psi_\mathbf{k} \qquad (2.8)
\end{aligned}
$$

$$
(2.9)
$$

where,

$$
\begin{aligned}
H_{\mathbf{k}} &= -J \begin{pmatrix} 0 & e^{+i\mathbf{k}\cdot\mathbf{R}_{\mathrm{AB}}} + re^{-i\mathbf{k}\cdot\mathbf{R}_{\mathrm{AB}}} & e^{i\mathbf{k}\cdot\mathbf{R}_{\mathrm{AC}}} + re^{-i\mathbf{k}\cdot\mathbf{R}_{\mathrm{AC}}} \\ e^{-i\mathbf{k}\cdot\mathbf{R}_{\mathrm{AB}}} + re^{+i\mathbf{k}\cdot\mathbf{R}_{\mathrm{AB}}} & 0 & e^{+i\mathbf{k}\cdot\mathbf{R}_{\mathrm{BC}}} + re^{-i\mathbf{k}\cdot\mathbf{R}_{\mathrm{BC}}} \\ e^{-i\mathbf{k}\cdot\mathbf{R}_{\mathrm{AC}}} + re^{+i\mathbf{k}\cdot\mathbf{R}_{\mathrm{AC}}} & e^{-i\mathbf{k}\cdot\mathbf{R}_{\mathrm{BC}}} + re^{+i\mathbf{k}\cdot\mathbf{R}_{\mathrm{BC}}} & 0 \end{pmatrix} \\
\psi^{\dagger}_{\mathbf{k}} &= (a^{\dagger}_{\mathbf{k}}\, b^{\dagger}_{\mathbf{k}}\, c^{\dagger}_{\mathbf{k}}) \\
r &= J'/J
\end{aligned}
\tag{2.10}
$$

In particular, if we take $r = 1$ (regular kagome lattice), the Hamiltonian takes the following simple form,

$$
H_{\mathbf{k}} = -2J \begin{pmatrix} 0 & \cos(k3) & \cos(k2) \\ \cos(k3) & 0 & \cos(k1) \\ \cos(k2) & \cos(k1) & 0 \end{pmatrix}, \tag{2.11}
$$

where $k1 = \mathbf{k}\cdot\mathbf{a}_1/2$, $k2 = \mathbf{k}\cdot\mathbf{a}_2/2$ and $k3 = \mathbf{k}\cdot(\mathbf{a}_2 - \mathbf{a}_1)$. Now we can solve for the band structure, which is boiled down to solving Eq. 2.11 for different values of $\mathbf{k}$. The characteristic equation $\det|H_k + \epsilon I| = 0$ is exactly solvable. The solutions are

$$
\epsilon = (1+r)J \quad \text{or} \quad \epsilon = \frac{J}{2}\left[-(1+r) \pm \sqrt{(3r-1)^2 + 8(1+r\Omega(\mathbf{k}))}\right] \tag{2.12}
$$

where $\Omega(\mathbf{k}) = \cos(2\cdot k1) + \cos(2\cdot k2) + \cos(2\cdot k3)$. We plot the band structure for the regular ($r = 1$) kagome lattice in Fig. 2.2. A few observations are made regarding the special features of the kagome band structure.

Flat band The first solution in Eq. 2.12, which has the highest eigenenergy, has no dependence on $\mathbf{k}$. This corresponds to a band that is dispersionless, or *flat band*. The origin and importance of flat bands is explained in chapter 1. In chapter 5, we will discuss an experiment that demonstrates the distortion of this flat band due to interaction effects.

Quadratic band touching point At the Γ point where $\Omega = 3$, the eigenenergies are $\epsilon = (1+r)J$ (double root) and and $-2(1+r)J$. The two-fold degeneracy of the higher-energy solutions indicate that there is band touching between the second ($n = 2$) and third ($n = 3$, flat) band. Near the touching point, the energy difference between the touching bands changes quadratically.

The existence of this touching point can be explained by the C_3 symmetry of the lattice, and also by the incompleteness of the CLS basis. In chapter 6, we will investigate further into the origin and features of this touching point.

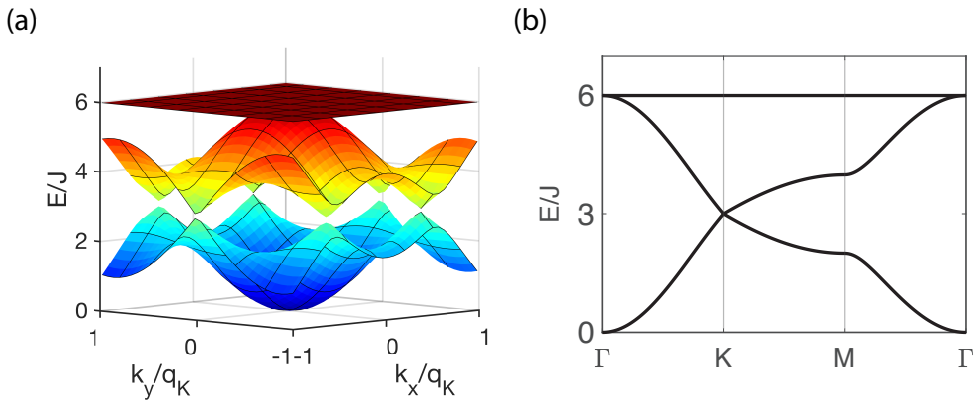

Figure 2.2: (a) Full kagome tight-binding band structure. (b) One-dimensional cut-through of the band structure along the symmetry line $\Gamma - K - M - \Gamma$ (see Eq. 2.4).

Dirac points There are other band touching points between the first and the second band. They occur when the term in the square root in the second solution in Eq. 2.12 vanishes, which is possible only when $\Omega = -3/2$, which corresponds to the two equivalent K points in the Brilluoin zone, and $r = 1$, i.e. a regular kagome lattice. Once the kagome lattice is trimerized , the lowest two bands are gapped out by $6|r - 1|J$. These touching points are actually the famous Dirac point, which is widely studied in the context of the honeycomb lattice.

2.3 Construction of optical kagome lattice

To perform quantum simulations of many-body quantum-mechanical models for the kagome lattice, we load ultracold atoms into an optical lattice with the kagome geometry. In this section, we explain the scheme for creating such an optical lattice using interfering laser beams.

Observe that a kagome lattice is simply a triangular lattice with one out of every four sites removed. To create an optical kagome lattice, we can superimpose two optical triangular lattices, one at wavelength λ and is *attractive*, and the other at 2λ and is *repulsive*. These two lattices are referred to as the short-wavelength (SW) and the long-wavelength (LW) lattices respectively in the rest of the dissertation. The two lattices are superimposed at an particular relative position that one out of every four attractive SW lattice sites sit on top of a repulsive LW lattice site, and therefore is energetically raised. The remaining attractive sites of the resultant superlattice thus forms a kagome lattice (Fig. 2.3).

For the trimerized kagome lattice, this scheme has to be slightly modified. We create an *attractive* LW triangular lattice instead and place its lattice sites in the middle of the trimers formed by three SW lattice sites. For details, see Ref. [47].

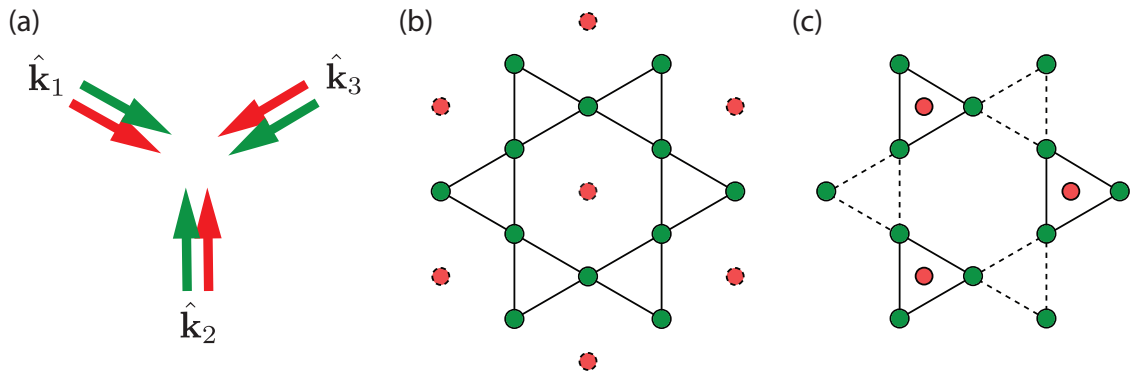

Figure 2.3: (a) Configuration of laser beams. Beams of both 532 nm and 1064 nm co-propagate and are focused onto atoms along three different directions that intersect at 120 degrees. (b) To create a kagome lattice, an attractive SW triangular lattice (formed by in-plane polarized light) and a repulsive LW triangular lattice (formed also by in-plane polarized light) are superimposed. The repulsive sites of the LW lattice (red dots with dashed circumference) are situated on top of a SW lattice site (green dots). (c) To create a trimerized kagome lattice, an attractive LW triangular lattice (formed by out-of-plane polarized light) is used instead. The attractive sites of the LW lattice (red dots with solid circumference) are situated in the middle of three SW lattice sites. In the figure, one of the two equivalent trimerized pattern is shown.

Below we derive the expressions of the potential of a triangular lattice, a regular kagome lattice and a trimerized kagome lattice. From there focus on the regular optical kagome lattice and calculate its band structure through direct diagonalization of the single-particle Hamiltonian. We confirm that all the important features emphasized in the last section are reproduced.

Triangular lattice

Let us first consider the construction of an optical triangular lattice [40]. We write down a set of wavevectors $\{\mathbf{k}_i\}$ for the three intersecting beams as follows

$$\mathbf{k}_1 = k \begin{pmatrix} \sqrt{3}/2 \\ -1/2 \end{pmatrix}, \qquad \mathbf{k}_2 = k \begin{pmatrix} 0 \\ 1 \end{pmatrix}, \qquad \mathbf{k}_3 = k \begin{pmatrix} -\sqrt{3}/2 \\ -1/2 \end{pmatrix} \tag{2.13}$$

Here $k = 2\pi/\lambda$ is the magnitude of the wavevector and λ is the wavelength of light. We keep k generic so that the following derivation applies to both the SW and LW lattices. We also denote the polarizations of the laser beams by $\{\boldsymbol{\epsilon}_i\}$.

Assuming equal electric field strength E from each beam and define $I_0 = |E|^2$, the total electric field is

$$\mathbf{E}(\mathbf{r}, t) = \sum_i \mathbf{E}_i = \sum_i E\boldsymbol{\epsilon}_i e^{i(\mathbf{k}_i \cdot \mathbf{r} - \omega t)} \tag{2.14}$$

where ω is the angular frequency of the light. Here $\mathbf{E}(\mathbf{r}, t)$ is a phasor. We calculate the time-averaged intensity and the potential seen by the atoms:

$$\begin{aligned} V(\mathbf{r}, t) &\propto I(\mathbf{r}, t) \\ &= \frac{1}{T}\int_0^T (\mathrm{Re}(\mathbf{E}(\mathbf{r}, t))^2 dt \\ V(\mathbf{r}, t) &= 4V_0\left(\frac{3}{4} + \frac{1}{2}\sum_{i=1}^{3}\cos(\phi_i)\cos(\mathbf{G}_i \cdot \mathbf{r})\right) \end{aligned} \tag{2.15}$$

where $\cos(\phi_i) = \boldsymbol{\epsilon}_j \cdot \boldsymbol{\epsilon}_k$ and $\mathbf{G}_i = \mathbf{k}_j - \mathbf{k}_k$, for cyclic permutation of i, j and $k \in \{1, 2, 3\}$. Since $3 \geq \sum_i \cos(\mathbf{G}_i \cdot \mathbf{r}) \geq -\frac{3}{2}$, we can infer the maximum and minimum of the potential with some particular polarizations. In our experiments, lattice beams are either in-plane or out-of-plane polarized. In such cases,

$$\frac{9}{2}V_0 \geq 4V_0\left(\frac{3}{4} - \frac{1}{4}\sum_{i=1}^{3}\cos(\mathbf{G}_i \cdot \mathbf{r})\right) \geq 0 \qquad \text{in-plane polarization} \tag{2.16}$$

$$9V_0 \geq 4V_0\left(\frac{3}{4} + \frac{1}{2}\sum_{i=1}^{3}\cos(\mathbf{G}_i \cdot \mathbf{r})\right) \geq 0 \qquad \text{out-of-plane polarization} \tag{2.17}$$

At the same single beam intensity I_0, the lattice formed by out-of-plane polarized beams is two times deeper. This is because the all the beams have aligned polarization in that case, leading to stronger interference. Also, note that complete destructive interference is possible in both configuration.

The intensity patterns formed by in-plane and out-of-plane beams are complementary to each other. While in-plane polarized beams form a triangular (honeycomb) lattice of intensity minima (maxima), out-of-plane polarized beams form a triangular (honeycomb) lattice of intensity maxima (minima). Whether atoms are attracted to the intensity maxima or minima depend on the sign of the ac stark shift. For example, the 532-nm SW light is blue-detuned with respect to the main atomic transition line of rubidium-87 atoms at 780 nm. In that case, $V_0 \propto |I_0|$, and atoms are attracted to intensity minima to lower potential energy. In contrast, 1064-nm LW light is red-detuned and $V_0 \propto -|I_0|$. Therefore atoms are attracted to the intensity maxima.

Kagome lattice

To create the regular optical kagome lattice, we choose the polarization of all the beams to be in-plane, i.e. $\cos(\theta_{i,j}) = -1/2$ for all pairs of i and j. As a result, the SW lattice is an attractive triangular lattice, and the LW lattice is a repulsive triangular lattice. We define the lattice depth $V_{\mathrm{SW/LW}} = 9/2|I_0|$ for both lattices. The expressions for the the two lattice potentials are

$$V_{\mathrm{SW}}(\mathbf{r},t) = \frac{8}{9}V_{\mathrm{SW}}\left(\frac{3}{4} - \frac{1}{4}\sum_{i=1}^{3}\cos\left(2\mathbf{G}_i\cdot\mathbf{r} + \theta_i^{\mathrm{SW}}\right)\right) \tag{2.18}$$

$$V_{\mathrm{LW}}(\mathbf{r},t) = -\frac{8}{9}V_{\mathrm{LW}}\left(\frac{3}{4} - \frac{1}{4}\sum_{i=1}^{3}\cos\left(\mathbf{G}_i\cdot\mathbf{r} + \theta_i^{\mathrm{LW}}\right)\right) \tag{2.19}$$

where we have added the phase factors $\theta_i^{\mathrm{SW/LW}}$ to the expressions. These phase factors are important as they determine the relative position of the two triangular lattices. They have to be actively stabilized to construct a lattice with well defined geometry. An electronic feedback system was built by former member Thomas Barter for this purpose [47]. In Chapter 3, we describe an upgraded phase lock system which allows us to arbitrarily adjust these phases and therefore dynamically translate or distort the lattices. In the following, we assume that all the phases are controllable and static.

The kagome lattice potential $V_{\mathrm{kag}}(\mathbf{r},t)$ is obtained by adding $V_{\mathrm{SW}}(\mathbf{r},t)$ and $V_{\mathrm{LW}}(\mathbf{r},t)$ and setting all the $\theta_i^{\mathrm{SW/LW}}$ to be zero [2]:

$$V_{\mathrm{kag}}(\mathbf{r}) = \frac{2}{3}(V_{\mathrm{SW}} - V_{\mathrm{LW}}) - \frac{2}{9}\left(V_{\mathrm{SW}}\sum_{i,j}\cos(2\mathbf{G}_i\cdot\mathbf{r}) - V_{\mathrm{LW}}\sum_{i,j}\cos(\mathbf{G}_i\cdot\mathbf{r})\right) \tag{2.20}$$

Plots of $V_{\mathrm{kag}}(\mathbf{r},t)$ at different lattice depth ratio $V_{\mathrm{SW}}/V_{\mathrm{LW}}$ are shown in Fig. 2.4.

Trimierzed Kagome lattice

To construct an optical trimerized kagome lattice, we superimpose an in-plane polarized SW lattice to an out-of-plane LW lattice. In this case, both the SW and LW lattices are an attractive triangualr lattice. We define $V_{\mathrm{LW}} = 9|I_0|$. The lattice phases are set so that LW lattice intensity maxima are situated at the center of trimer comprised of either the A-B-C sites or the A-C-D sites. The lattice potentials can be written as

[2] There are other choices of phases that make kagome lattices too, but they are all equivalent up to lattice translation.

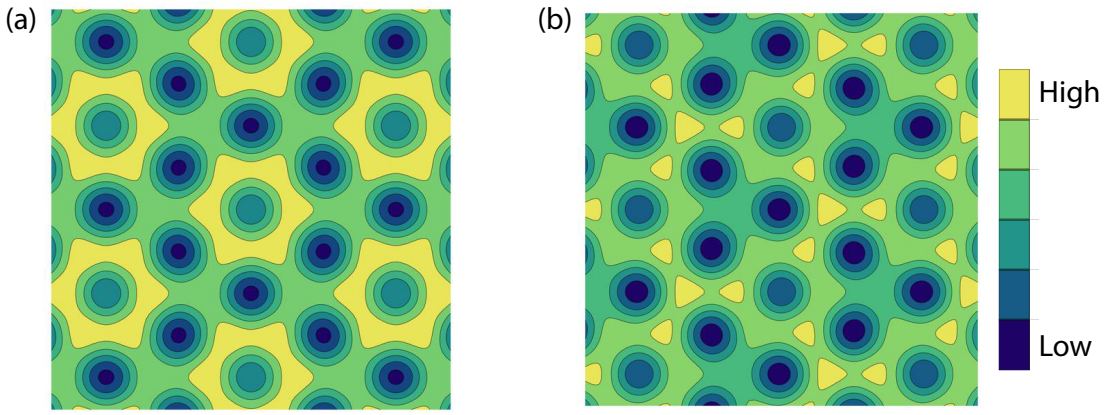

Figure 2.4: Potential of (a) a regular optical kagome lattice and (b) a trimerized optical kagome lattice. A lattice depth ratio is $V_{\mathrm{LW}}/V_{\mathrm{SW}} = 1/3$ is used for calculations.

$$V_{\mathrm{TKL}}(\mathbf{r},t) = \frac{2}{3}(V_{\mathrm{SW}} - \frac{1}{2}V_{\mathrm{LW}}) - \frac{2}{9}\left(V_{\mathrm{SW}}\sum_{i,j}\cos(2\mathbf{G}_i\cdot\mathbf{r}) + V_{\mathrm{LW}}\sum_{i,j}\cos\big(\mathbf{G}_i\cdot\mathbf{r}+\theta_i^{\mathrm{LW}}\big)\right) \tag{2.21}$$

where

$$\theta_1 = \pm\frac{\pi}{3}, \qquad \theta_2 = \pm\frac{2\pi}{3}, \qquad \theta_3 = \pm\frac{\pi}{3} \tag{2.22}$$

The + and − cases correspond to the two different ways of trimerization.[3]

2.4 Band theory

In this section, we solve for the band structure of the regular optical kagome lattice by direct diagonalizing the full single-particle Hamiltonian. We confirm that, in appropriate parameter regimes, it reproduces the important features described earlier this chapter, namely the possession of a flat band and the presence of a quadratic band touching point, of the tight-binding band structure.

The Hamiltonain for a particle loaded into the optical kagome lattice is formally written as

$$H = \frac{\hat{\mathbf{p}}^2}{2m} + V_{\mathrm{kag}}(\mathbf{r}) \tag{2.23}$$

[3]Again, there are other choices of phases that make equivalent trimerized kagome lattices up to lattice translation.

By the Bloch's Theorem, the eigenstate with discrete translational invariance is given by

$$\psi_{\mathbf{k}}^{(n)}(\mathbf{r}) = \exp(i\mathbf{k}\cdot\mathbf{r})u_{\mathbf{k}}^{(n)}(\mathbf{r}) \tag{2.24}$$

Here $\mathbf{k}$ is the quasimomentum and n is the band index. Substituting Eq. 2.24 into Eq. 2.23, we obtain the following equation for $u_{\mathbf{q}}^{(n)}(\mathbf{r})$:

$$\left(\frac{(\hat{\mathbf{p}}+\mathbf{q})^2}{2m} + V_{\text{kag}}(\mathbf{r})\right) u_{\mathbf{k}}^{(n)}(\mathbf{r}) = E_{\mathbf{q}}^{(n)} u_{\mathbf{k}}^{(n)}(\mathbf{r}) \tag{2.25}$$

To solve this equation, note that $u_{\mathbf{k}}^{(n)}(\mathbf{r})$ has the same periodicity as the lattice potential $(\mathbf{r})$. Therefore, it can be written in a Fourier basis with discrete momenta $\mathbf{G}_s = s_1\mathbf{G}_1 + s_2\mathbf{G}_2$ (Eq. 2.2), where $s = (s_1, s_3)$ is a composite index. Explicitly,

$$u_{\mathbf{k}}^{(n)}(\mathbf{r}) = \sum_s c_s \exp(i\mathbf{G}_s\cdot\mathbf{r}) = \begin{bmatrix} \vdots \\ c_s \\ \vdots \end{bmatrix} \tag{2.26}$$

where an ordered basis of $\{\mathbf{G}_s\}$ is chosen when writing the state as a vector. Now we want to compute the matrix element $H_{s,s'}$ and cast the problem into the matrix form.

The kinetic energy term evaluates to

$$\langle \mathbf{G}_s' | \frac{(\hat{\mathbf{p}}+\mathbf{q})^2}{2m} | \mathbf{G}_s \rangle = \frac{(\mathbf{G}_s+\mathbf{q})^2}{2m}\delta_{s,s'} \tag{2.27}$$

For the lattice potential term, observe that $\cos(\mathbf{G}\cdot\mathbf{r}) = (1/2)\times(\exp(i\mathbf{G}\cdot\mathbf{r}) + \exp(-i\mathbf{G}\cdot\mathbf{r}))$, we have

$$\begin{aligned} \langle \mathbf{G}_s' | V_{\text{kag}}(\mathbf{r}) | \mathbf{G}_s \rangle = \frac{2}{3}(V_{\text{SW}} - V_{\text{LW}})\delta_{s,s'} \quad &- \quad \frac{1}{9}V_{\text{SW}} \sum_{i=1}^{3} \delta(\mathbf{G}_s - \mathbf{G}_s' \pm 2\mathbf{G}_i) \\ &+ \quad \frac{1}{9}V_{\text{LW}} \sum_{i=1}^{3} \delta(\mathbf{G}_s - \mathbf{G}_s' \pm \mathbf{G}_i) \end{aligned} \tag{2.28}$$

Combining the results, we have

$$H_{s,s'} = \begin{cases} (\mathbf{G}_s+\mathbf{q})^2/(2m) + (2/3)(V_{\text{SW}} - V_{\text{LW}}) & s = s' \\ -(1/9)V_{\text{SW}} & s - s' = \pm\{(2,0),(0,2),(2,-2)\} \\ +(1/9)V_{\text{LW}} & s - s' = \pm\{(1,0),(0,1),(1,-1)\} \\ 0 & \text{otherwise} \end{cases} \tag{2.29}$$

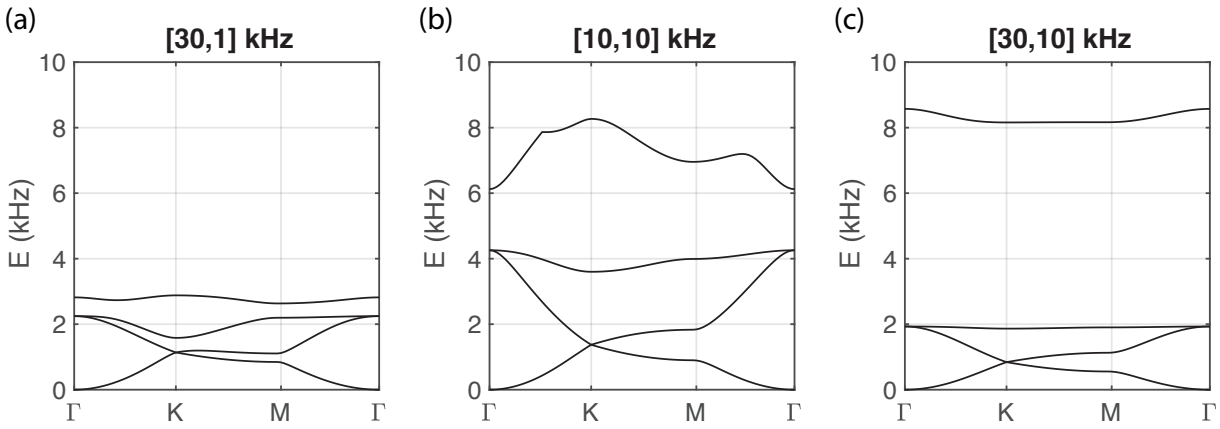

Figure 2.5: Band structures of the regular optical kagome lattice obtained by direct diagonalization for lattice depths $(V_{\mathrm{SW}}, V_{\mathrm{LW}}) = h\times$ (a) (30, 1) , (b) (10, 10) and (c) (30, 10) kHz respectively. In (a), LW lattice is shallow that the D-site remains energetically close to the other three lattice sites, and therefore the lattice geometry is somewhere between triangular and kagome. In (b) the SW lattice too shallow that higher-order tunneling processes are present, breaking the tight-binding assumption. In (c), both lattices are deep enough, the tight-binding band structure is recovered, showing a flat band.

The physical meaning of this matrix is as follows. The diagonal terms represents the kinetic energy of the plane waves, with an energy offset from the lattice potential. The off-diagonal terms represent lattice-mediated coupling between different momentum states. In the reciprocal lattice, particles can hop from one momentum state to another through the momentum transfer in a two photon process, where particles absorb one photon from a lattice beam of one color and emit it into another of the same color. With the SW (LW) lattice, such a process leads to a momentum change of one (two) reciprocal lattice vector(s). In this treatment, off-resonance processes (e.g. absorption and emission of a single photon from each color) and high-order (> 2) photon processes are neglected.

Having cast the problem in the matrix form, the band structure can be numerically calculated by diagonalizing the matrix. The matrix has an infinite dimension in theory and needs to be truncated for practical calculations. For realistic experimental parameters, a truncation to $\max(\mathrm{s}) = 4$ is appropriate.

Band structures

In Fig. 2.5, band structures calculated at three different sets of lattice depths are shown. One can see that in order to recover the tight-binding band structure, both the SW and LW lattices have to be sufficiently deep. When either one lattice is not sufficiently deep, some aspects of the tight-binding model are not satisfied. The SW lattice needs to be deep enough

such that the Wannier function is well defined and localized within single site. That is to ensure higher-order tunneling processes (those beyond nearest neighbors) are suppressed. See [48] for further discussions. The LW lattice needs to be deep enough such that the fourth site in a unit cell is detuned and occupancy in that site is negligible.

2.5 Lattice characterization

The superlattice created in the experiment can be characterized by the momentum distribution of ground-state atoms in a superfluid state in the superlattice. To measure momentum distribution of lattice-trapped atoms, we suddenly turn off the lattice beams and let the atoms either expand in free space for some period of time, or implement the momentum space focusing technique by letting the atoms evolve in a weak underlying magnetic trap for a quarter of a trap period. After that, we take absorption images of the atoms, which reveal their momentum distribution.

To be concrete, we write down the expression of the momentum distribution $n(\mathbf{q})$ in the tight-binding limit:

$$n(\mathbf{q}) = |\tilde{W}(\mathbf{q})|^2 \sum_{s,s',i,j} e^{i\mathbf{q}\cdot(\mathbf{R}_{s,i}-\mathbf{R}_{s',j})} \hat{a}^\dagger_{s',j} \hat{a}_{s,i} \tag{2.30}$$

where s and s' are unit cell indices, $i,j \in \{A,B,C\}$ are lattice site indices, $\tilde{W}(\mathbf{q})$ is the Fourier transform of the Wannier function, and $a^\dagger_{s,i}$ is the creation operation of a particle in the Wannier basis at unit cell s and site i. Here we have made the approximation that Wannier functions are identical at different lattice sites. In the following we make an approximation that the Wannier function takes a Gaussian form: $|\tilde{W}(\mathbf{q})|^2 = \exp(-|\mathbf{q}|^2/a_w^2)$, where a_w is its width in the momentum space, and is identical for all the lattice sites.

We consider a generic state with nonzero quasimomentum $\mathbf{q}_0$:

$$|\psi\rangle = \sum_{l,\alpha} e^{i\mathbf{q}_0\cdot\mathbf{R}_{l,\alpha}} c_\alpha |\alpha\rangle \tag{2.31}$$

To avoid confusion, we define new indices l and α for labelling unit cells and lattice sites. $c_{l,\alpha}$ is the coefficient for the Wannier state $|\alpha\rangle$ at the corresponding site α in unit cell l. We take c_α as complex numbers, and $\sum_\alpha |c_\alpha|^2 = \sum_\alpha P_\alpha = 1$. In fact, for the purpose of lattice characterization, we only need to consider the $\mathbf{q}_0 = 0$ case. In the following, however, we will keep the generic form in Eq. 2.31 so that the derived results can be used in later sections.

With Eq. 2.31, and the assumption that the system is in a superfluid state with long-range order, the momentum space distribution then evaluates to

$$
\begin{aligned}
n(\mathbf{q}) &= |\tilde{W}(\mathbf{q})|^2 \sum_{s,s',i,j} \sum_{l,l',\alpha,\beta} e^{i\mathbf{q}\cdot(\mathbf{R}_{s,i}-\mathbf{R}_{s',j})} c^*_\beta c_\alpha e^{i\mathbf{q}_0\cdot(\mathbf{R}_{l,\alpha}-\mathbf{R}_{l',\beta})} \hat{a}^\dagger_{s',j} \underbrace{\langle\beta|\, \hat{a}^\dagger_{s',j}\hat{a}_{s,i}\, |\alpha\rangle}_{\delta_{i,\beta}\delta_{j,\alpha}\delta_{s,l}\delta_{s',l'}} \\
&= |\tilde{W}(\mathbf{q})|^2 \sum_{s,s',i,j} e^{i(\mathbf{q}-\mathbf{q}_0)\cdot(\mathbf{R}_s-\mathbf{R}_{s'})} e^{i(\mathbf{q}-\mathbf{q}_0)\cdot(\mathbf{R}_i-\mathbf{R}_j)} c^*_i c_\mathrm{j} \\
&= M|\tilde{W}(\mathbf{q})|^2 \underbrace{\sum_s e^{i(\mathbf{q}-\mathbf{q}_0)\cdot\mathbf{R}_s}}_{\delta(\mathbf{q}-\mathbf{q}_0-\mathbf{G})} \sum_{i,j} e^{i(\mathbf{q}-\mathbf{q})\cdot(\mathbf{R}_i-\mathbf{R}_j)} c^*_i c_j \\
&= M|\tilde{W}(\mathbf{q})|^2 \delta(\mathbf{q}-\mathbf{q}_0-\mathbf{G}) \left(1 + \sum_{i>j} 2\cos((\mathbf{q}-\mathbf{q}_0)\cdot(\mathbf{R}_i-\mathbf{R}_j))\,\mathrm{Re}(c^*_i c_j)\right)
\end{aligned}
\tag{2.32}
$$

In the second last line the translational symmetry of the lattice is invoked and M is the number of unit cells. The 1 in the last bracket comes from the sum of all the $|c^*_i c_i|$ terms. The following relations are useful when evaluating the interference term at different $\mathbf{G}$'s:

$$
\begin{aligned}
\mathbf{R}_C - \mathbf{R}_B = \mathbf{R}_D - \mathbf{R}_A &= (1/2)\mathbf{a}_1 \\
\mathbf{R}_D - \mathbf{R}_B = \mathbf{R}_C - \mathbf{R}_A &= (1/2)(\mathbf{a}_1 - \mathbf{a}_2) \\
\mathbf{R}_B - \mathbf{R}_A = \mathbf{R}_C - \mathbf{R}_D &= (1/2)\mathbf{a}_2
\end{aligned}
\tag{2.33}
$$

Below we consider different cases of $\mathbf{q}-\mathbf{q}_0 \in \{\mathbf{G}\}$.

$\mathbf{q}-\mathbf{q}_0 = \mathbf{0}$: Interference is always constructive.

$$
M^{-1}\frac{n(\mathbf{q}_0)}{|\tilde{W}(\mathbf{q}_0)|^2} = 1 + 2\sum_{i>j}\sqrt{P_i P_j}\cos(\theta_{ij}) \tag{2.34}
$$

$\mathbf{q}-\mathbf{q}_0 = \mathbf{G}$: Since $\mathbf{G}_i \cdot (1/2)\mathbf{a}_j = \pi\delta_{i,j}$, the interference can be constructive or destructive, depending on the particular choice of $\mathbf{G}$.

$$
\begin{aligned}
M^{-2}\frac{n(\mathbf{q}_0 \pm \mathbf{G}_1)}{|\tilde{W}(\mathbf{q}_0 \pm \mathbf{G}_1)|^2} = 1 + 2\Big[&+ \cos(\theta_{AB})\sqrt{P_A P_B} + \cos(\theta_{DC})\sqrt{P_D P_C} \\
&- \cos(\theta_{BC})\sqrt{P_B P_C} - \cos(\theta_{DA})\sqrt{P_D P_A} \\
&- \cos(\theta_{DB})\sqrt{P_D P_B} - \cos(\theta_{AC})\sqrt{P_A P_C}\Big]
\end{aligned}
\tag{2.35}
$$

$$M^{-2}\frac{n(\mathbf{q}_0 \pm \mathbf{G}_2)}{|\tilde{W}(\mathbf{q}_0 \pm \mathbf{G}_2)|^2} = 1 + 2\Big[-\cos(\theta_{AB})\sqrt{P_A P_B} - \cos(\theta_{DC})\sqrt{P_D P_C} + \cos(\theta_{BC})\sqrt{P_B P_C} + \cos(\theta_{DA})\sqrt{P_D P_A} - \cos(\theta_{DB})\sqrt{P_D P_B} - \cos(\theta_{AC})\sqrt{P_A P_C}\Big] \tag{2.36}$$

$$M^{-2}\frac{n(\mathbf{q}_0 \pm \mathbf{G}_3)}{|\tilde{W}(\mathbf{q}_0 \pm \mathbf{G}_3)|^2} = 1 + 2\Big[-\cos(\theta_{AB})\sqrt{P_A P_B} - \cos(\theta_{DC})\sqrt{P_D P_C} - \cos(\theta_{BC})\sqrt{P_B P_C} - \cos(\theta_{DA})\sqrt{P_D P_A} + \cos(\theta_{DB})\sqrt{P_D P_B} + \cos(\theta_{AC})\sqrt{P_A P_C}\Big] \tag{2.37}$$

$$\mathbf{q} - \mathbf{q}_0 = 2\mathbf{G}$$

: Since $2\mathbf{G}\cdot(1/2)\mathbf{a}_j = 2\pi\delta_{i,j}$, the interference is always 1. This implies that the weight in the 0th and 2nd order peaks only differ from the weight of the Wannier function in momentum space.

$$M^{-1}\frac{n(\mathbf{q}_0 \pm 2\mathbf{G})}{|\tilde{W}(\mathbf{q}_0 \pm 2\mathbf{G})|^2} = 1 + 2\sum_{i>j}\sqrt{P_i P_j}\cos(\theta_{ij}) \tag{2.38}$$

Now, we focus on ground state of the superlattice lattice, in which case $\mathbf{q}_0 = \mathbf{0}$ and all the coefficients c_i are real. We define experimentally measurable quantities $\tilde{P}_i$ as [44, 49, 50]

$$\begin{aligned}\tilde{P}_i &= \left(\frac{n(\mathbf{G}_i) + n(-\mathbf{G}_i)}{2n(\mathbf{0})}\right)\cdot\frac{|\tilde{W}(\mathbf{0})|^2}{|\tilde{W}(\mathbf{G}_i)|^2} \\ &= \left(\frac{n(\mathbf{G}_i) + n(-\mathbf{G}_i)}{2n(\mathbf{0})}\right)\cdot\left(\frac{n(\mathbf{0})}{n(2\mathbf{G}_i)}\right)^{\frac{1}{4}}\end{aligned} \tag{2.39}$$

where the last line follows from Eq. 2.34 and 2.38, and the approximation that the Wannier function in momentum space is Gaussian. Note that $\tilde{P}_i$ is related to the fractional population of atoms in a unit cell, which is dependent on the superlattice geometry, through Eq. 2.34 to 2.38. Therefore, we can characterize the superlattice geometry through measurements of $\tilde{P}_i$. For an ideal kagome lattice, one site in a unit cell is eliminated and the other three sites are equal in energy, giving $P_A = P_B = P_C = 1/3$ and $P_D = 0$. From Eq. 2.34 to 2.38, we have $\tilde{P}_1 = \tilde{P}_2 = \tilde{P}_3 = 1/9$.

Chapter 3

Experimental Apparatus

The two ingredients that make up our quantum simulator are ultracold atoms and the optical lattices. We will first briefly describe the apparatus that produces ultracold atoms. Then, we will focus on two major upgrades on the optical lattice setup, namely (1) a new SW lattice setup based on frequency doubling, and (2) an improved phase lock system which allows arbitrary control of lattice relative phases.

3.1 Ultracold atoms

The apparatus that produces ultracold atoms for our experiments is described and explained in details in the theses of previous group members [49, 50, 47]. In short, our current apparatus is capable of producing ultracold rubidium-87 atoms in the quantum degenerate regime. A series of standard techniques are employed to reduce the temperature of atoms down by nine orders of magnitude, from slightly above the room temperature down to hundreds of nanokelvin. These techniques include a Zeeman slower [51], a magneto-optical trap [52], microwave evaporation [36, 35] and optical evaporation [53]. The mechanism of each of these techniques is extensively discussed in the literature. The actual implementation and practical details are found in the theses cited above.

As rubidium-87 is a bosonic isotope, when a gas of such atoms is cooled to sufficiently low temperatures they form a Bose-Einstein condensate (BEC), where the ground state of the system is macroscopically occupied. On a typical day, we produce pure (no discernible thermal fraction), optically trapped BECs with properties listed in Table 3.1.

Number	Trap frequency	Peak density	Thomas-Fermi Radius	Chemical potential
5×10^4	$2\pi\times$(23, 41, 46) Hz	$3\times10^{13}\mathrm{cm}^{-3}$	(12, 9, 8) μm	$h\times$300 Hz

Table 3.1: Properties of a typical BEC.

To probe the atoms, we perform absorption imaging with a simple imaging system consisting of an objective lens (150 mm, NA = 0.17), a focusing lens (300 mm) and a CCD camera (Stingray from Allied Vision). The magnification of this imaging system is 2.0 and the imaging resolution is 4 μm.

3.2 Bichromatic triangular superlattices

As explained in Chapter 2, our scheme of creating an optical kagome lattice requires (incoherently) superimposing two non-retroreflecting, triangular lattices at a 2-to-1 wavelength ratio. In the original superlattice setup, two independent laser sources are used to generate these two lattices – a 18W Verdi laser from Coherent for the SW lattice, and a Nufern fiber amplifier seeded by Mephisto MOPA from Coherent for the LW lattice.

The relative position between the two lattices needs to be actively stabilized, otherwise the superlattice geometry varies over time. Stabilizing the relative position, or phase, between two non-retroreflecting lattices at different colors is not a trivial task. The details of the original phase stabilization system in the experiment can be found in Ref. [47]. The basic idea of the system is the following: consider a pair of beams, beam 1 and beam 2, at wavelength λ. We want to fix their relative phase at a certain position $\mathbf{r}$ (say this is the center of the atomic gas), where the two beams overlap and interfere non-colinearly with phase θ_1 and θ_2. To do so, we let the beams propagate further, and combine the beams again, say on a beam splitter, at $\mathbf{r}'$, where the phases of the two beams are θ_1' and θ_2' respectively. We measure the combined beam on a photodiode to extract phase information through the interference signals. Using electronic feedback, we enforce the phase condition $\theta_1' - \theta_2'$ at the combining cube. Note that $\theta_{1'(2')}$ and $\theta_{1(2)}$ are related only by the light propagation phase $\int \mathbf{k} \cdot d\mathbf{r}$. If the light propagation phase is constant, enforcing a phase condition at $\mathbf{r}'$ automatically fixes the phase relation at $\mathbf{r}$. For each color, we designate one beam as the reference beam and fix the phases of the other two beams relative to it. The relative phases are locked to zero, i.e. a constructive-interference condition. When all the lattice phases are locked, we have two triangular lattices with fixed positions in real space. To allow adjustments on the relative positions of the two lattices between different experimental runs, a pair of dispersive glass wedges is intentionally added to one path of the interferometer. Varying the total thickness of the glass wedge in the interferometer path changes the propagation phase differentially for the two colors. This results in a change in the relative position between the two lattices (and therefore a different lattice geometry), on top of a common displacement for both lattices which has no physical significance.

One of the biggest issues of this scheme comes from the combination of the using of two separate lasers to generate the two lattices, and the unequal path lengths from the combining cube to the location of atoms. Consider a laser frequency shift of $f \to f + \Delta f$ and an interferometer with path length difference ΔL. This leads to a displacement of the lattice relative to its original position:

$$\frac{\Delta(\theta_1 - \theta_2)}{2\pi} \times \lambda = \frac{\Delta f}{f} \Delta L \tag{3.1}$$

When the two laser sources have independent frequency drifts, the two triangular lattices displace from each other and the resultant superlattice geometry changes.

For the rest of this chapter, we detail two major technical upgrades on the superlattice setup. The first one is a new SW lattice setup that involves a high power, frequency doubling system that converts 1064-nm light into 532-nm light. With this system, all the beams used to create the superlattice are delivered from one single light source. In case of frequency drifts, the fractional change $\Delta f/f$ would be the same for both colors, thus resulting in a slow drift in the absolute position of the superlattice but no distortion in the geometry. The second one is the extension of an existing phase lock system that leads to the capability of setting an arbitrary relative phase condition between lattice beams. In other words, $\theta_1' - \theta_2'$ can be flexibly locked to any values, not just zero. Such a seemingly small extension to the system opens up a lot of experimental possibilities.

Both upgrades are motivated by needs from experiments reported in this dissertation. Experiments performed with the trimerized kagome lattice (Chapter 4) demand a very stable superlattice geometry due to the linear sensitivity of this lattice geometry on its linear sensitivity on relative lattice displacements. With our original setup, data taking relied on random, temporary pauses of the Verdi laser's random drift. The upgraded setup creates a superlattice whose geometry is completely immune to frequency drifts of the laser source.[1] Another experiment-motivated need comes from the exploration of the kagome band structure reported in Chapter 5. In that experiment, we can only accelerate atoms to quasimomenta along a single direction using an out-of-plane optical beam that is aligned to a specific position in advance. A flexible method to accelerate the atoms in arbitrary directions is needed for full exploration of the band structure. We can do that with the upgraded phase lock system, which allows us to lock the lattice phases to time-varying lock points, thus "accelerating" the lattice, instead of the atoms, in arbitrary directions. The two upgrades therefore respectively improve the *stability* and *flexibility* of the superlattice setup.

[1] The original setup also has other minor problems. For example, the Verdi laser has pronounced intensity noise peaks at 375 Hz and its harmonics, close to the typical energy scale of our lattice system. Another problem is that the 532-nm light is delivered in free space, through a total path length of 3 m from the laser to the position of atoms. One obvious problem is the difficulty of beam alignment. For example optimizing alignment through an accousto-optical modulator placed upstream in the beam path unavoidably misaligns the beam from the atoms. Moreover, due to high beam power, optics in this set up become damaged quite often. As a result, the spatial profiles of lattice beams get deteriorated. Such low-quality laser beams lead to various problems, including insufficient lattice depth (as they cannot get focused down nicely) and even anomalous data sometimes. These problems are mitigated in the new system, where lattice beams are delivered from the laser source to the atoms through optical fibers.

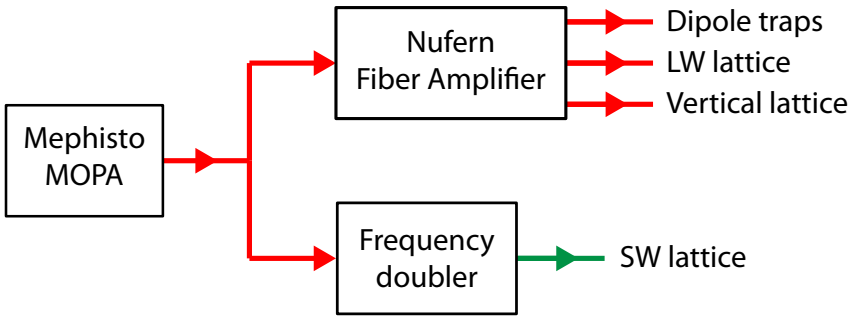

Figure 3.1: High-level schematic for generating trapping beams and lattice beams used in the experiment. In this scheme, all beams have a common origin from the Mephisto MOPA.

3.3 Frequency doubling and SW lattice

The Mephisto MOPA is the most powerful and stable laser in our lab. It outputs 40 W of 1064-nm light with a linewidth of 1 kHz (for a measurement time of 100 ms) and a measured frequency drift on the order of 10 MHz/hr. We take advantage of the high output power of this laser and construct a system that relies on this laser only to create all the lattice beams. A small amount of power ($\sim$ 150 mW) is taken from the MOPA's output and used to seed the Nufern amplifier, which outputs about 10 W of amplified 1064-nm light. The major portion of the MOPA output power is frequency-doubled to generate 532-nm light through the process of second harmonic generation. See Fig. 3.1 for a high level schematic.

In the following section, we focus on the part of frequency doubling and the construction of the SW lattice setup. Details on the dipole trap, LW lattice and vertical lattice setups can be found in [50].

3.3.1 Second harmonic generation

We start by briefly describing the theory of second harmonic generation, a process in which nonlinear response of a dielectric material to electric field is utilized to convert light at one frequency (fundamental) into another one at twice the frequency (second harmonic). See for example [54] for a complete coverage of the subject.

Nonlinear response

When an electric field $\mathbf{E}(t)$ passes through a dielectric media, bound electrons inside the material feel a force and move away from their equilibrium position. The material acquires polarization $\mathbf{P}$. When the electric field is small, we can assume linear responses from the system, and $\mathbf{P}(t) = \epsilon_0 \chi \mathbf{E}(t)$ where ϵ_0 is the electric permittivity of free space and χ is the electric susceptibility which quantifies how polarizable a material is. When the electric field

becomes strong, we need to consider nonlinear effects. The field-induced polarization can be written in the following general form

$$\mathbf{P}(t) = \epsilon_0 \left[\chi^{(1)}\mathbf{E}(t) + \chi^{(2)}\mathbf{E}^2(t) + \chi^{(3)}\mathbf{E}^3(t) + \cdots \right] \tag{3.2}$$

where $\chi^{(n)}$ is the n-th order electric susceptibility. In the harmonic oscillator model for bound electrons, higher order susceptibilities come from corrections to an imperfect harmonic potential. The symmetry of a crystal could enforce some of these higher order terms to vanish. For example, inversion symmetry dictates that $\chi^{(2)}$ vanishes. Therefore, a nonlinear crystal without inversion symmetry is needed for second harmonic generation. One expects nonlinear terms ($n \geq 2$) start to matter when the applied electric field is somehow comparable to the nuclear electric field $\simeq 10^{12}$ V/m that binds the electrons to the ions. By $I = 1/2\epsilon_0|E|^2$, beam intensity on the order of 10^5 W/mm^2 is required to induce observable nonlinear effects.

Phase matching

Second harmonic generation takes place as the fundamental wave travels along the nonlinear crystal. We want to ensure that the second harmonic waves created at different positions are added up in phase such that the total wave amplitude builds up, instead of averaging out because of destructive interference. In the ideal phase matching condition where the fundamental and second harmonic waves travel at the same phase velocities in the nonlinear material, the second harmonic wave amplitude is added up constructively everywhere and therefore its power is maximized. Recall that phase velocity is given by ω/k. Since the frequencies of the two waves have a definite 1-to-2 ratio as dictated by conservation of energy, the phase matching condition is therefore

$$\Delta\mathbf{k} = \mathbf{k}_2 - 2\mathbf{k}_1 = 0 \tag{3.3}$$

where the index 1(2) refers to the fundamental (second harmonic) wave. Alternatively, as λ is rescaled to λ/n in a medium of refractive index n, the phase condition can be rewritten as $\Delta n = n_2 - n_1 = 0$. In general, these nonlinear crystals are dispersive, and therefore the phase matching condition is not satisfied. If $\Delta\mathbf{k} \neq 0$, the relative phase between the fundamental and second harmonic waves advances by π over a distance of $\pi/|\Delta\mathbf{k}| = \lambda/(2\Delta n)$, typically on the order of μm.

There are different tricks to make the phase condition apply. One of them is by periodically modulating the nonlinear property of the dielectric material. The most common technique is *periodic poling*, where the orientation of the birefringent material is reversed periodically over distances around the coherence length $d_c = 1/2 \times \pi/|\Delta\mathbf{k}| = \lambda/\Delta n$. By doing so, the phase of the second harmonic wave reverses sign when the accumulated phase is about to go past $\pi/2$. As a result, the field amplitude does not get averaged out, albeit the accumulation is not completely constructive. This is known as the quasi-phase matching condition.

3.3.2 Frequency doubling system

Having discussed the basics of second harmonic generation, we now describe the experimental setup. The frequency doubling system, as well as the lattice-beam preparation section, are built on the same single optical table and are housed in an enclosure.

Generic Considerations

Below are some considerations regarding handling high power laser beams in the setup:

- There is no optical isolator for Mephisto MOPA in this setup. There was one when the system was initially built. Later, we noticed that the isolator severely distorts the spatial beam mode and reduce the frequency doubling efficiency, even though we were using one that is designed for handling high intensity beam and our laser intensity was way lower than the damage threshold. This distortion happens only at high power, therefore it is likely some thermal effect in the Faraday rotator. An engineer from Coherent, as well as people from some other research groups, have told us that an external isolator is unnecessary. The isolator was then taken out and we have not seen a problem with the Mephisto MOPA over three years of operating time.

- The output power of our Mephisto MOPA is 40W (nominally 43W). Such a high power beam should be handled with care. A few sets of halfwave plates and polarizing beam splitters (PBS) are put into the setup for power adjustment so that different sections of this setup can be sequentially turned up after alignment at low power is done. Thin film plate polarizers are used as they are in general more tolerant to high power compared to PBS. However, even these plate polarizers could be damaged by the high power beam over time. In our previous setup with the high power Verdi laser, we have seen that the transmitted beam of a damaged PBS is more susceptible to spatial mode distortion than the reflected beam. In this setup, the beam that goes into the nonlinear crystal undergoes multiple reflections on PBS but no transmission, as a clean spatial mode of this beam is required for good conversion efficiency.

- There is a lot of beam power that needs to be dumped in this setup. Under normal operation condition, about 20W of 1064-nm light is left unconverted going through the nonlinear crystal. This light is in generally dumped but not recycled for other purposes, as it has a very non-Gaussian profile. Dumping the power inside the enclosure that houses the system is undesirable, as it causes the local temperature to rise, misaligning optics. We have seen increase in temperature by a few degrees because of this dumped power. For this reason, most beams are redirected to outside of the enclosure for dumping.

Regarding the last point, for the purpose of facilitating thermal equilibration, the enclosure is partially open. However, this allows dust to creep into the setup and cause damages on optics when it is burnt by the high power laser beam. It also makes the setup susceptible

to air current and temperature fluctuations in the laboratory. A better solution is to build an air circulating system that passes temperature-controlled, laminar flow of air through the whole setup. This would be an important upgrade to the system in the future.

Frequency Doubling Crystal

We implement a single-pass frequency doubling scheme (see Fig. 3.2) with a periodically poled Mg-doped stoichiometric lithium tantalate (PPMgSLT) crystal, purchased from a Japanese company OXIDE. Stoichiometric lithium tantalate is a nonlinear crystal suitable for high-power SHG in the UV to mid-IR range. It has many desirable properties as a frequency doubler [55], including a high thermal conductivity and a high nonlinear coefficient. Especially when doped with magnesium, it is also less susceptible to detrimental processes like photorefractive damages and green-induced infrared absorption, which limits the conversion efficiency in practice, compared to some other nonlinear materials. According to specification, the crystal is able to perform second harmonic generation with 33W input and 10W output, or an efficiency of 30%.

The crystal has a size of 0.5mm (H) $\times$ 2mm (W) $\times$ 30mm (L) mm. It is housed in a aluminum mount, which is temperature stabilized by a thermoelectric cooler. This mount sits on a 5-axes translational stage.

We focus the MOPA output beam from a $1/e^2$ radius of 1 mm down to 68 μm, with a 200 mm lens. An important factor that determines the conversion efficiency is the focusing parameter $\xi = l/b$, where l is the length of the doubling crystral, and $b = (2\pi n_1/\lambda_1)w^2$ is the confocal parameter, with n_1 being the refractive index of the crystal at the fundamental wavelength λ_1 and w the focused beam size. In our setup, $\xi = 0.52$. This is quite different from the theoretical optimum value of $\xi = 2.84$. This is potentially a parameter to be improved in the future if more power is needed. However, the current focusing condition has provided us a satisfactory amount of output power at 532 nm that is close to the specification.

Performance

In Fig. 3.3, we show the variation of second harmonic output power from the frequency doubling setup as a function of the fundamental input power. The power is measured with a fixed beam alignment but at different optimized temperatures (further details in the discussion later in this section). The output power is measured after two consecutive dichroic mirrors placed after the crystal for separating the fundamental and second harmonic waves. This induces a total transmission loss of 6%.

In Fig. 3.3 (a), we directly plot the output power versus the input power. Under typical operation condition, we send 30 W of input power into the doubling crystal, getting 9.3 W (or 9.8 W after correction of transmission loss) of output. The conversion efficiency is 31% at this input power, consistent with the spec value. In Fig. 3.3b, the same data are plotted with the input power squared. The data show nice quadratic dependence until the input power goes above $\sqrt{600} \simeq 24$ W. This deviation can be attributed to depletion of the

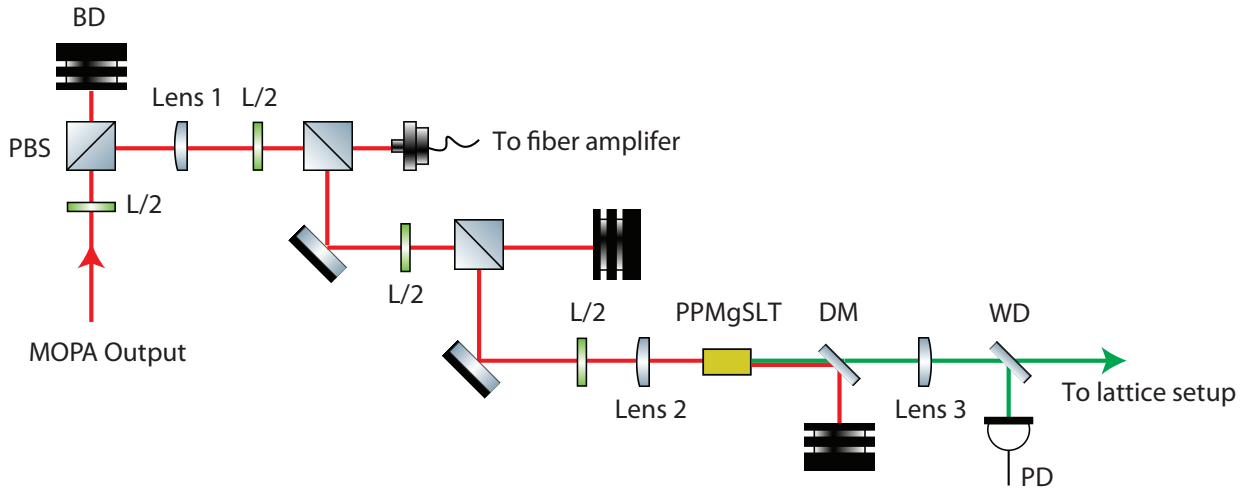

Figure 3.2: Schematic of the single-pass frequency doubling setup. The output power of Mephisto MOPA is used for seeding another fiber amplifier and also frequency doubling. Lens 1 (700 mm) corrects for the slight divergence of the Mephisto MOPA output. Lens 2 focuses the 1064-nm beam (see text) through the nonlinear crystal and Lens 3 defocuses the output frequency-doubled beam. Two dichoric mirrors (only one is shown) separates the 1064-nm input and 532-nm output light. A window is used to pick off $< 1\%$ of power for monitoring. Legend: L/2, half waveplate; PBS, polarizing beam splitter; BD, beam dump; DM, dichroic mirror; WD, window; PD, photodiode. We acknowledge Alexander Franzen for making the vector graphics library which provides templates used in this figure, as well as Fig. 3.6, 3.8, 3.9.

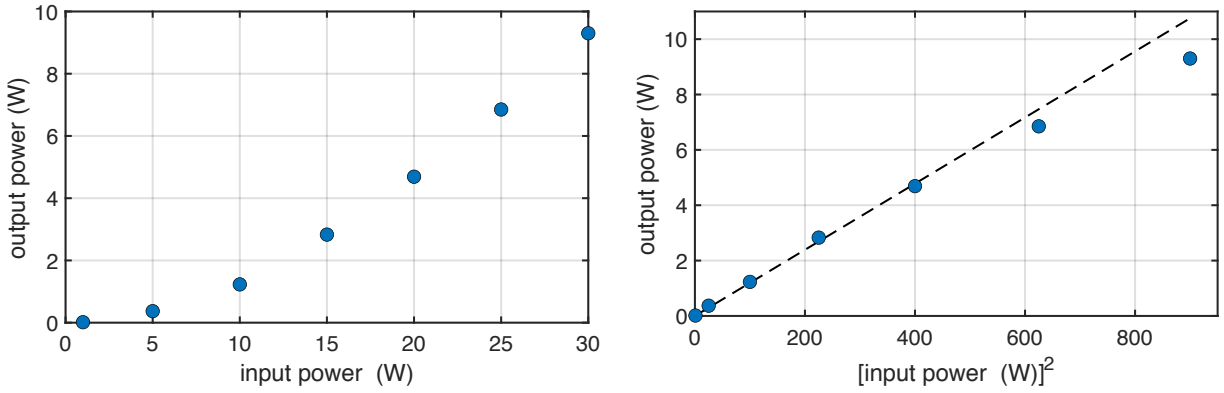

Figure 3.3: Frequency doubling efficiency. Variation of 532-nm output power versus 1064-nm input power (a) and input power squared (b).

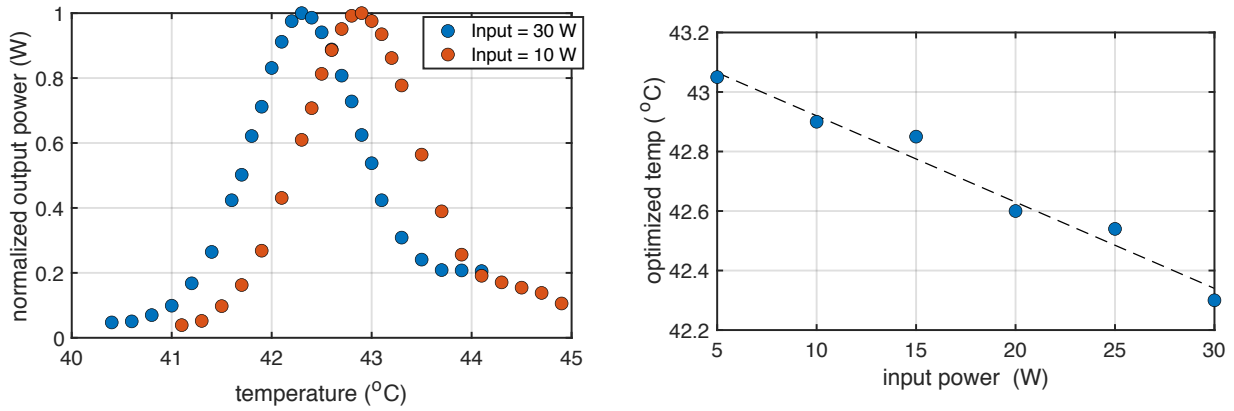

Figure 3.4: Temperature tuning of the frequency-doubling crystal. (a) Normalized output power of the doubling crystal at two different input power (10 W and 30 W) measured with fixed beam alignment. (b) Optimized crystal temperature at different input power.

fundamental wave or thermal dephasing [56]. Thermal dephasing is a common problem in second harmonic generation associated with absorption of the optical power in the crystal. It therefore causes local variations in the refractive index and breaks the phase-matching condition.

The crystal temperature, as stabilized by a thermoelectric cooler in the setup, is a crucial parameter as it sets the phase matching condition. We measure the variation of the output power as a function of crystal temperature at different values of input power. In Fig. 3.4 (a), two such measurements taken at 10 W and 30 W of input power are shown. In both cases, a clear maximum can be identified, which corresponds to the temperature that best satisfies the phase matching condition given a particular beam alignment. The lineshape, however, deviates from the theoretically predicted $sinc^2$ function. A Gaussian fit to the 30 W data excluding those at < 0.2 normalized power gives a FWHM of 1.39(2) °C, slightly larger than the predicted value of 1.08 °C[56]. In Fig. 3.4b, we plot the dependence of the optimized temperature on the input power. At increasing operating power, the crystal absorbs more power from the beams and heats up. A lower set temperature corrects for that to maintain the optimized phase matching condition. A linear fit to the data gives -0.03(1) °C/W.

Fig. 3.5 shows the second harmonic power as a function of time. Two data sets taken under different conditions. The first data set was taken after a major alignment of the doubling crystal was performed, and the temperature of the crystal was scanned to maximize the conversion efficiency before the measurement. The power drops by about 5% in the first hour, and a couple percent more over the next few hours. The fluctuations in the power also grow, presumably due the input beam drifting away from the optimal position and thus the system becoming more susceptible to pointing noise in the input beam. This drift in beam alignment is attributed to thermal equilibration of the crystal and its mount. The second

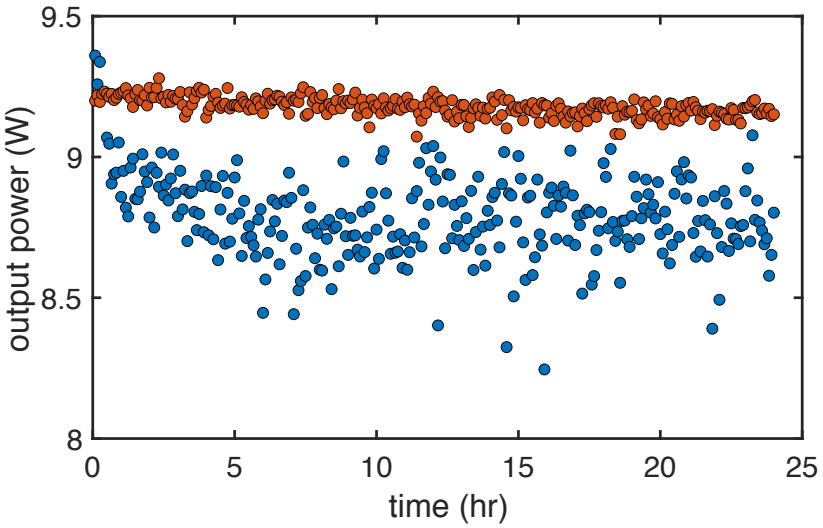

Figure 3.5: Time variation of the output power of the frequency doubling. The first set of data (blue circles) was taken after beam alignment and temperature optimization. After a few days, the input beam was realigned at a constant temperature, and a second set of data was taken (orange circles).

data set was taken after the system was realigned without changing the temperature a few days after the first data set was taken. For this data set, the output power is much more stable. It is important that every time the temperature of the crystal is adjusted, perhaps for accommodating the change in beam alignment and phase matching condition, the system needs to be realigned for stable operation.

3.3.3 SW lattice setup

The frequency doubled light enters a lattice-preparation setup, where the 532-nm light generated is split up and manipulated by optical devices. The overall amount of power going into the lattice section is controlled by a combination of halfwave plate and Glan-Calcite Polarizer (Thorlabs GL15-A), which is designed to offer purely polarized transmitted light at high beam power.

In the lattice section, the beam is split into three paths using non-polarizing beam splitters. To control the intensity and phase of the lattice beams, an acousto-optic modulator (AOM) is added to each path. We drive these AOMs with RF signals generated by waveform generators (Keysight 33512 A/B) and then amplified. The RF output power and phase of these generators are controlled by electronic feedback systems, so that the intensities and phases of the first order diffraction beams are set to desired values. We use only the first-order diffracted beam of the AOM and dump the zeroth order. One of the beams, which

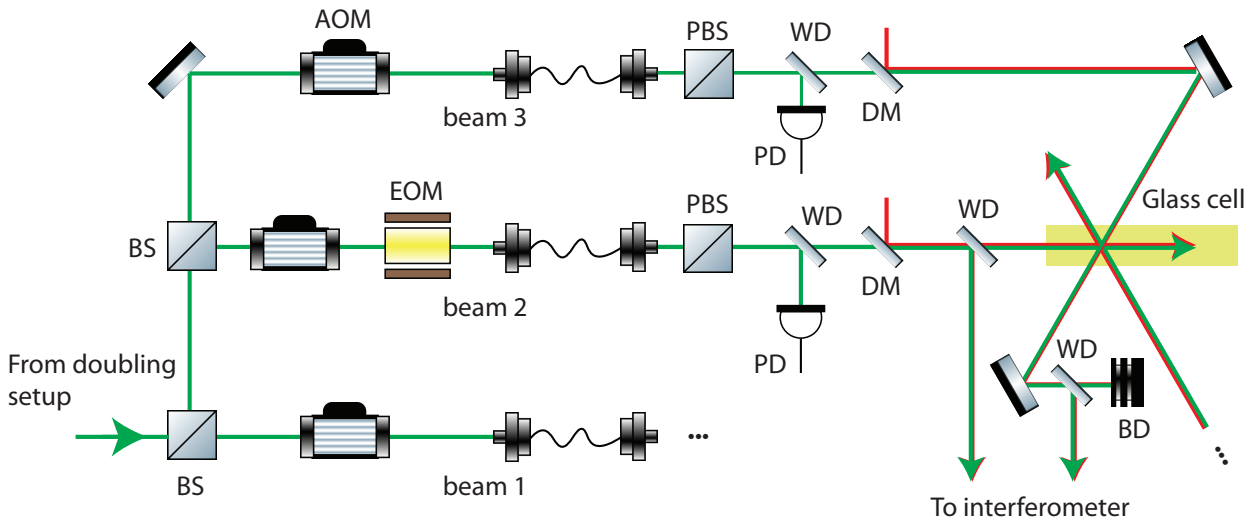

Figure 3.6: SW lattice setup. The frequency-doubled light is split into three beams for the construction of the SW lattice. Each beam goes through an AOM, which is independently driven. The reference beam (beam 2) also goes through an EOM. All three beams are delivered through photonic crystal fibers to the science table, where they are combined with the LW lattice light to generate the superlattice. A small fraction of power is picked off from each beam twice for intensity and phase stabilization respectively. Legend: BS, beam splitter; PBS, polarizing beam splitter; WD, glass window; PD, photoiode; DM, dichroic mirror; BD: beam dump.

serves as the reference beam to which the phases of the other two lattice beams are locked relative to, also goes through an electro-optical modulator (EOM), which puts on sidebands on this beam as part of the phase lock scheme (see next section).

The lattice beams are then delivered to the science table (where the experiment actually takes place) through polarization-maintaining photonic crystal fibers (LMA-PM-10 from NKT Photonics). These fibers are high index guiding fibers made up of pure fused silica. In such a fiber, a solid core with high refractive index is surrounded by a patterned array of hollow cores. This microstructured pattern can be engineered to make photonic crystal fibers go beyond the limitations of conventional optical fibers. For example, the photonic crystal fibers we use have a mode field diameter of 8.4 μm at 532 nm. This is a factor of $2-3$ larger than that for a conventional polarization maintaining optical fiber that works at 532 nm. The peak intensity in the fiber is thus reduced by the same factor squared, reducing the risk of damages.

On both sides of the fiber, collimators 60FC-4-A18-01 from Schäfter Kirchhoff are used. These collimators are monolithic aspherical lenses, which are better for handling high power beams than other models where multiple lenses are glued together for better aberration

correction.

Immediately after coming out of a fiber and going through a polarization clean-up cube, a beam is sampled by a window. A small amount of picked off power is directed onto a photodiode with logarithmic scaling for intensity stabilization purposes. See Ref. [50] for details. Because of the position of the photodiode, the power to voltage conversion does not change with day-to-day drift in beam alignment. The transmitted beams through the window combine with the 1064-nm beams that are prepared in a separate section [50] on dichroic mirrors. The combined beams are then directed onto the atoms along three directions intersecting at 120° degrees. The SW lattice beams are focused down to 75 μm at the location of the atoms, creating a SW triangular lattice.

As explained earlier in this section, the phases of the lattice beams need to be actively stabilized. We sample the lattice beams with glass windows, and measure their phases interferometrically. This will be the focus of section 3.4.

3.3.4 Stability test

The main purpose of constructing this new frequency doubled SW lattice system is to create a bichromatic lattice with geometry that is stable and immune to drifts in laser frequency. We test the stability of the system with the most sensitive superlattice we have worked with - the trimerized kagome lattice.

Fig. 3.7 shows the results of two different tests. In the first test, we prepare a optical trimerized kagome lattice at $(V_{\mathrm{SW}}, V_{\mathrm{LW}}) = (50, 13)$ kHz and take diffraction images with a superfluid in this lattice. We take around 30 repeated shots. From the diffraction images, we extract the $\tilde{P}$ quantities which reveal the populations in the four sites of a unit cell of the superlattice (see section 2.5 or Ref. [44, 49, 50]). For an ideal kagome lattice, trimerized or normal, the three $\tilde{P}$ values should all be $1/9 = 0.11$. The data clearly show that the superlattice keeps its geometry throughout 30 shots, which takes about half an hour to finish. As explained earlier in this chapter, with the original system, a stable trimerized kagome lattice is possible only when the laser temporarily pauses its random drifts. It is quite often the case that the geometry drifts away only a few minutes after we find a good setting adjusting the glass wedges. With the new setup, a stable superlattice geometry is guaranteed by construction.

In the second test, we look at the stability of the TKL over a longer time scale. We take 3-5 repeated shots to look at the superfluid diffraction as before at three different times in a day, with time intervals of 1.5 hours and about 3.5 hours respectively. The frequency of the Mephisto MOPA drifted by about 30 MHz between each set of measurements. From the extracted $\tilde{P}$ values, we see that in the first 1.5 hours, the change in $\tilde{P}$ is smaller than statistical error and thus is insignificant.

In the third measurement, the geometry has clearly drifted away. We thus put a lower bound of 1.5 hours on the stability of the trimerized kagome lattice geometry. Further investigations are needed to identify the cause of the drift in the last measurement . Interleaved lattice balance checks throughout this experiment rule out the possibility that the super-

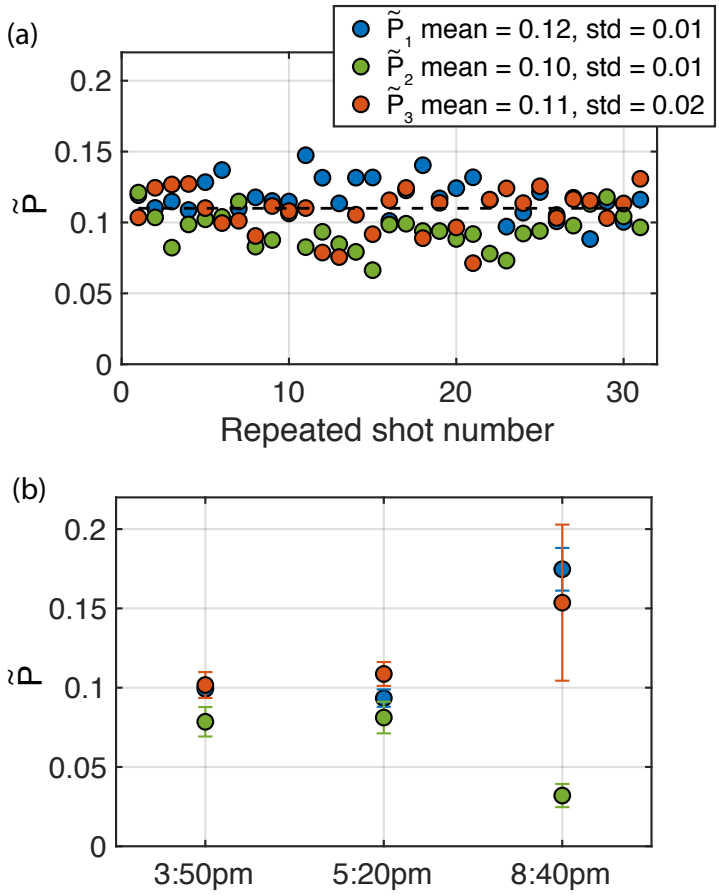

Figure 3.7: Stability of TKL created with the new lattice system. (a) Repeated measurements of $\tilde{P}$ values measured with superfluid diffraction. (b) Averaged $\tilde{P}$ values over 3-5 shots measured at three different times in a day. The Mephisto MOPA frequency changes by 30 MHz between the first and second data set, as well as the second and third data set.

lattice geometry change comes from power imbalance in individual triangular lattices. The relative phases of the lattice beams might change for reasons other than laser frequency change. For example, a change in air pressure in the laboratory may cause a sufficient drift in relative path lengths to explain these data [47].

3.4 Arbitrary phase control system

In the previous section we assume that a boundary phase condition is enforced by feedback at the position where lattice beams are combined, and we focus on maintaining the mapping between this phase condition and the one at the atoms' location. In this section, we switch our focus to the scheme for establishing such a boundary phase condition. The idea of

the original scheme [47] is summarized as follows. Suppose we want to lock the phase θ of a lattice beam relative to a reference beam. We phase-modulate the reference beam by an EOM to put on two sidebands to its carrier frequency so that lock-in detection can be implemented. We combine these two beams and measure their interference on a photodiode. By demodulating the photodiode output, a signal that varies with $\sin(\theta)$ is obtained. This serves as an error signal which, after being processed by a loop filter, can be fed to the signal generator whose output drives the corresponding lattice AOM in the setup (see Fig. 3.6).

The major limitation of this setup is its limited lock range. The error signal is derived from a sinusoidal interference signal. We typically lock to the zero crossing of the error signal. If one attempts to adjust the lock point by $\pi/2$, the slope of the error signal becomes zero and the lock fails. Therefore the adjustable range for lock points is limited to $\pm\pi/2$. The dispersive glass wedges can be used to adjust the relative phases of the lattice beams at the atoms over a large range (multiple 2π) by changing the propagation phases of the beams in the interferometer (see chapter 3.2 and Ref. [50]). However, the glass wedges are controlled by actuators and can only respond on the time scale of seconds. Therefore they are only used for adjusting superlattice geometry between different experimental runs.

The capability of changing the relative phases dynamically (with sub-ms timescale) over a wide range (beyond $\pm\pi/2$ or even multiple 2π) opens the door to various possible experiments. For example, it would allow quick distortion of the unit cell, which can be useful for initial state preparation (e.g. loading into an inverted triangular lattice [50]), wavefunction engineering (e.g. phase imprinting), as well as state detection (e.g. site mapping). Sweeping the relative phases continuously, one can also implement moving lattices to study atoms with non-zero quasimomenta in ground and excited bands in the lattice frame [57].

For retroreflecting lattices, the phase boundary condition is enforced physically with a mirror. The relative phases of lattice beams at the atoms' position can be changed rapidly by jumping the lattice beam frequencies. In our experiment, we cannot do the same because changing frequency would result in the disengagement of the phase lock.

In this section, we discuss an upgraded phase lock system which is based on a new scheme to generate the phase lock error signal. Under this scheme, the relative phases can be locked to an arbitrary value. A couple of examples will be given to illustrate to use of this system.

3.4.1 Scheme of generating error signals

The idea of the new scheme is essentially the IQ modulation technique in RF technology. In this technique, phase modulation is implemented by amplitude-modulating two sinusoidal signals, commonly referred to as the I (in phase) and Q (quadrature) components, that are $\pi/2$ out of phase. This is easy to understand if one considers the following basic trigonometric relation

$$\sin(\theta+\phi) = \sin(\phi)\underbrace{\cos(\theta)}_{I} + \cos(\phi)\underbrace{\sin(\theta)}_{Q} \tag{3.4}$$

Clearly, amplitude-modulating the I and Q components corresponds to phase-modulating the combined signal. For example, to shift the phase of the combined signal from 0 to $\pi/2$, we change the scaling factors of I and Q from $\sin(0) = 0$ and $\cos(0) = +1$ to $\sin(\pi/2) = +1$ and $\cos(\pi/2) = 0$.

The same idea can be applied to generate an error signal with flexible phase offset in our phase lock system. In our case, I and Q correspond to two $\pi/2$-shifted sinusoidal signals whose arguments are the relative phase θ between two lattice beams. In the original phase lock system, the interference between the sidebands on the reference beam and the other lattice beam provides a $\sin(\theta)$ term (Q). All we need is to generate the other quadrature (I).

With RF signals, I and Q can be generated by splitting a sinusoidal signal and delaying one of them by a quarter of a cycle, say with a delay line. In optics, a quarter-waveplate can achieve the same purpose – it introduces a $\pi/2$ differential phase shift between light linearly polarized along its slow and fast axes. To obtain I and Q for the phase lock, we let one of the two beams become circularly polarized by passing through a quarter-waveplate. We then combine the two beams on a beamsplitter cube. The combined beam show interference along its two orthogonal polarizations, but with phases of θ and $\theta + \pi/2$ respectively. Measuring these interference signals on separate photodiodes, we obtain the I and Q components we need. The two components are then scaled and summed to produce the desired signal. This technique is referred to as quadrature detection in the literature, and has various applications including image reconstruction and lidar [58, 59].

Optical signal

Let's be more concrete and describe the scheme in mathematical terms. Suppose we have two beams [2]with electric field $\mathbf{E}_1$ and $\mathbf{E}_2$ with equal amplitude E_0. Beam 2 with electric field $\mathbf{E}_2$ serves as the reference beam and is phase-modulated by an EOM at a frequency Ω with small modulation depth M. Both beams begin with linear polarization $\hat{x}$ (say parallel to the optical table). To perform quadrature detection, we send beam 2 through a quarter waveplate such that it becomes circularly polarized. We write down the electric field of the two beams at the location of the combing cube:

$$\begin{aligned} \mathbf{E}_1(t) &= E_0 e^{i\omega t + i\theta}\hat{x} \\ \mathbf{E}_2(t) &= E_0 e^{i\omega t + iM\sin(\Omega t)}\left(\frac{\hat{x}+i\hat{y}}{\sqrt{2}}\right) \\ &\simeq E_0 e^{i\omega t}(1 + iM\sin(\Omega t))\left(\frac{\hat{x}+i\hat{y}}{\sqrt{2}}\right) \end{aligned} \tag{3.5}$$

Here θ is the phase of beam 1 relative to beam 2 at the combining cube, and $\hat{x} \perp \hat{y}$. We analyze the combined electric field on a PBS that is rotated by $\pi/4$ with respect to the

[2]In the experiment, these are low-power beams picked off from the lattice beams. In this section, they are referred to by the name (Beam 1,2 and 3) of the beams they are picked off from.

table such that the analyzing basis vectors are $\hat{x}' = (\hat{x} + \hat{y})/\sqrt{2}$ and $\hat{y}' = (-\hat{x} + \hat{y})/\sqrt{2}$. The reflected and transmitted beams from the rotated PBS are measured on two separate photodiodes. Consider the intensities of those two beams:

$$\begin{aligned} I_{\hat{x}'} &= |(\mathbf{E}_1(t) + \mathbf{E}_2(t)) \cdot \hat{x}'|^2 \\ &\simeq I_0(1 + \cos(\theta) + M \sin(\omega t) \sin(\theta)) \\ I_{\hat{y}'} &= |(\mathbf{E}_1(t) + \mathbf{E}_2(t)) \cdot \hat{y}'|^2 \\ &\simeq I_0(1 - \sin(\theta) + M \sin(\omega t) \cos(\theta)) \end{aligned} \tag{3.6}$$

where $I_0 = |E_0|^2/2$, and we ignore $\mathrm{O}(M^2)$ terms. From the expression we see that we have created the I and Q components we want optically. Next we need to extract those terms electronically.

Electronic signal

We measure the power of the two beams on two separate photodiodes with transimpedance stages. We obtain electrical signals $V_{1(2)} = \alpha P_{\hat{y}'(\hat{x}')}$, where α is the product of the responsivity of the photodiode and the transimpedance gain, and P is the beam power (which relates to I_0 by some effective area of the beam, which is unphysically represented by a plane wave in this model). After high-pass filtering the signal to remove the $1+\cos(\theta)$ and $1-\sin(\theta)$ terms, we multiply the two signals V_1 and V_2 by scaling factors $S_1(\phi) = \sin(\phi)$ and $S_2(\phi) = \cos(\phi)$ respectively. The two scaled signals are then added up to give

$$\begin{aligned} V &= \alpha P M \sin(\Omega t)(S_1(\phi)\cos(\theta) + S_2(\phi)\sin(\theta)) \\ &= \alpha P M \sin(\Omega t)\sin(\theta + \phi) \end{aligned} \tag{3.7}$$

Finally, we demodulate the signal with $\sin(\Omega t)$ and low-pass filter it. The following signal is obtained:

$$V_{\mathrm{err}} = \alpha' \sin(\theta + \phi) \tag{3.8}$$

which gives us an error signal whose zero crossings are determined by ϕ, a tunable parameter that parametrizes the scaling functions S_1 and S_2. Here α' combines the modulation depth and all the gain parameters involved in the process that turns the optical signals into electrical signals [47].

This scheme is applied to both pairs of beams (beam 1-2 and beam 2-3) for each color, providing a full control over the relative phases of all the lattice beams.

3.4.2 Hardware

In this subsection, we discuss the important hardware components used in the upgraded setup. Components that were present in the old phase lock system and described in [47] will be omitted here.

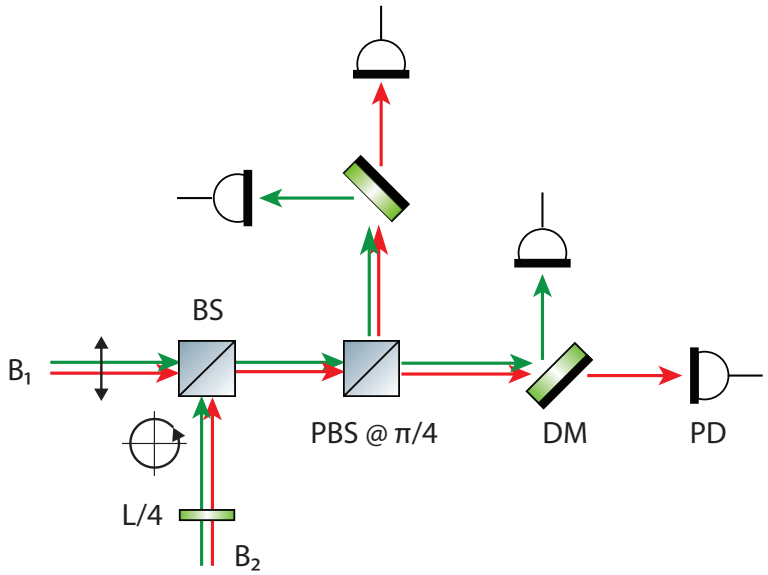

Figure 3.8: Optical part of the new scheme for generating phase lock error signal. Two low-power beams that are picked off from the lattice beams are directed into an interferometer. One of the two beams passes through a quarter waveplate and becomes circularly polarized. The two beams are then combined on a beam splitter. A polarizing beam splitter rotated by $\pi/4$ with respect to the optical table analyzes the combined light and sepeartes it into two orthogonally polarized components. A dichoric mirror separates the two colors for each component. All the beams are detected by separate photodiodes. In the experiment, there are two copies of this setup for the two pairs of relative phases (θ_{12} and θ_{23}) for each color. Legend: L/4, quarter waveplate; BS, beam splitter, PBS: polarizing beam splitter; DM, dichroic mirror; PD, photodiode.

Optical Part

Quarter waveplate In our setup, the lattice beams of the two colors are combined before they are picked off for the interferometer. Therefore dual-wavelength quarter waveplates are needed to circularly polarize both colors. We use the product QWPD-1064-4-532-4-10 purchased from CVI Laser optics. The product has tolerance of $\lambda/100$ on phase retardance.

Combining beam splitter We use the product BSW26 from Thorlabs, which is a thin film plate beam splitter, to combine the lattice beams. The product has angle-dependent birefringence, which limits us from getting true quadrature pairs that are $\pi/2$ out of phase. This problem is addressed in the next subsection.

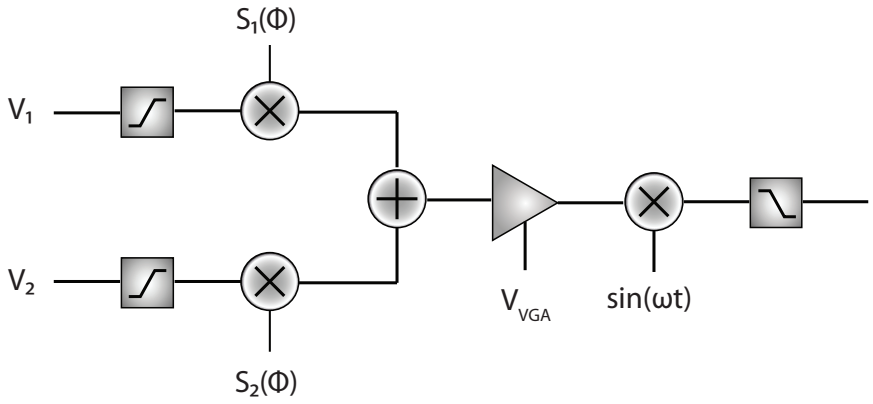

Figure 3.9: Electronic part of the new scheme for generating phase lock error signal. The I and Q components of the optical signal are measured on two separate photodiodes, generating electrical signals V_1 and V_2. These signals are high-pass filtered, multiplied by scaling factors $S_1(\phi)$ and $S_2(\phi)$ respectively, and added up. The combined signal is then amplified by a variable-gain amplifier, whose gain is set by an external voltage V_{VGA}. Finally, after the signal is demodulated and low-pass filtered, an error signal for the phase lock is generated.

Polarizing Beam Splitter We use the product PBS1005-SBB from AT Films. It works over a wide range of wavelengthss that cover 532 nm and 1064 nm, and offers good extinction ratio of 2000:1. To avoid extra birefringence from optics (especially the dichroic mirrors needed for separating the two colors) messing up the phases, we let the combined beams be analyzed by this PBS rotated by $\pi/4$ immediately after the combining beam splitter.

Dichroic Mirrors A combination of various dichroic mirrors from Thorlabs (DMLP and DMSP series) and Newport (10SWF series) are used. The extinction ratio is not crucial as the reference beams of the two colors are modulated at very different frequencies (700 kHz for 532 nm and 20 MHz for 1064 nm). Demodulation picks out the signal at the right frequency only.

Photodiodes For 1064-nm light, we use FS1811 from Newport. The detector material is InGaAs, which has high responsivity at 1064 nm. Those photodiodes have a small detector area (diameter = 300 μm). Typically, we need to focus the beam down for detection. For 532-nm light, we use a combination of PDA36A and PDA100A. Those photodiodes do not have particularly high responsivity at 532 nm, and could be replaced to obtain stronger signals.

Electronic Part

Multiplier To scale the output of the two photodiodes, we use the integrated chip AD835 from Analog Devices. It is a 4-quadrant multiplier – it can handle multiplication of both positive and negative voltages. It has a 250 MHz bandwidth, which is much higher than the modulation frequencies we use.

Adder The addition of the two scaled photodiode outputs is done by a simple inverting summing circuit built with an op amp LM6172.

3.4.3 Practical considerations

In section 3.4.1, we derive the expression of the error signal assuming that the interference signal on the two photodiodes are equal in size and exactly $\pi/2$ out of phase. In practice, there are imperfections in the system that break those assumptions. The major one comes from the birefringence of the combining beam splitter. While imbalance in the size of optical signals can be corrected by attenuation (if not limited by signal to noise), deviation from a true quadrature pair cannot be corrected easily. Both types of imperfections lead to nonlinearity in phase modulation. In the extreme case where one quadrature is practically zero, the error signal is predominantly produced by the other quadrature. Amplitude modulation on the quadrature pair will look only like amplitude (but not phase) modulation on the combined signal.

In fact, we can solve this problem robustly with modified scaling functions that take the above two imperfect conditions into account. Suppose the output of the two photodiodes are $V_1 = A_1 \cos(\theta)$ and $V_2 = A_2 \sin(\theta + \beta)$. We set $S(\phi)$ according to the following expressions,

$$\begin{aligned} S_1(\phi) &= -\tan(\beta)\cos(\phi) + \sin(\phi) \\ S_2(\phi) &= \frac{A_1}{A_2}\frac{1}{\cos(\beta)}\cos(\phi) \end{aligned} \tag{3.9}$$

Then, simple algebra shows $S_1 V_1 + S_2 V_2 = A_1 \sin(\theta + \phi)$.

The values of β and A_1/A_2 can be directly measured by looking at the individual error signals. One could turn all the lattice beams on to some typical power, frequency-detune the beams and look at the error signal produced at the appropriate settings V_{VGA} of the variable gain amplifier. Table 3.2 shows calibration settings and results on a randomly selected day in October 2020. Even though the error signals generated are far from perfect I and Q components, Eq. 3.9 keeps the circuit working robustly.

3.4.4 Feedforward

With the new scheme to generate an error signal with arbitrary phase offset, we now consider how to implement a rapid change in lattice phase in the experiment. One approach is to

Lattice	B2 setpoint	V_{VGA}(V)	Beam pair	A_1(V)	A_2(V)	β/π
SW	1.7V	1.02	1-2	0.36	0.75	0.48
			2-3	0.58	0.71	0.50
LW	2.18V	0.42	1-2	0.45	0.29	0.38
			2-3	0.70	1.40	0.56

Table 3.2: Calibration of error signals on a randomly selected day in Oct 2020. The B2 setpoints chosen correspond to lattice depth of 4 kHz for both lattices.

simply vary $S_1(\phi)$ and $S_2(\phi)$ to change the offset and let the feedback system do its job to follow. Such an approach is limited by the bandwidth of the lock, which is set by the loop filter in the system. The loop filter being used at the moment is designed to set a bandwidth of a couple of kHz [47]. However, we would want to change the lattice phases at 10's of kHz in some experiments, for example the moving lattice experiment reported in the next section. This requirement is in conflict with the constraint that the lock becomes unstable at a few 10's of kHz (see section 4.5 of [47]).

We take another approach to achieve rapid changes in lattice phases. This approach is known as the feedforward technique. The idea of the technique is as follows. In addition to changing the offset of the lock point, we also change the frequency of the beam in a complementary way such that the error signal remains where it is throughout the change. To be more specific, recall that the error signal goes as $\sin(\theta + \phi)$. Suppose we change the offset in a dynamic way $\phi \to \phi(t)$. To compensate this change, we can intentionally vary the frequency of a lattice beam as $\Delta f(t)$. This leads to a change in the relative phase between the lattice beams. If the following condition is satisfied

$$\theta(t) = 2\pi \int \Delta f(t) dt = -\phi(t), \tag{3.10}$$

then $\theta(t) + \phi(t)$ remains zero, and the feedback system only needs to correct for fluctuations on top of the dynamic change.

To develop some intuition, consider applying the same technique to a feedback system that stabilizes the intensity of a laser beam. In that case, the two complementary actions would be jumping the set point and jumping the laser power. The error signal will remain unchanged if the two actions precisely match up.

In our experiment, ϕ can be varied dynamically by sending scaling signals $S_1(\phi(t))$ and $S_2(\phi(t))$ to the multiplier circuit, while the frequency of a lattice beam can be changed by sending a signal $V_{\mathrm{ff}}(t)$ to the frequency modulation port of the signal generator which drives the corresponding lattice AOM. Note that the same frequency modulation port is where the

error signal $V_{\rm err}(t)$ is fed to. This modulation port has an input range of $\pm$ 5V. An inverting summing circuit[3] is used to add up the two signals: $V_{\rm FM}(t) = V_{\rm err}(t) + V_{\rm ff}(t)$. The voltage to frequency conversion is determined by $\Delta f(t) = K_{\rm VCO} \times V_{\rm FM}(t)$, where

$$K_{\rm VCO} = \frac{2\pi \times \text{frequency deviation}}{\text{input range}} \tag{3.11}$$

Here, both *frequency deviation* and *input range* are parameters that can be set on the function generator. We set frequency deviation to a value depending on requirements from the experiment. See next section for an example. The input range is usually set to 5V, but can be switched to 1V if a higher gain is needed.

From the above discussion, it is clear that the synchronization of the two complementary actions is crucial, especially when rapid dynamical experiments are to be performed. The signal generators we use are direct digital synthesizers. Internal analog to digital conversion causes a delay, which has to be taken account. This delay is empirically determined to be $\tau = 13\,\mu$s. In practice, the feedforward condition is $\theta(t) = \phi(t + \tau)$.

3.4.5 Demonstrations

In this section, we demonstrate the use of the arbitrary phase lock system through two examples. The first one is a run-to-run change of the superlattice geometry through changing the lock point offset ϕ. The second one is loading atoms into a moving (bichromatic) lattice using the feedforward technique. We focus on the technical details, instead of the physics, of these two demonstrations to illustrate how this new system is used in practice.

Superlattice geometry change The first demonstration shows how the superlattice geometry can be changed by varying the lock point offset ϕ. Here the lock point offset of one pair of LW beams is varied, therefore moving the LW lattice along the direction of a lattice vector. In particular, we pick the beam 2-3 pair and move the lattice along the $\mathbf{a}_3 = \mathbf{a}_1 - \mathbf{a}_2$ direction (Fig. 5.1 (a) and (b)).

We initialize the system by picking $\phi = 0$, such that the two scaling factors are $S_1 = -\tan(\beta)$, $S_2 = (A_1/A_2) \times (1/\cos(\beta)$ (Eq. 3.9). Using the dispersive glass wedges in the set up, we prepare a superlattice in the 1D-stripe geometry as a starting point. At this point, we have not done anything new beyond the function of the original phase lock system.

Now, instead of using the dispersive glass wedge, we vary the offset of the lock point in the phase feedback to change the superlattice geometry. Before each experimental run, we vary the values of $S_1(\phi)$ and $S_2(\phi)$ such that an error signal with a different offset ϕ is generated in the experiment. See Fig. 3.10 (b). Over the whole range, the SW lattice travels a distance of a lattice spacing $a_{\rm LW} = 2/3 \times \lambda_{\rm LW}$. Half way through this range, the LW repulsive site is brought to the location of a SW site, creating a kagome lattice. When the offset reaches 2π, the superlattice should return to the 1D-stripe geometry it started with.

[3]This inverts the error signal and shifts the lock point by a constant π.

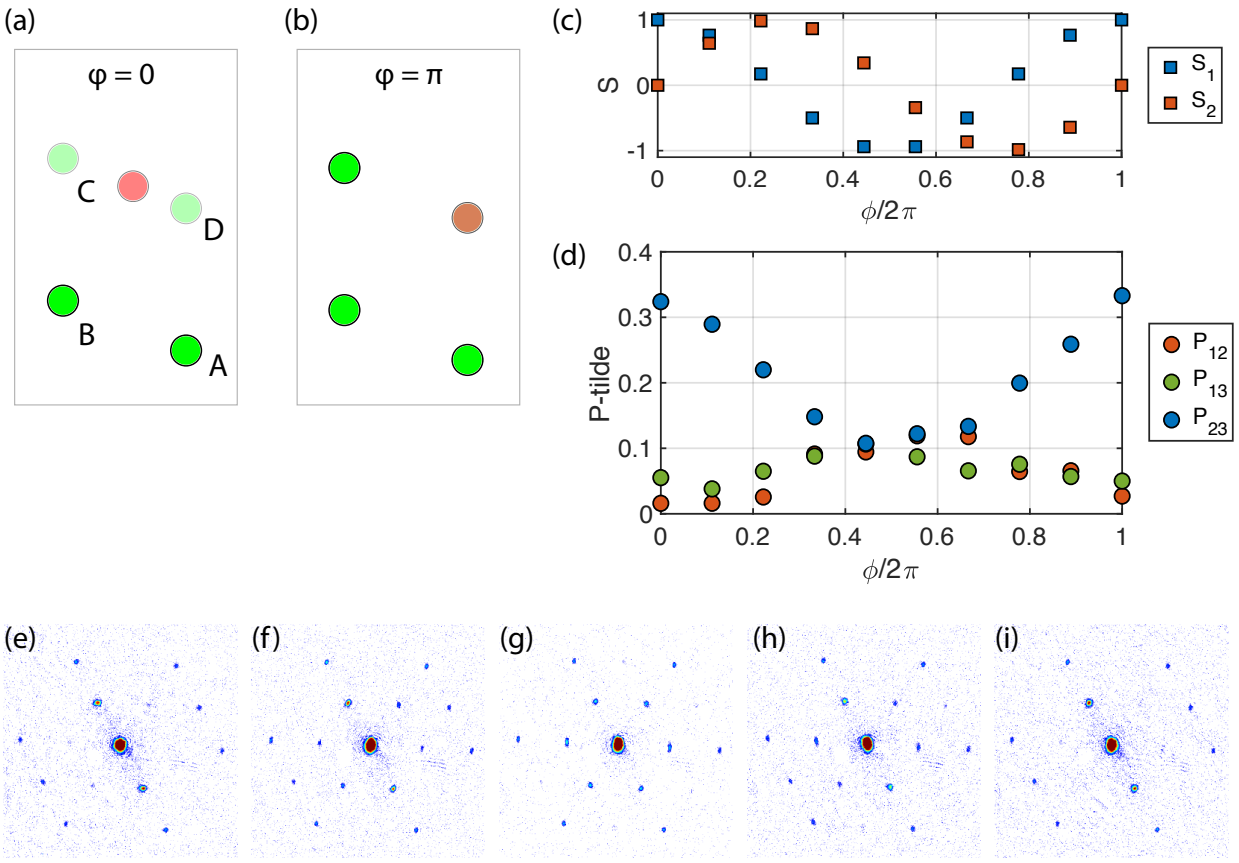

Figure 3.10: Superlattice geometry scan by varying the offset ϕ of the phase feedback lock point. (a) At $\phi = 0$, the repulsive LW lattice site raises the energies of sites C and D, realizing a superlattice with 1D-stripe geometry. (b) At $\phi = \pi$, the superlattice returns to the kagome geometry. (c) Scaling factors S_1 and S_2 for different values of ϕ. (d) Measured $\tilde{P}$ (filled circles) and theoretical predictions (solid lines). (e) - (i) Diffraction images obtained at $\phi/2\pi = 0.00$, 0.22, 0.44, 0.78 and 1.00.

The diffraction images as well as the extracted $\tilde{P}$ quantities show the change from a 1D-stripe to a kagome lattice, and then back to the 1D-stripe. The smooth changes between lattice geometries confirm that the phase lock system works properly to translate the LW lattice in real space which leads to changes in the superlattice geometry.

Moving lattice The second demonstration involves moving lattices. A lattice is said to be moving when the potential as a whole translates in real space over time : $V(\mathbf{r}) \rightarrow V(\mathbf{r}-\mathbf{r}_0(t))$. To move a lattice, one can frequency-detune the lattice laser beams. In our experiment, we achieve the same effect by sweeping the relative phases between the laser beams. Phases of both pairs of beams (beam 1-2 and beam 2-3) of each color can be swept to move the lattice

in a 2D plane. The velocity of a moving lattice $\mathbf{v}_{\text{lat}}$ is given by the following expression

$$\mathbf{v}_{\text{latt}} = f_{12}\mathbf{a}_{12} + f_{23}\mathbf{a}_{23} \tag{3.12}$$

where f denotes frequency detuning and $\mathbf{a}$ denotes the lattice vectors.

In our experiment, we turn all the lattice beams on to low lattice depths (sub-recoil) first such that both the intensity and phase locks can be engaged without affecting the atoms. After this preloading stage, the lattice can be accelerated immediately or after the lattice is ramped up to the targeted depth. In the former case, the atoms are still approximately free particles, excepted that they are boosted to a non-zero velocity in the lattice frame. Subsequent ramping up of the lattice can connect atoms to Bloch states in excited bands. In the latter case, the atoms are described by Bloch states of the lattice. Lattice acceleration leads to Bloch oscillation of atoms. A combination of both allows us to explore freely the band structure of a lattice. These ideas are further explained in later chapters. See Chapter 5 for discussions on connection between moving free particles and excited Bloch states, and Chapter 6 for discussions on Bloch states in a moving lattice. In the following demonstration, we load stationary atoms into moving lattices, i.e. accelerating before ramping the lattice.

We first consider how fast of a moving lattice we need. Suppose we want to have atoms moving at $\mathbf{v}_{\text{lat}} = 1.25 \times (\mathbf{q}_K/m)$ in the lattice frame, where $\mathbf{q}_K$ is the quasimomentum at a certain K point of the LW lattice and m is the mass of atoms. Since $\mathbf{q}_K$ is along the direction of a lattice vector, we only need to detune one lattice beam, say beam 2-3. In our experiment, $|\mathbf{q}_K|/m = 4.3\,\text{mm/s}$. By Eq. 3.12, we need to detune the LW lattice beam by f_{23}^{LW} =7.6 kHz and the SW lattice beam by f_{23}^{SW} = 15.1 kHz. We use the feedforward technique to sweep the phases at such frequencies.

These required frequency detunings guide us on how to set up the signal generators. Recall that the frequency modulation port has an input range of ±5V. We typically set an upper limit for V_{ff} to be around 4V to leave some margin for normal feedback purposes. We want to keep the frequency deviation parameter at as small as the experiment allows for two reasons: (1) to use the full range of the frequency modulation port for better signal-to-noise ratios, and (2) to suppress overall gain of the phase lock system as to avoid feeding back extra technical noises onto the lattice beams, and also feedback instability. Therefore, we set the frequency deviation parameter to be $(5/4) \times f_{23}^{\text{LW}}$ kHz = 9.5 kHz/V and $(5/4) \times f_{23}^{\text{SW}}$ kHz = 18.9 kHz/V for the signal generators in the LW and SW setup respectively. One should calibrate this voltage-to-frequency conversion empirically to avoid errors due to small offsets in the circuits. This can be done by checking the frequency of the error signal with a chosen V_{ff}.

Now we are ready to perform the experiment. The experimental sequence is as follows. Again, we initialize S_1 and S_2 according to Eq. 3.9 and V_{ff} to 0. As a BEC is created and the lattice is preloaded, V_{ff} is jumped to 4V. After a delay of $\tau = 13\,\mu$s, S_1 and S_2 are varied according to Eq. 3.9, with $\phi(t) = 2\pi f_{23} t$. Finally, the lattice is ramped up to its full depth V_{SW} = 25kHz and V_{LW} = 15kHz. In Fig. 3.11, we show single-shot diffraction images taken with atoms loaded into the moving SW, LW and kagome lattices, all moving

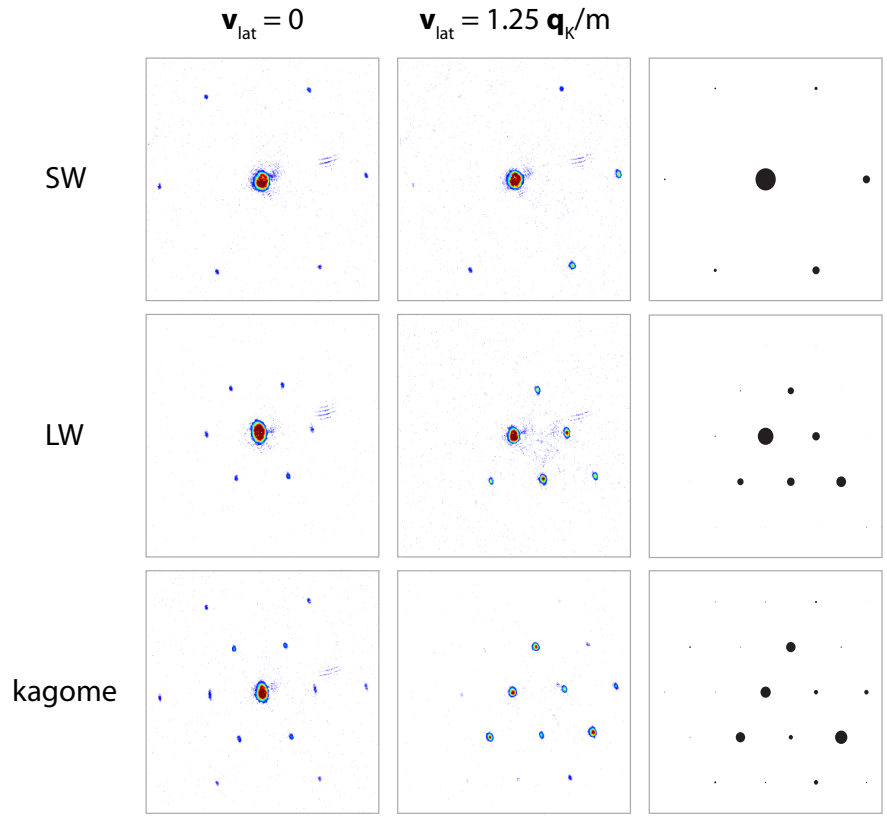

Figure 3.11: Diffraction images of atoms loaded into mono-/bichromatic (left) stationary and (middle) moving lattices. For the velocity chosen ($\mathbf{v}_{\text{lat}} = 1.25\mathbf{q}_K/m$), atoms are loaded into the n=1 band of the SW lattice, and the n=3 band of the LW and kagome lattice. For comparison, momentum distributions calculated from non-interacting band theory are shown on the right.

at $\mathbf{v}_{\text{lat}} = 1.25(\mathbf{q}_K/m)$. The images obtained agree qualitatively with calculations from non-interacting band theory.

It is also possible to implement multi-stage acceleration sequences by concatenation. One has to pay attention to the phases accumulated in each step and make sure S_1 and S_2 are continuous everywhere. The delay in the signal generators is also important to be included every time when a new acceleration section begins.

Example traces of V_{ff} and $S_{1/2}(t)$ for implementing a 2-step lattice acceleration is shown in Fig. 3.12. The sequence is divided into four sections, labeled by numbers 1-4. To keep things generic, we write the voltage-to-frequency conversion factor as α [kHz/V]. In section 1, the first acceleration takes place. V_{ff} is linearly increased to some targeted value. As a result, the scaling factors should vary according to Eq. 3.9 with $\phi(t)$ accumulates as $2\pi f(t)t \sim t^2$. In section 2, V_{ff} is held at a constant value. This corresponds to a lattice moving at a

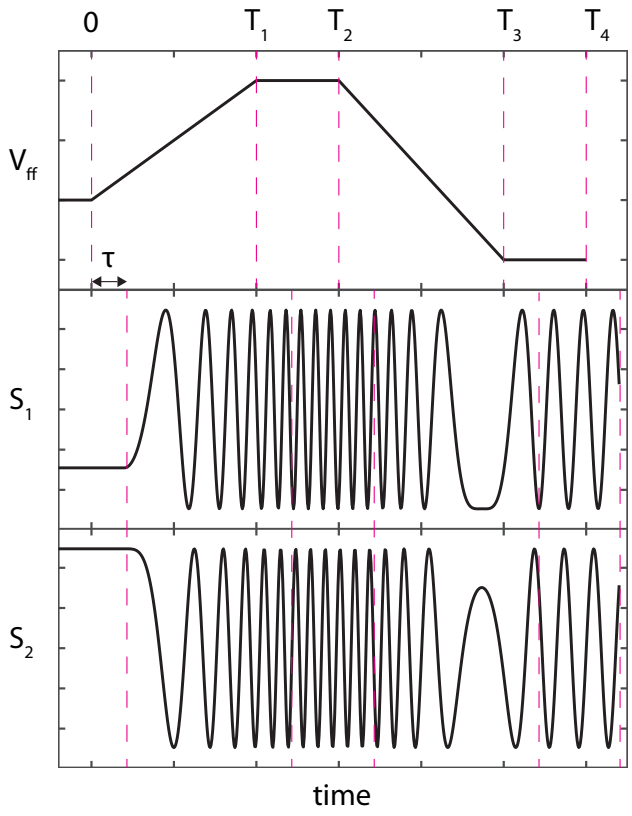

Figure 3.12: Illustration of the implementation of a 2-step acceleration experiment described in the text.

constant velocity. After a delay of τ, S_1 and S_2 are set to vary with linearly increasing phase $= 2\pi(V_{\rm ff}/\alpha)t + \Theta_{acc1}$, where $\Theta_{acc1} = 1/2(V_{\rm ff}/\alpha)T_1^2$ is a constant phase coming from the phase evolution during section 1. Ignoring such a phase leads to a glitch in $S_{1/2}$ that could disengage the phase lock. Sections 3 and 4 are similar to sections 1 and 2, except with additional terms in the phase to include phase evolution from earlier sections. In Chapter 6, we will present results from a 2-step acceleration experiment performed with a honeycomb lattice that explores the singular nature of the Dirac points.

Chapter 4

Breathing of the Trimerized Kagome Lattice

This short chapter concerns our studies on the spatial coherence of strongly interacting bosons in an optical trimerized kagome lattice. Major results of the work are reported in publication [45] and Thomas Barter's dissertation [47]. In the following, we discuss an important aspect of our data analysis method – the consideration of the "lattice breathing" effect – that is not reported in the above references.

4.1 Introduction

The trimerized kagome lattice (TKL) can be regarded as a triangular lattice of trimers (triangular plaquettes), where the intra-trimer tunneling (J) and inter-trimer tunneling (J') are different. The ratio of J'/J (the degree of trimerization) is a knob that tunes the lattice between geometrically frustrated settings at two different scales. In the limit of $J'/J \to 0$, we obtain a collection of independent trimers, which represent an exemplary setting for spin frustration (see Chapter 1). For $J' \sim J$, the trimers are coupled, and the overall lattice supports macroscopic frustrated quantum states like spin liquids, similar to the regular kagome lattice.

From a theoretical point of view, TKL is important in providing a model through which insights into understanding the kagome antiferromagnet can be obtained [60]. It has attracted a lot of theoretical interest, both in the condensed matter [60, 61, 62] and atomic physics communities [63, 64, 65]. In recently years, solid state materials with TKL structure have been synthesized and studied [66, 67]. To the best of our knowledge, our work is the first reported realization of an optical TKL for ultracold atoms.

Summary of the published results

We perform three experiments that demonstrate the features of the optical trimerized kagome lattice. First, we reveal the broken inversion symmetry of this lattice by studying the coherent diffraction of a weakly interacting superfluid after its transient dynamics induced in the lattice. Second, we study the transitioning into the strongly interacting regime. We measure the nearest-neighbor (NN) coherence of the gas as a function of lattice depths by studying the modulation of its momentum-space distribution obtained from time of flight images. We show that there is persistent nearest-neighbor coherence but no long-range coherence in the system. Third, we directly show the effect of the trimerization by performing interferometric measurements. We employ our superlattice to imprint complex phases on the nearest-neighbor coherence and observe asymmetric momentum distributions. This shows the asymmetry between the strong and weak bonds in this lattice.

The analysis method for the data obtained from the second and third experiment described above will be examined in the following. We will refer to the two experiments as the *lattice depth scan* and the *phase imprinting experiment* respectively.

Comparison of two analysis methods

To extract NN coherence of a strongly interacting bosonic gas in TKL, we fit time-of-flight images obtained in experiments to the following function [45]:

$$\frac{n(\mathbf{k})}{N} = |\tilde{W}(\mathbf{k})|^2 \left(1 + \sum_{i<j} [\alpha_{ij} \cos(\mathbf{k}\cdot\mathbf{a}_{ij}) + \beta_{ij} \sin(\mathbf{k}\cdot\mathbf{a}_{ij})]\right) \tag{4.1}$$

where

$$\begin{aligned} \alpha_{ij} &= \frac{2}{\nu}\mathrm{Re}(\langle a_i^\dagger a_j\rangle_J + \langle a_i^\dagger a_j\rangle_{J'}) \\ \beta_{ij} &= \frac{2}{\nu}\mathrm{Im}(\langle a_i^\dagger a_j\rangle_J + \langle a_i^\dagger a_j\rangle_{J'}) \end{aligned} \tag{4.2}$$

Here, $n(\mathbf{k})/N$ is the momentum distribution of atoms normalized by total atom number, $\tilde{W}(\mathbf{k})$ is the Fourier transform of the Wannier function, $\mathbf{a}_{ij}$ is the lattice vector going from site i to site j, ν is the number of atoms per trimer, and $\langle a_i^\dagger a_j\rangle_{J(J')}$ is the correlation function evaluated over a bond between site i and j with tunneling energy $J(J')$. The summation in Eq. 4.1 runs over the three sites in a unit cell: $i, j \in \{A, B, C\}$.

In our original data analysis, we fix the length of the lattice vectors $\mathbf{a}_{ij}$ (referred to as *bond length* for the rest of the chapter) at a value extracted from diffraction images of a superfluid loaded into TKL. The underlying assumption is that the spacing between sites is constant throughout the experiment. Such an analysis method leads to results (shown in Fig. 4.1 (a) and (c)) that have two puzzling features. First, the NN coherence measured

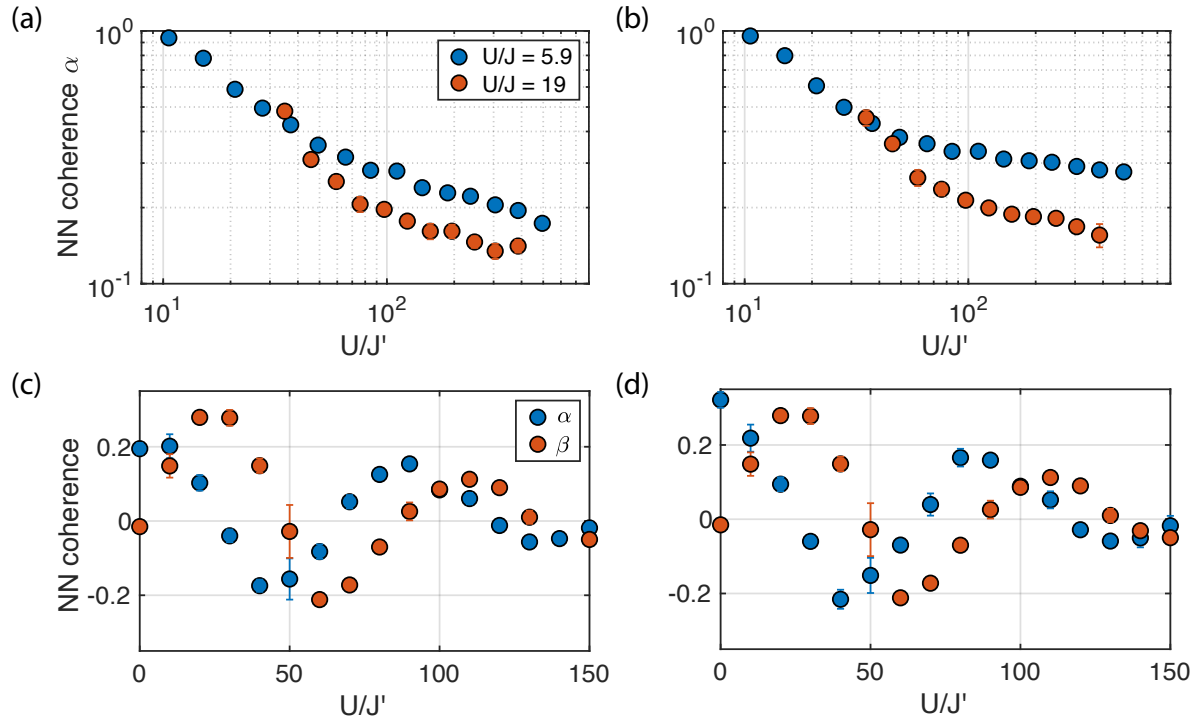

Figure 4.1: A subset of the experimental data obtained from the U/J' scan experiment ((a) and (b)) and the phase imprinting experiment performed at $U/J' = 571$ ((c) and (d)). For data presented in (a) and (c), analysis is performed under the assumption that the bond lengths are constant. For data presented in (b) and (d), bond lengths are treated as fitting variables in analysis.

in the lattice depth scan continues to droop as U/J' is increased. It conflicts with our understanding that at increasing U/J', the total coherence becomes dominated by intra-trimer coherence and reaches a plateau. The droop was first attributed to technical fluctuations which cause heating. Second, in the phase imprinting experiment, because of the complex phase ϕ imprinted, we have

$$\begin{aligned}
\max(\alpha_{ij}) &= \max\left(\frac{2}{\nu}\mathrm{Re}(e^{i\phi}\langle a_i^\dagger a_j\rangle_J + e^{-i\phi}\langle a_i^\dagger a_j\rangle_{J'})\right) \\
&= \frac{2}{\nu}\left(\langle a_i^\dagger a_j\rangle_J + \langle a_i^\dagger a_j\rangle_{J'}\right) \\
\max(\beta_{ij}) &= \max\left(\frac{2}{\nu}\mathrm{Im}(e^{i\phi}\langle a_i^\dagger a_j\rangle_J + e^{-i\phi}\langle a_i^\dagger a_j\rangle_{J'})\right) \\
&= \frac{2}{\nu}\left(\langle a_i^\dagger a_j\rangle_J - \langle a_i^\dagger a_j\rangle_{J'}\right)
\end{aligned} \tag{4.3}$$

Therefore, $\max(\alpha)$ and $\max(\beta)$ represent the sum and difference of the inter- and intra-trimer coherence respectively. We expect $\max(\alpha_{ij}) \geq \max(\beta_{ij})$, with the equality condition holds in the strong U/J' regime. However, with the original analysis method, we obtain an unphysical result of $\max(\alpha_{ij}) < \max(\beta_{ij})$.

It was later realized that the above puzzles are caused by treating the bond lengths as a constant. In fact, the bond lengths are variable in our experiment for two mechanisms. The first one is the so-called "lattice breathing effect", where physical distances between lattice sites change as a function of lattice depths (see next section). The second one is the motion of atoms within individual sites which causes their center of mass to oscillate as a function of time (see section 4.3). This leads to effective bond lengths that are not equal to the physical distances between lattice sites. As we shall see later, in the phase imprinting experiment, the two mechanisms are related in the sense that the sudden change in lattice breathing effect triggers motion of atoms within lattice sites.

The data were reanalyzed with the bond lengths being fit parameters. Both of the above two puzzling features are resolved (Fig. 4.1 (b) and (d)). We call the change in bond length *lattice breathing*.

Lattice breathing

As explained in Chapter 2, the optical kagome lattice is constructed by overlaying an in-plane polarized SW lattice and an out-of-plane polarized LW lattice. The effects of the LW lattice on the overall superlattice potential is discussed in section 2.3. Here, we focus on the "breathing" effect. In the lattice unit cell, the attractive LW lattice site is placed in the middle (centroid) of one of the two trimers. Therefore, the SW lattice sites are situated on potential gradient of the LW lattice attractive site. When the ratio of lattice depths $r_V = V_{\mathrm{LW}}/V_{\mathrm{SW}}$ increases, those SW sites are pulled towards the attractive center. This is easy to understand if one considers that a harmonic potential has a shifted minimum when an extra linear potential is added. The bond lengths (commonly denoted by a_J) between the sites in a trimer therefore decreases with v_r. The breathing of TKL also implies the bond length across two neighboring trimers (commonly denoted by $a_{J'}$) increases with v_r. The dependence of a_J and $a_{J'}$ on r_V is shown in Fig. 4.2 (d).

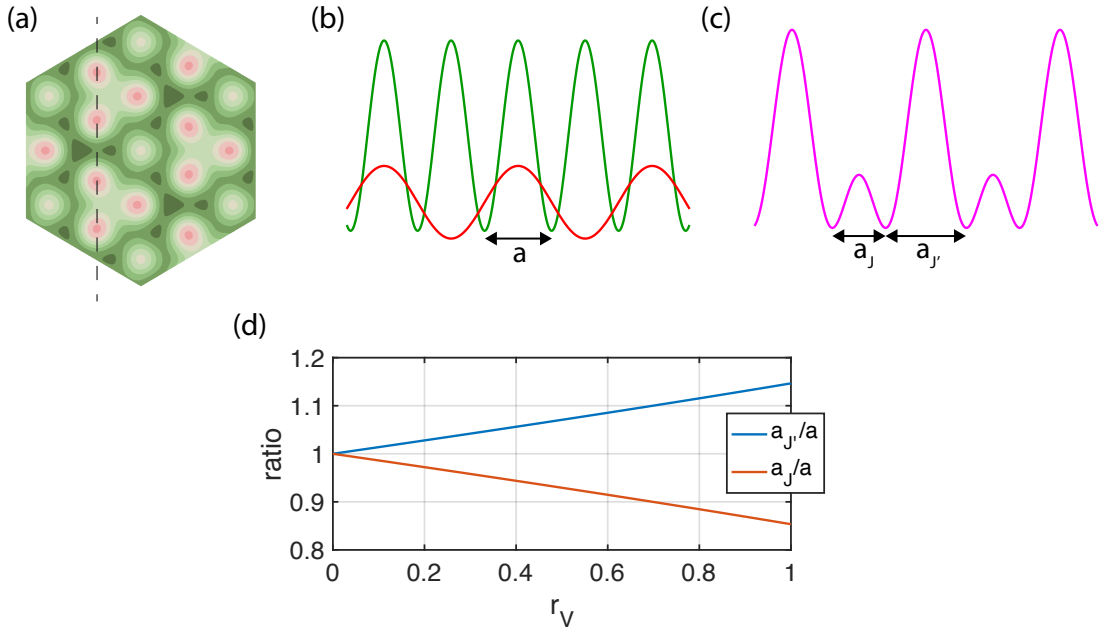

Figure 4.2: Breathing of the TKL. (a) Potential of TKL. (b) Potential of the SW and LW lattice along a one-dimensional cut through indicated by the dashed line in (a). (c) Combined potential along the same cut through. (d) Dependence of a_J and $a_{J'}$ (normalized to the SW lattice spacing a) on r_V.

In theory, for any non-zero value of r_V, there are two different length scales (a_J and $a_{J'}$) in the lattice. In fitting our time-of-flight images to Eq. 4.1, we assume that there is only one length scale. This is a justified approximation. At low lattice depths, the breathing effect is weak and we have $a_J \simeq a_{J'}$. At high lattice depths, the total coherence of the system is dominated by intra-trimer coherence. Therefore modulation of $n(\mathbf{k})$ due to the inter-trimer coherence is negligible.

In the following, we will describe how this breathing effect is observed in our data.

4.2 Lattice depth scan

We discuss the fitting of the lattice depth scan data with both the triangular lattice and TKL in this section.

For the triangular lattice, which is a monochromatic lattice, increasing the lattice depth has no effects on the physical lattice spacing. We expect that the extracted bond length has no dependence on the lattice depth.

For TKL, we expect the bond length to change. In this experiment, U/J' is increased at two constant values of U/J. This involves changing both V_{SW} and V_{LW}. Increasing V_{LW} reduces coupling between different trimers, suppressing J'. However, J is increased at the

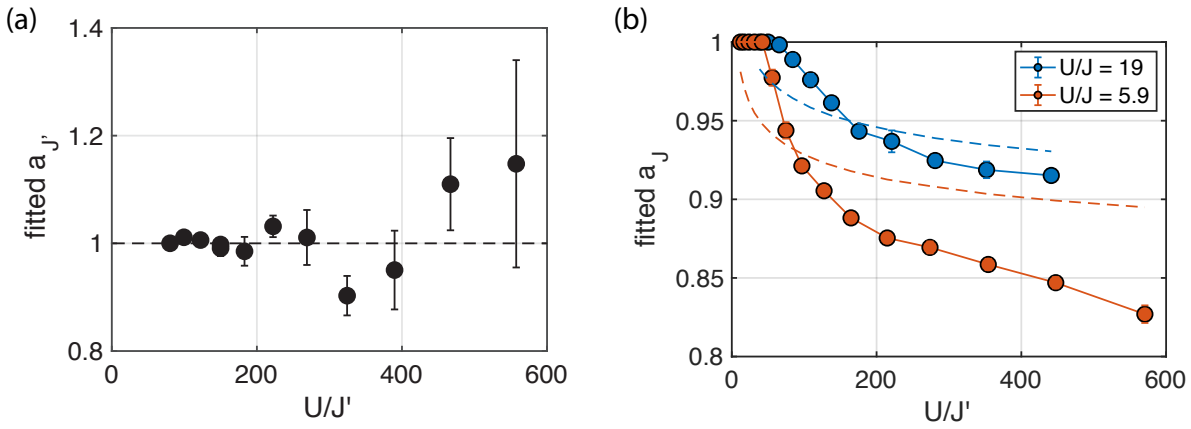

Figure 4.3: Extracted bond lengths as a function of U/J' for the (a) triangular lattice data and (b) TKL data. In (b), the calculated variation of physical lattice spacing with the corresponding change in r_V in the two different experimental settings is shown as dashed lines.

same time, as sites within a trimer are pulled together and the barrier between them are lowered. To maintain the ratio of U/J, V_{SW} is increased (which in turn increases U). It turns out that with increasing U/J', the ratio of r_V increases, and therefore the bond length should decrease.

Since the three sites in a trimer are pulled towards the centroid symmetrically, we assume all three bond lengths to be the same in the fitting.

In Fig. 4.3 (a), we show the extracted bond lengths (denoted by a'_J), normalized by the averaged value of the first five data points, for the triangular data. At relatively low $U/J' < 300$, the fitted lattice spacing shows no trend of variation. As the system is deep into the Mott insulating regime at high U/J', the modulation on the Wannier function $\tilde{W}(\mathbf{k})$ becomes too small to be reliably extracted. The fitted lattice spacing thus varies a lot from shot to shot but shows no overall trend.

The average extracted bond length for the triangular lattice is taken as the lower bound for the lattice spacing fit for TKL. Such a bound is needed for fitting the TKL data taken at low values of U/J', where atoms are still in the superfluid regime and higher-order (beyond nearest-neighbor) coherence terms are significant. Without the bound Eq. 4.1 does not work well and gives unreliable fits. This averaged bond length is also used for normalizing the data presented later.

In Fig. 4.3 (b) we show the fitted bond lengths for the TKL data. In this case, the fitted bond length shows a very clear trend that it decreases with U/J'. Comparing the two data sets, the lattice breaths more at $U/J = 5.9$ than at $U/J' = 19$. This is consistent with the fact that r_V is increased more in the $U/J = 5.9$ data set.

Looking back at Fig. 4.1, we now understand the drooping in extracted α with the original

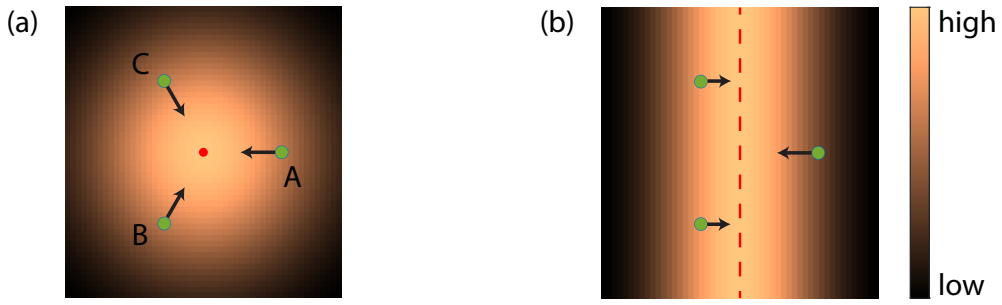

Figure 4.4: Potential and pulling on the trimer sites A, B and C. (a) In the TKL configuration, the attractive center (red dot) is placed at the centroid of the trimer. All trimer sites are pulled equally towards the centroid (black arrows). (b) In the phase-imprinting lattice configuration, the potential gradient points along the direction of the LW one-dimensional lattice. The trimer sites form an isoceles triangular with $a_{AC} = a_{AB} \neq a_{BC}$. The main effect of quenching the lattice is displacing sites B and C vertically in the figure, inducing oscillations of atoms within each site.

fitting method. It is a systematic underestimation of fitted modulation amplitude due to a wrong spatial modulation frequency.

Although the breathing effect is observed, the actual change in the bond length does not agree with our simple calculations with the lattice potential (4.3 (b)). As the effect comes purely from the lattice construction in this case, it seems that the only possible cause of such disagreement is miscalibration of the lattice depths. We will revisit this point at the end of the next section and rule out such possibility.

4.3 Phase imprinting

For the phase imprinting experiment, we turn off one beam of the LW lattice, essentially turning the LW lattice from a triangular lattice to a 1D lattice. This changes the pulling effect of the LW lattice and thus the positions of the lattice sites. In the TKL configuration, the LW attractive site is pulling all the three sites in a trimer equally towards their centroid. In the new lattice configuration, the LW potential gradient points along the 1D lattice direction. The trimer sites form an isoceles triangular, instead of an equilateral triangle as in TKL. This results in two different length scales within a trimer. Hence, we allow two independent bond lengths – one for the bond perpendicular to the lattice direction, the other for the two bonds that have nonzero projections onto the lattice direction. See Fig. 4.4. We do not put any bounds on the bond lengths in this case.

The phase imprinting experiment is performed at three different values of $U/J' = 75$, 215, 571. All the fitting results are shown in Fig. 4.5. We focus on the data taken at $U/J' = 571$, the setting at which we see an unphysical situation of $\max(\beta) > \max(\alpha)$ in

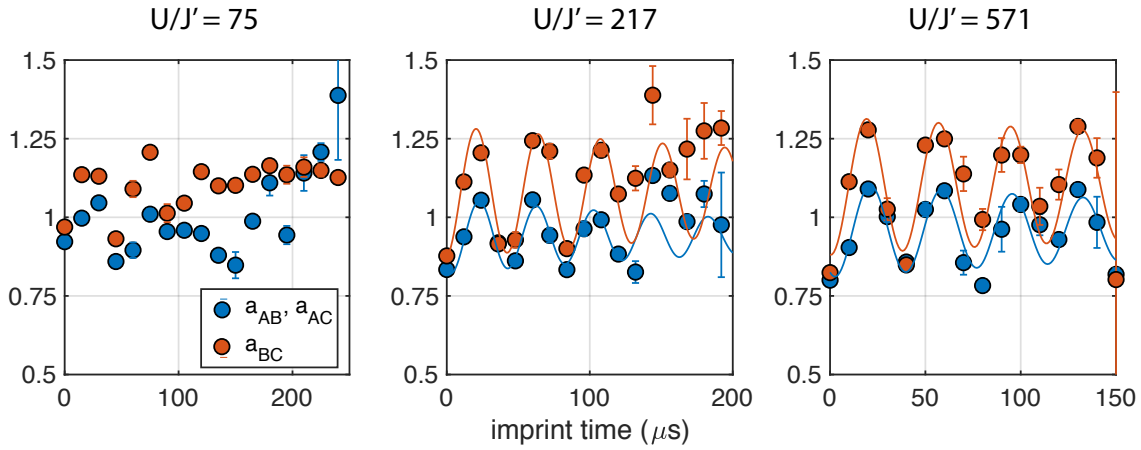

Figure 4.5: Normalized fitted bond lengths for data from the phase imprinting experiment at different values of U/J'. The data at $U/J' = 217$ and 571 are fitted to decayed sinusoids indicated by the solid lines.

the original analysis as described in the beginning of the chapter. At that setting, clear oscillations of the bond lengths are observed. Also, the oscillations begin at the minimum. This can be understood in a classical picture as follows. Initially, the atoms are located at the TKL sites. As the lattice is quenched into a new configuration, the sites are pulled to new positions as explained above. This amounts to putting atoms on a slope of the new lattice sites. Consequently, the atoms begin to oscillate within their sites. Since the pulling effect is stronger in TKL, the oscillations begin with the atoms being the closest to each other. Hence, at $t = 0$, the extracted bond lengths are at minimum.

The oscillations can also be understood through band theory. As the lattice is quenched, the ground state of TKL is projected onto the eigenstates of the new lattice. According to calculations based on non-interacting band theory, around 7% of the population is excited to a p-band, which is associated with the p-orbitals of the lower two lattice sites. This leads to oscillation between the s- and p-orbitals, and the center of mass of the atomic wavefunction oscillates in time.

Similar to what we have seen in the previous section, if the bond length is fixed in the fit function, the extracted NN coherence could be systematically underestimated, unless the actual bond length oscillates to the same value at particular times. At $t = 0$, the bond length is at its minimum, and the underestimation is the most severe. It is also the time when α attains its maximum. Therefore $\max(\alpha)$ is badly underestimated in the original analysis method. In contrast, $\max(\beta)$ is evaluated at roughly $t = 40$ μs (Fig. 4.1). The actual bond lengths happen to be at about the value fixed in the fit function. Hence, there is no underestimation. This explains why $\max(\beta) > \max(\alpha)$ originally. The problem is solved with the new analysis method.

We fit both sets of data obtained at $U/J' = 571$ to a decayed sinusoidal function. Both

fits give an extracted oscillation frequency of 27(2) kHz. This agrees very well with the calculated band gap of 28.1 kHz between the ground s-band and the excited p-band. This band gap is sensitive to the SW lattice depth only, since it is determined by the local trap frequency of the SW sites. Our data thus suggest that we did not miscalibrate the SW lattice. The calibration of the LW lattice is confirmed by the diffraction experiment of this work [45]. Altogether, we have no reasons to believe that the disagreement between the observed and calculated breathing is due to lattice miscalibrations.

Calculations show that at $U/J' = 75$ and 217, the lattice quench excites 3% and 5% of the population up to the p-band, and predicted oscillation frequencies are at 23 and 25 kHz respectively. From the data at $U/J' = 217$, we are still able to see such oscillations at the expected frequency despite less satisfying agreement for data at later times. However, at $U/J' = 75$, we cannot observe any oscillations. This can be due to the fact that in the phase imprinting lattice geometry, neighboring unit cells are no longer isolated from one another. The barriers that separate neighboring trimers do not exist anymore, and atoms are more mobile to tunneling along the direction perpendicular to the LW one-dimensional lattice. This could lead to faster collision-induced decay from the p-band. This tunneling rate is determined by V_{SW} only. Among the three settings of the phase imprinting experiment, V_{SW} is the lowest at $U/J' = 75$, and such tunneling processes should be the fastest.

Chapter 5

Renormalization of the Kagome Flat Band

In Chapter 2, we calculate the non-interacting band structure of the kagome lattice and discuss the importance of the flat $n = 3$ band. An interesting question is how this band structure is modified in the presence of interactions between atoms. We address this question experimentally by probing the band structure of an optical kagome lattice with interacting bosonic atoms. Main results of our experimental work are published in [46]. In this chapter, we provide details of the experimental protocol, data analysis, and numerical modeling that lead to the final data presented in the publication. We also discuss some aspects of the work which are not well understood and could be the subject of future research studies.

5.1 Introduction

Although band theory gives us an excellent starting point to understand systems with discrete translational symmetry like solid crystals, its single-particle nature limits its scope of applicability. To make accurate predictions on the properties of a material, electronic interaction effects have to be taken into account. In some cases, band structure remains good description of the system, but it is modified by interactions. This is referred to as *band renormalization*.

Band renormalization can add peculiar features to the band structrue of a lattice. For bosonic systems, it has been shown in theory that interactions can lead to the so-called looped structure near band crossings of a one-dimensional lattice [68, 69, 70] and several two-dimensional lattices [71, 72].

For the kagome lattice, the band renormalization effect can potentially have very important consequences. In a tight-binding model, the tunneling process between neighboring sites i and j is given by $-J(\hat{a}_i^\dagger \hat{a}_j + \hat{a}_j^\dagger \hat{a}_i)$. A kagome lattice has frustrated tunneling when J is negative. Under that condition, the flat band of the kagome lattice is the ground band, and an important question concerning the many-body ground state of bosons in such a flat

ground band thus arises, given that no quasimomentum is selected as being the lowest in energy. In Ref. [12], this question is addressed by studying the possibility of band renormalization through interactions. At the mean-field level, they find that the flat band of the kagome lattice can be significantly renormalized by interactions such that, with all bosons occupying a specific quasimomentum, the energy can now vary with quasimomentum. A remarkable prediction of that work is that the renormalized flat band has minimum energy at three degenerate points in the Brillouin zone at the Γ, K and K' points (see Fig.). Depending on the temperature of the system, bosons can form a superfluid by condensing at the $K(K')$ points, or a trion superfluid by being in a thermal mixed state occupying all three quasimomenta. While a superfluid has single-particle, long-range order ($\langle \hat{a}_i^\dagger \hat{a}_j \rangle \neq 0$ for largely spaced sites i and j), for a trion superfluid, the long-range coherence is seen only in a three-body operator (a six-field operator). Our experimental findings, taking place in a kagome lattice with positive J, do not relate exactly to the situation in Ref. [12], but they do illustrate the strong role of band structure renormalization in unflattening the single-particle flat-band of the kagome lattice.

A brief review of related experiments

The experimental studies of band structure of optical lattices with bosonic atoms in excited Bloch states began as soon as the loading of BECs into optical lattices were demonstrated in the early 2000's. Early experiments performed with one-dimensional lattices showed remarkable results that confirm predictions from band-theory [38, 73, 74, 57] . In those experiments, atoms are accelerated to excited Bloch states in the lattice frame instead of the laboratory frame. This is achieved by changing the frequency difference between the two laser beams that form the lattice (see section 3.4). In Ref. [38], band gaps between the ground and excited bands at various quasimomenta are measured with coherent oscillations of atoms in a superposition of different energy bands. In Ref. [74, 73], the group velocity and effective mass of atoms, which represent the slope and the curvature of energy bands, are measured with atoms with various non-zero quasimomenta in the ground band. In Ref. [57], atoms are loaded into lattices moving at different speeds, and are placed entirely into excited Bloch bands. The dispersion of excited Bloch bands is measured through the group velocity of atoms. In all these experiments, quantitative agreement with band-theory predictions is obtained.

Interaction effects on band structure have also been studied experimentally. Two kinds of band structure can be distinguished here. (1) The band structure for excitations of an bosonic gas interacting at the mean-field level, commonly referred to as the Bogoliubov bands; and (2) the band structure for a bosonic gas driven out-of-equilibrium into excited Bloch states. The first type of band structure has been probed with Bragg spectroscopy for BECs in a one-dimensional lattice [75, 76] and a three-dimensional cubic lattice [77, 78, 79]. For the second type of band structure, the focus of experimental works has been on searching for evidence of the existence of looped structure. Indirect evidence has been obtained by measurement of modified tunneling probability of a bosonic gas undergoing

acceleration across an avoided crossing of energy bands in a one-dimensional lattice [80, 81, 82], and by measurement of atomic decay rates [83].

Our experimental work belongs to the study of the second type of band structure. It focuses specifically on the effects of mean-field interactions on a flat band. A similar experiment was performed with the optical Lieb lattice [84], which also has a flat band. In that experiment, the interaction-induced distortion of the flat band is revealed by oscillations in sublattice populations with a superposition of band states.

Summary of published results

In our work, we probe the band structure of an optical kagome lattice by measuring the group velocity $\mathbf{v}_g$ of interacting Bose gases in excited Bloch states in the ground and excited bands. To prepare excited Bloch states, we first accelerate a rubidium-87 BEC, essentially preparing a plane wave with non-zero momentum $\mathbf{k}$ [1]. Then, adiabatic ramp-up of the optical kagome lattice connects the plane wave to an excited Bloch state with band index n, which is determined by the momentum imparted initially, and quaismomentum $\mathbf{q} = \mathbf{k}$ modulo reciprocal lattice vectors. To measure $\mathbf{v}_g$, we obtain diffraction images of the atoms and extract the center of mass of these images.

In the experiment, atoms are accelerated along a symmetry line in the direction $\hat{y} = (0, 1)$ (see Fig. 2.2). We measure $\mathbf{v}_g$ of atoms with different initial momenta k_y that are connected to three different bands ($n = 1, 3, 4$). Then we focus on the $n = 3, k_y = 1.25 \times q_K$ Bloch state at various lattice depths ($V_{\mathrm{SW}}, V_{\mathrm{LW}}$) and the number density n_0. We compare our data with calculations based on non-interacting band theory and GPE. The data, in quantitative agreement with the predictions from GPE, show that interactions distort the kagome band structure, in particular the $n = 3$ band. Studies on interaction effects on the real-space atomic density distribution confirms the picture that interactions lead to an effective lattice potential that deviates from the kagome geometry, and thus does not support a flat band.

Tight-binding model

In this section, we try to get some insights into the experimental findings from the tight-binding model. We consider some consequences of including mean-field interactions in this model. The lattice depths chosen for the experiments are not deep enough to be truly in the tight-binding regime, as evidenced by the non-zero group velocity even in the non-interacting band theory. However, tight-binding is still a good model to qualitatively explain the observed band distortion. We focus on the Bloch states probed in the experiment and provide intuitive understanding on (1) why the $n = 3$ band acquires dispersion with interactions, and (2) how the representative $n = 3, k_y = 1.25 q_K$ Bloch state undergoes density redistribution.

We extend the non-interacting tight-binding Hamiltontian in Eq. 2.11 and include the mean-field interaction part as follows.

[1] In this chapter, we denote real and quasi-momentum as $\mathbf{k}$ and $\mathbf{q}$ so that it is consistent with Ref. [46].

$$\begin{aligned} H_{\mathrm{MF}} &= H_{\mathbf{k}} + H_U \\ &= -2J \begin{pmatrix} 0 & \cos(k2) & \cos(k3) \\ \cos(k2) & 0 & \cos(k1) \\ \cos(k3) & \cos(k1) & 0 \end{pmatrix} + nU \begin{pmatrix} |\psi_A|^2 & 0 & 0 \\ 0 & |\psi_B|^2 & 0 \\ 0 & 0 & |\psi_C|^2 \end{pmatrix} \end{aligned} \tag{5.1}$$

where ψ_i ($i \in \{A, B, C\}$) is the wave amplitude in site i of the unit cell, n is the number of atoms in a unit cell and $U = g \int |W(\mathbf{r})|^4 d^2\mathbf{r}$ is the on-site interaction energy.

In general, the Hamiltonian Eq. 5.1 needs to be solved numerically. However, at certain high symmetry points, the eigenstates in the non-interacting case remain eigenstates in the presence of interactions.

Degeneracy lifting

Let's consider a particular pair of neighboring K and M points in the $n = 3$ band. Below we show by simple calculations that these two points are no longer degenerate under interactions.

K point Take $K = (0, 1)q_K$. The non-interacting part of Eq. 5.1 is

$$H_{\mathrm{K}} = J \begin{pmatrix} 0 & -1 & -1 \\ -1 & 0 & 1 \\ -1 & 1 & 0 \end{pmatrix} \tag{5.2}$$

The highest-energy eigenvector is given by

$$\psi_{\mathrm{K}} = \frac{1}{\sqrt{3}} \begin{pmatrix} 1, & -1, & -1 \end{pmatrix}^{\mathrm{T}} \tag{5.3}$$

with eigenenergy $2J$. This eigenstate has uniform density distribution among the three sites in the unit cell. Therefore, it is also an eigenstate of the interaction part of the mean-field Hamiltonian, with eigenenergy $U/3$. This state has a total energy of $E_{\mathrm{K}} = 2J + U/3$.

M point Take $M = (\sqrt{3}/4, 3/4)q_K$. The non-interacting part of Eq. 5.1 is

$$H_{\mathrm{M}} = -2J \begin{pmatrix} 0 & 0 & 1 \\ 0 & 0 & 0 \\ 1 & 0 & 0 \end{pmatrix} \tag{5.4}$$

The highest-energy eigenvector is given by

$$\psi_{\mathrm{M}} = \frac{1}{\sqrt{2}}\begin{pmatrix}1, & 0, & -1\end{pmatrix}^{\mathrm{T}} \tag{5.5}$$

with eigenenergy $2J$. This eigenstate has uniform density distribution among the two occupied sites. Again, it is also an eigenstate of the interaction part of the mean-field Hamiltonian, with eigenenergy $U/2$. Overall, this state has a total energy of $E_{\mathrm{M}} = 2J + U/2$.

We can see that interactions lift the degeneracy in the flat band. The K and M points scale differently with interaction energy U. By simple linear interpolation, we see that the section of the $n = 3$ band between these two points acquires dispersion on the order of $\Delta E/\Delta k = U/(3q_K)$.

Density Redistribution

Generally, non-interacting Bloch states in the $n = 3$ band have different density distributions, and most of them do not remain eigenstates in the presence of interactions. In [46], we perform band-theory and GPE calculations and compare the density distribution of the $n = 3$, $k_y = 1.25$ Bloch state with and without interactions. The result is slightly surprising. Without interactions, most population is equally shared by two of the three sites (B and C), and the third site (A) is only slightly populated. In the presence of interactions, the atoms redistribute so that density becomes even higher in sites B and C, leaving site A further depleted. We can understand this change in density distribution through the tight-binding model.

The eigenstates in the non-interacting case at $(k_x, k_y) = (0, 1.25)$ are

$$\begin{aligned}
\psi_1 &= \begin{pmatrix}0, & -0.71, & 0.71\end{pmatrix}^{\mathrm{T}} \\
\psi_2 &= \begin{pmatrix}0.94, & 0.24, & 0.24\end{pmatrix}^{\mathrm{T}} \\
\psi_3 &= \begin{pmatrix}-0.34, & 0.66, & 0.66\end{pmatrix}^{\mathrm{T}}
\end{aligned} \tag{5.6}$$

For the highest energy state ψ_3, we see that two out of three sites are highly populated as described above. Now we consider the effect of interactions. Interactions create an effective potential for the atoms, where sites B and C are positively detuned by roughly the interaction energy, making an effective unit cell with one low-energy site (A) and two high-energy sites (B and C). Since the $n = 3$ band is the highest energy band in this s-band manifold, the state changes in a way to maximize the energy of the system. This can be achieved by redistributing atoms from site A to site B and C. As a result, the population in site A goes down, and that in sites B and C goes up.

Alternatively, we can consider the coupling between different bands due to interactions. Suppose we start with the non-interacting Bloch state ψ_3 and slightly "turn on" interactions. The change in eigenstates can be calculated by considering the interaction as perturbation. We evaluate the interaction matrix with ψ_3 such that it is given by

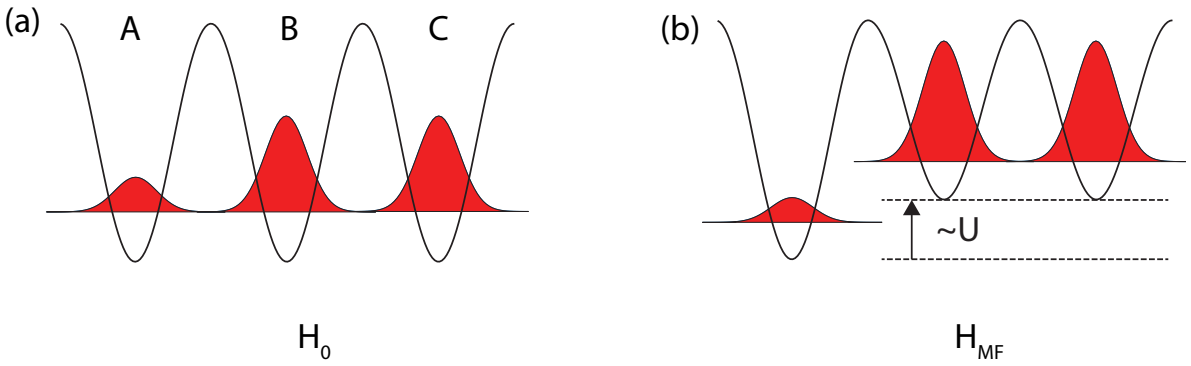

Figure 5.1: Lattice potential modified by mean-field interactions. For the non-interacting eigenstate ψ_3 in Eq. 5.6, one site (A) has much lower population than the two other sites (B and C). In the presence of interactions, the two sites with large populations are effectively detuned by the interaction energy U.

$$H_U = nU \begin{pmatrix} 0.34^2 & 0 & 1 \\ 0 & 0.66^2 & 0 \\ 0 & 0 & 0.66^2 \end{pmatrix}. \tag{5.7}$$

We immediately see that there is no coupling between ψ_1 and ψ_3, i.e. $\langle\psi_1|H_U|\psi_3\rangle = 0$. The coupling between ψ_3 and ψ_2 leads to decreased population in site C, confirming the above argument.

In Chapter 6, we will investigate further into the interacting tight-binding model, in particular what happens to the quadratic band touching point at Γ under interactions.

5.2 Group velocity and Data analysis

In this work, group velocity is the key physical observable that we measure to reveal the interaction-induced distortion of the kagome band structure. A Bloch wave can be regarded as a wave packet, or a superposition of plane waves with a fundamental spatial frequency determined by the lattice spacing. It is natural to define the group velocity $\mathbf{v}_g$ of a Bloch wave as follows,

$$\mathbf{v}_g = \frac{1}{\hbar}\nabla_{\mathbf{q}} E_{\mathrm{n}}(\mathbf{q}) \tag{5.8}$$

where $\mathbf{q}$ is the quasimomentum and n is the band index of the Bloch wave. It can be shown that the group velocity is equal to the averaged velocity of atoms. Such a relation is usually proven in the non-interacting case in introductory solid state physics textbooks. Here, we provide an alternative proof that applies also to interacting cases.

The Hellmann-Feynman theorem reads

$$\frac{dE}{d\lambda} = \langle\psi|\frac{dH}{d\lambda}|\psi\rangle \tag{5.9}$$

where λ is some parameter of the Hamiltonian. For a generic Hamiltonian for a lattice-trapped system with mean-field interactions:

$$H = \frac{\hat{\mathbf{p}}^2}{2m} + V(\mathbf{r}) + g|\psi(\mathbf{r})|^2. \tag{5.10}$$

where $\hat{\mathbf{p}}$ is the momentum operator, $V(\mathbf{r})$ is the lattice potential, $g = 4\pi\hbar^2 a/m$ is the interaction strength, with a being the s-wave scattering length. Applying Eq. 5.9 to Eq. 5.10 and a Bloch state $\psi_{\mathbf{q}}(\mathbf{r}) = \exp(i\mathbf{q}\cdot\mathbf{r})u_{\mathbf{q}}(\mathbf{r})$,

$$\begin{aligned}
\nabla_{\mathbf{q}} E_{\mathrm{n}}(\mathbf{q}) &= \langle\psi_{\mathbf{q}}|\nabla_{\mathbf{q}} H|\psi_{\mathbf{q}}\rangle \\
&= \langle\psi_{\mathbf{q}}|\nabla_{\mathbf{q}}\left(\frac{\mathbf{p}^2}{2m}\right)|\psi_{\mathbf{q}}\rangle \\
&= \frac{\hbar}{m}\langle u_{\mathbf{q}}|(\mathbf{p}+\hbar\mathbf{q})|u_{\mathbf{q}}\rangle \\
&= \frac{\hbar}{m}\langle\psi_{\mathbf{q}}|\mathbf{p}|\psi_{\mathbf{q}}\rangle
\end{aligned} \tag{5.11}$$

Therefore, the group velocity, or equivalently the slope of the band, can be measured through the observable $\langle\psi_{\mathbf{q}}|\mathbf{p}|\psi_{\mathbf{q}}\rangle$. Expressing the Bloch wave in the plane wave basis $\psi_{\mathbf{q}}(\mathbf{r}) = \sqrt{V}^{-1}\sum_{\mathbf{G}} c_{\mathbf{G}}\exp(-i\mathbf{G}\cdot\mathbf{r})$, we have the following relation,

$$\mathbf{v}_g = \frac{\hbar}{m}\sum_{\mathbf{G}}|c_{\mathbf{G}}|^2\mathbf{G} \tag{5.12}$$

In cold-atom experiments, $\mathbf{v}_g$ can be conveniently measured by extracting the center of mass of atomic gases from atomic diffraction images.

Extracting group velocity

This section concerns the details of our data analysis method. Essentially, the analysis extracts the following from raw diffraction images obtained in experiments: (1) the quasi-momentum $\mathbf{q}$ of the Bloch state prepared, (2) number of coherent atoms in each momentum components of the Bloch state and (3) total atom number, including those atoms counted in (2) as well as decayed atoms in the background.

To begin with, two things are needed to interpret these diffraction images. They are (1) the origin, the location that corresponds to zero momentum, and (2) the pixel-to-momentum conversion, which is the distance on the image that corresponds to a particular magnitude of momentum. We take repeated images with a stationary BEC loaded into the lattice.

The averaged position of the central $\mathbf{G}_0$ peak indicate the origin, and the averaged spacing between the diffraction peaks, which represent a well defined distance in momentum space, provides the pixel-to-momentum conversion.

Now we can analyze the images and extract useful physical quantities from them. Throughout the analysis routine, the number of atoms in each momentum peak is extracted by Gaussian fitting. This is empirically the most robust fitting function that works for different images, even the ones with distorted peaks. The flow of the analysis algorithm goes as follows. First, the value of $\mathbf{q}$ is determined every shot by performing a Gaussian fit around a small region centered at an initial guess position. This initial guess position is based on the acceleration time in that particular experimental run. Based on the extracted $\mathbf{q}$, a number of regions of interest (ROI) whose center positions are related by the reciprocal lattice vectors $\{\mathbf{G}\}$ are defined on the image. The size of each ROI is specified such that it is only slightly bigger than the most spread out peak in these images (see Fig. 5.2). We point out that because of repulsive interactions, atoms with the same momentum cannot converge to a single point in real space even with the momentum space focusing technique. From the raw images (see Fig. 5.9), we can see that different peaks have different sizes, with the peaks that have higher populations being more spread out. This spreading has nothing to do with the momentum distribution of the atoms, which is much smaller than what this spreading would suggest.

Gaussian fitting is performed in each ROI to determine the number of atoms of each momentum peak. Because momentum peaks sometimes look distorted and do not have their centers exactly at the expected position based on reciprocal lattice vectors, the analysis routine calculates the position where the density averaged over a small neighborhood is maximum and use it as the initial guess for the Gaussian fit. The initial guess for the $1/e^2$ Gaussian width is just specified as half the size of the ROI. If the fit gives a residual error that is smaller than a threshold value specified by the user, the fitting result is accepted.

To make the algorithm more robust to the variation in peak sizes, a second fit with half the original box size, and half the initial guess for the Gaussian $1/e^2$ width, is performed if the first one fails. This helps with capturing small peaks with an atom number just above the noise floor by providing a better initial guess for fitting, as well as reducing the residual error of the fit so that it is recognized as a good fit by the algorithm. If the second fit also fails, the number of atoms in that peak is taken as zero.

After counting the atom numbers in each peak, we perform data selection. In this experiment, we target at the Bloch states on the symmetry line where $k_x = 0$. Therefore we discard data whose extracted $|k_x|$ is greater than a threshold value. States that are too close to the Brillouin zone boundaries are also discarded due to non-adiabaticity reason (see the lattice loading section). After data selection, the group velocity $\mathbf{v}_g$ can be calculated by Eq. 5.12.

Our experiment concerns Bloch states along a symmetry line in the $\hat{y}$ direction, where the x component of $\mathbf{v}_g$ vanishes by symmetry. By data selection, we only keep data near this symmetry line. Therefore, for simplicity, we use the scalar v_g to represent the y component of $\mathbf{v}_g$.

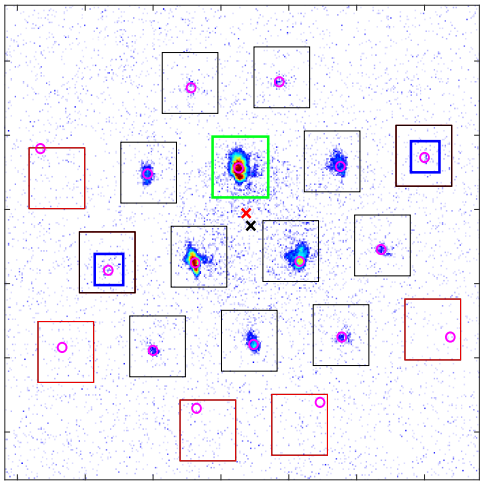

Figure 5.2: Fitting algorithm at work. The position of the $\mathbf{G}_0$ peak is determined (green box), then a number of regions of interest (black boxes) are defined based on reciprocal lattice vectors. In each region, the number of atoms is extracted by fitting the density profile to a Gaussian function. The initial guess for the Gaussian center is determined by finding the position where the density averaged over a small neighborhood is maximum (magenta circles). If the first fit fails, a new region is defined with half the original size (blue boxes) and a second fit is attempted. If the residual error of the second fit is still above the threshold specified by the user, then the fit result is discarded and the atom number in that region is counted as zero (red boxes). The calculated $\mathbf{v}_g$ is marked as a red cross. The origin is marked as a black cross. Note that the diffraction pattern is slightly tilted with respect to the imaging system.

5.3 Lattice loading and adiabaticity

In this section, we explain the details of the lattice loading scheme and how various parameters are chosen. The scheme is separated into two steps, namely lattice preloading and lattice loading. Between these two steps, the BEC is accelerated to some momentum. The acceleration step will be the focus of next section.

Lattice preloading

After the creation of a BEC, the optical lattice is first preloaded such that all the lattice beams are turned on to low intensity levels. This is for providing some optical signal for both the intensity and phase feedback systems to engage.

It is important to keep the preload intensity levels as low as the feedback system allows in practice. A non-zero lattice depth opens up small gaps at Brillouin zone boundaries, which leads to imperfect band transfer when atoms are accelerated across Brillouin zones.

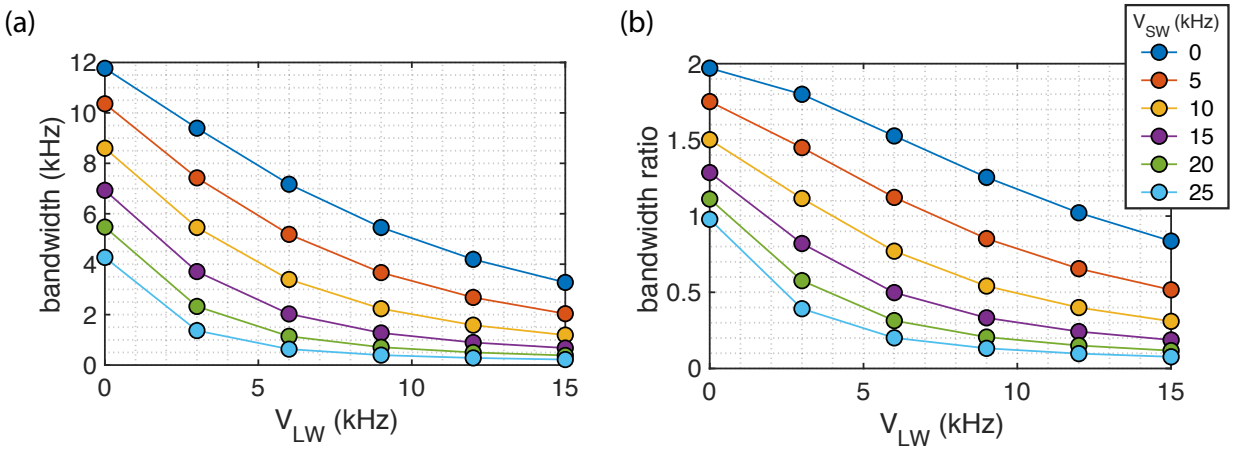

Figure 5.3: (a) Bandwidth of the kagome $n = 3$ band and (b) bandwidth ratio of the $n = 3$ to $n = 1$ bands as a function of lattice depths $(V_{\mathrm{SW}}, V_{\mathrm{LW}})$. Results are calculated with non-interacting band theory.

In practice, we need about 1 mW in each lattice beam. This creates a lattice with $V_{\mathrm{pre}} = 0.5$ (0.4) kHz for the SW (LW) lattice. We estimate the band transfer fidelity to be $\simeq 98$ %, for the $n = 1$ to $n = 3$ band crossing, and almost perfect transfer for the $n = 3$ to $n = 4$ band crossing.

Lattice loading

In this step, the lattices are ramped up from preload depths to their final depths. We first show some results from non-interacting band theory which guide us how to choose lattice depths for this experiment. We look at how the third band is flattened as a function of lattice depths. In figure 5.3, we show the bandwidth of the $n = 3$ band, as well as the bandwidth ratio of the $n = 3$ to $n = 1$ bands, as a function of lattice depths. To have a reasonably flat band, we can choose appropriate values of lattice depths such that the bandwidth ratio $\ll 1$.

Ideally, we want to work with high lattice depths for both lattices so that a tight-binding kagome lattice is constructed (see section 2.4). However, there is a challenge in doing so. In this experiment, excited Bloch states with nonzero $\mathbf{q}$ in the ground and excited bands are explored. Interacting bosonic atoms in excited Bloch states are susceptible to various kinds of instability, including Landau instability, modulation instability [85, 86, 87, 88], as well as inter- and intra-band decay [89, 90, 91]. Such instability is induced by interactions, therefore the time scale for those physical processes to set in is on the order of $1/\mu$, where μ is the chemical potential of the system. With higher lattice depths, lattice sites become tighter, locally increasing the density of the gas and also the chemical potential. This makes interaction-induced instability set in faster, limiting the lifetime of the atoms. We will have a closer look at this issue in section 5.5. As a compromise, we work with lattice

depths of $(V_{\mathrm{SW}}, V_{\mathrm{LW}}) = (25,15)$ and $(20,10)$ kHz in this experiment. At such depths, the bandwidth ratios are 0.1 and 0.2 respectively, and the atoms remain coherent for a few hundred microseconds. This is consistent with estimations based on the chemical potential of the system, which is on the order of 1 kHz.

Now, we need to find a good ramp function and ramp time that respect the adiabatic condition and give us good state preparation fidelity. Ideally, if we can ramp up the lattice in a time that is much longer than the time scale defined by the band gaps, the adiabatic condition can be easily satisfied with standard linear or exponential ramps. For primitive lattices, different bands are separated by lattice recoil energies, typically on the order of 10 kHz. For non-primitive lattices like the kagome lattice, bands associated with each atomic orbital are separated by roughly the tunneling energy, which is on the order of kHz. In particular, for the lattice depths we choose, the separations between the s-bands are roughly 1 kHz. This is very similar to the chemical potential of the system. While the adiabatic condition requires a ramp time that is much longer than $(1\ \mathrm{kHz})^{-1} = 1$ ms, interaction-induced instability forbids such a requirement to be satisfied. As a result, the simple strategy of implementing a slow lattice ramp does not work for us.

To find an efficient ramp function that puts atoms into the excited bands, in particular the $n = 3$ band, we numerically evaluate the fidelity of various ramp functions for a range of Bloch states. The ramp time is fixed at 1.2 ms, which is empirically found to be about the longest ramp time with which a significant fraction of the atoms in the $n = 3$ band is still coherent (more details in the next section). We compare polynomial and exponential ramps with different exponents. Among the ramps considered, the best one we find is an exponential ramp in the following form,

$$V(t) = V_{\mathrm{pre}} + (V_{\mathrm{final}} - V_{\mathrm{pre}}) \times \left(\frac{e^{\alpha t} - 1}{e^{\alpha T} - 1} \right) \tag{5.13}$$

where V_{final} and V_{pre} are the final and preload lattice depths, $\alpha = 2.57$, and T = 1.2 ms. The SW and LW lattices are simultaneously ramped up following the ramp function Eq. 5.13. This optimized ramp $V(t)$ gives the highest fidelity over a wide range of q_y in the section of $n = 3$ band explored in the experiment.

Comparison of state preparation fidelity calculated with band theory between a few different ramps is shown in Fig. 5.4. For the optimal ramp function (Eq. 5.13), the fidelity is above 0.95 over a fairly wide range of q_y. We confirm that the optimized ramp in Eq. 5.13 has similarly high fidelity in the interacting case. We simulate the dynamics of atoms using the time dependent lattice GPE, and compare the final states with the eigenstates of the time-independent GPE at the final lattice depths (see section 5.6) to evaluate the fidelity.

We test the above ramp function by measuring the time variation in v_g of atoms with initial momentum $k_y = 1.25 \times q_K$ that are loaded into the kagome lattice with different lattice ramp times. The results are shown in Fig. 5.5. With the shortest ramp time (0.4 ms), we observe big fluctuations in v_g. As the ramp time is increased, the fluctuations in v_g become smaller, converging to roughly the value predicted by GPE.

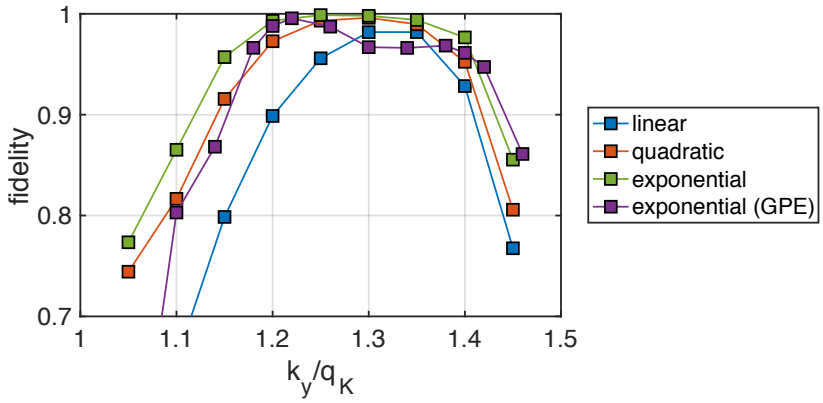

Figure 5.4: Comparison between different ramps. Fidelity shown in the plot is calculated with non-interacting band theory for a linear ramp (blue), a quadratic ramp (orange) and an exponential ramp in the form of Eq. 5.13 (green) with a ramp time of 1.2 ms for a range of k_y values that connect to Bloch states in the $n = 3$ band. Fidelity is also calculated (by graduate students Malte Schwarz and Shao-Wen Chang) for Eq. 5.13 with GPE (purple) using actual experimental values : lattice depths $(V_{\mathrm{SW}}, V_{\mathrm{LW}}) = (25, 15)$ kHz and $n_0 = 5.4 \times 10^{-13}\mathrm{cm}^{-3}$).

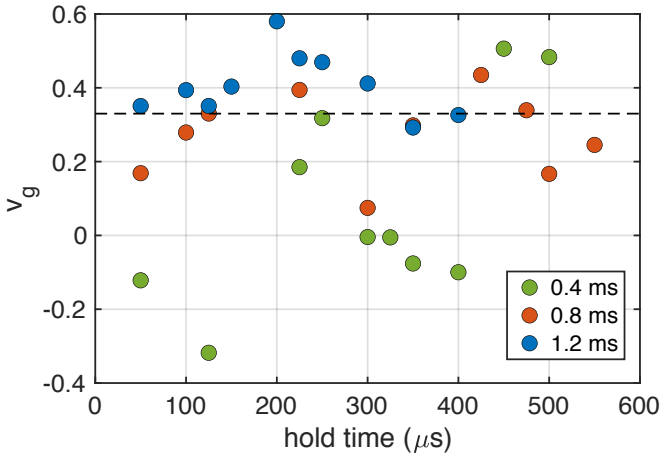

Figure 5.5: Time variation in v_g with different lattice ramp speeds. The kagome lattice is ramped up with the ramp function Eq. 5.13 to $(V_{\mathrm{SW}}, V_{\mathrm{LW}}) = (20, 10)$ kHz in 0.4 ms, 0.8 ms and 1.2 ms respectively. The initial momentum of the atoms is $k_y = 1.25 \times q_K$. The dashed line indicates the value of v_g for the corresponding Bloch state based on GPE.

The observed fluctuations in v_g with the faster ramps are attributed to non-adiabaticity. For a non-interacting system where the principle of superposition holds, ramps with imperfect fidelity put the system in a state of superposition of different bands, resulting in coherent

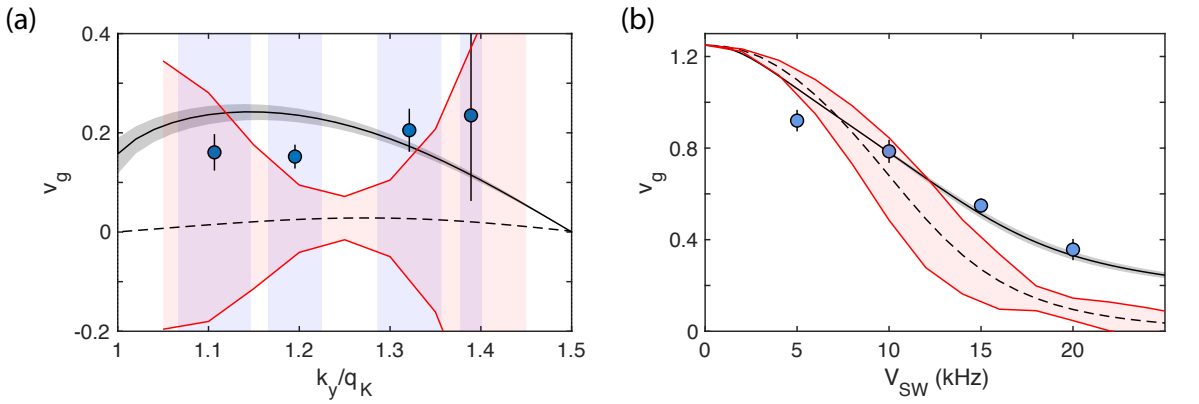

Figure 5.6: Data reproduced from Fig. 2 and 3(a) of [46]. (a) Measurement of v_g of atoms with initial momentum between $1 < k_y/q_K < 1.5$ kHz at fixed lattice depth (25, 15) kHz. (b) Measurement of v_g at various lattice depths with $V_{\mathrm{SW}}/V_{\mathrm{LW}} = 2$ with fixed $k_y = 1.25 \times q_K$. The red shaded region indicates the range of v_g due to imperfect adiabaticity. See publication for detailed experimental conditions.

oscillations in the population of each momentum components, as well as the weighted average $\mathbf{v}_g$. Such oscillations are larger for ramps with lower fidelity. For an interacting system, the principle of superposition does not hold, and the dynamics of a system that is not in an eigenstate can be much more complicated. In any case, we still expect time variation of the state of the system as well as its observables.

We point out that the fidelity values shown in Fig. 5.4 are actually not as high as they may seem. A seemingly small (~ 0.1) population in some other band could potentially lead to substantial oscillations in populations of individual momentum components and also $\mathbf{v}_g$. This is because the amplitude of such oscillations goes as the product of the square root of the fidelity. In the experiment, with 1.2 ms long ramps, we never see oscillations predicted by calculations. Here, we show that even when imperfect ramp fidelity is taken into account, non-interacting band theory is insufficient to explain our data. We show a subset of the data presented in [46], together with the calculated variation of v_g due to imperfect ramp fidelity, in Fig. 5.6. While data taken near Brillouin zone edges and those taken at low lattice depths could be explained by imperfect ramps, data taken at high lattice depths near $k_y = 1.25 \times q_K$ can only be explained if interactions are taken into account.

5.4 Acceleration and number density

After lattice preloading, atoms are accelerated by a red-detuned Gaussian beam that is displaced from the trap center along the y direction. Around half a watt of power is focused into a small beam with $1/e^2$ beam radius of 85 μm. The beam is turned on for 1-2 ms.

depending on the required initial momentum.

This tightly focused beam has an isotropic transverse trap frequency of $\omega_{\rm acc} = 2 \times 80$ Hz. This trap frequency is higher than that of the crossed ODTs (see Table 3.1)). Therefore, in addition to exerting forces for acceleration, this beam also leads to extra confinement to the atoms. When the beam is on, the gas is compressed in a trap that is temporarily tighter. The density of the gas is then increased. After the accelerating beam is turned off and the trap is relaxed, the gas is continues compressing, although at a slower rate. This is because in the experiment the accelerating beam is turned off after a time less than a quarter of the combined trap's oscillatory period. At that instant atoms still have radially inward velocities, therefore compression continues. Lattice beams are immediately ramped up as the accelerating beam is turned off. The atomic motion is then modified by the presence of the lattice.

The density of the gas is an important parameter as it sets the interaction energy scale of the system. This is explicitly shown in GPE (Eq. 5.17). In the following, we model the dynamics of the gas in the above sequence of events and estimate the increase in density at the end.

In our modeling, the crossed ODT $V_{\rm ODT}(\mathbf{r})$ is treated as a single Gaussian beam with beam radii $w_{x/y}$, trap frequencies $\omega_{x/y}$ and trap depth V_0 measured separately[2]. The accelerating beam $V_{\rm acc}(\mathbf{r})$ is also a Gaussian beam as described above. This beam is displaced along $\hat{y}$ by $w_a/\sqrt{2}$ from the crossed ODT center such that the position where its intensity gradient is the greatest coincides with the ODT center.

The potentials and their derivatives are calculated with experimental parameters and plotted in Fig. 5.7. Along the x direction, the trap minima of the crossed ODT and accelerating beam coincide. Therefore the trap frequencies, which is proportional to the second derivative of the potential, simply add up quadratically. The total trap frequency is increased by about a factor of 3. Along the y direction, the two trap minima are displaced from each other. The accelerating beam does not contribute to the trap frequency along y as $\partial_y^2 V_{\rm acc}(\mathbf{r})$ vanishes at the crossed ODT position. In the following, we ignore the effect of third order derivative, which could lead to a skewed density distribution in the gas.

We model the dynamics of the system and calculate the change in the gas density following the formalism presented in [92]. In this paper, a strongly interacting gas in a harmonic trap with time-varying trap frequencies is studied. Throughout the paper, the Thomas-Fermi approximation is adopted. Under this approximation, the peak density of a gas in equilibrium in a harmonic trap is

$$n_0 = \frac{15^{2/5}}{2} \left(\frac{aN}{\bar{a}_{\rm ho}} \right)^{2/5} (\omega_x \omega_y \omega_z)^{1/3} \tag{5.14}$$

[2]We measure the trap frequencies of the ODTs as follows. We create a BEC in the ODTs, then apply a magnetic field gradient in the $x-y$ plane to displace the atoms from the center. Measuring the BEC's position/velocity in its subsequent oscillatory motion, the in-plane trap frequencies ω_x and ω_y of the ODTs can be extracted. The trap depth can then be inferred from the trap frequencies and measured beam radii w along either x or y according to $V_0 = (1/4)m\omega^2 w^2$.

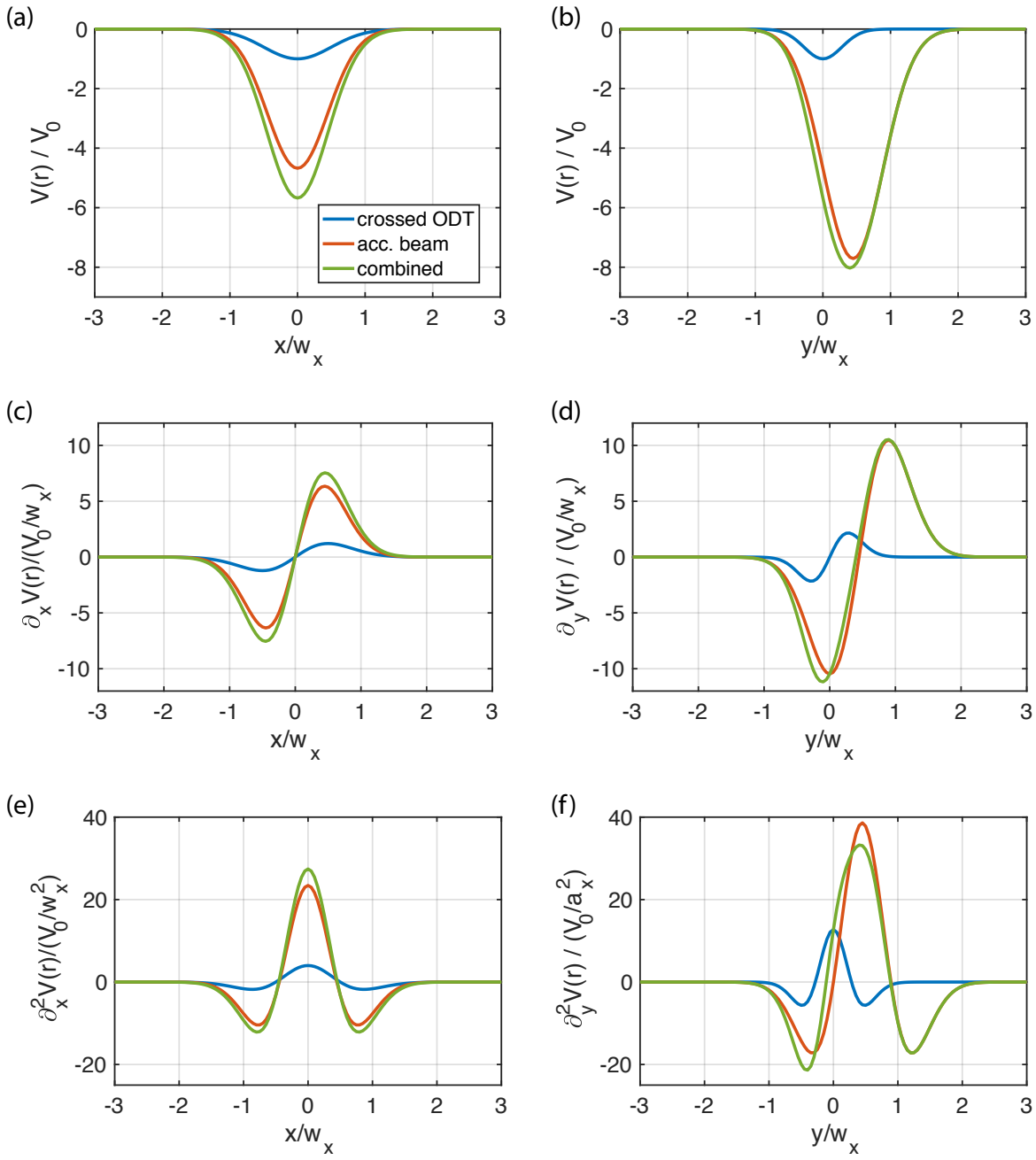

Figure 5.7: Potentials of the crossed ODT and accelerating beam and their derivatives along x and y. All quantities are calculated using experimental parameters. Units are derived from the depth of the crossed ODT V_0 and its harmonic oscillator length w_x along x.

where a is the s-wave scattering length, N is the number of atoms, $\bar{a}_{\mathrm{ho}}$ is the averaged harmonic oscillator length of the trap. If the trap frequency $\omega(t)$ is time dependent, the

Thomas-Fermi radii rescale $R_j \to \lambda_j(t)R_j$ according to a set of coupled second-order, differential equations of motion. By scaling analysis, the peak density of the gas then scales as $(\lambda_x(t)\lambda_y(t)\lambda_z(t))^{-1}$.

We extend their formalism to allow time dependence of the atomic mass. This is to account for the effects of the optical lattice on the atomsic motions through time-dependent effective mass terms. We obtain the following set of equations,

$$\ddot{\lambda}_j = \frac{m(0)}{m(t)}\frac{\omega_j^2(0)}{\lambda_j\lambda_x\lambda_y\lambda_z} - \lambda_j^2(t)\lambda_j - \frac{\dot{m}(t)}{m(t)}\dot{\lambda}_j \tag{5.15}$$

for j = {x, y, z}.

The effect of the accelerating beam on the overall trap frequency in the x direction is modeled by a step function:

$$\omega_x(t) = \begin{cases} \omega_x(0) & t < 0 \text{ and } T_{\text{off}} < t \\ \alpha\omega_x(0) & 0 < t < T_{\text{off}} \end{cases} \tag{5.16}$$

Here $\omega_x(0) = 2\pi \times 23$ Hz, $\alpha \simeq 3$ and $T_{\text{off}} \simeq 1$ ms is the acceleration time (i.e. how long the accelerating beam is turned on). The value of T_{off} changes from shot to shot (for different initial momentum k_y) and here a typical value is chosen for calculations. In our model, along y there is only a boost in velocity and the trap remains unchanged. Furthermore, we estimate the change in the atoms' effective mass using non-interacting band theory. The explicit ramp function of the lattice, which will be explained in details in the next section, is implicitly included in $m(t)$. We only take into account the renormalization of mass in the x-direction, which is posteriori justified by the calculation results that the time scale concerned in the problem is too fast for cross-dimensional dynamics to take place.

The time evolution of λ's, as well as the scaling of peak density $(R_xR_yR_z)^{-1}$, is shown in Fig. 5.8. From the calculation, the density is expected to increase by 5% at the moment the accelerating beam is turned off, and about 20% when the lattice is fully ramped up. We estimate that the density of the gas in the lattice is increased by $\simeq 15 \pm 10\%$ from the original value in the ODTs.

5.5 Holding and decay

When atoms are held in the excited bands, decay occurs. In this section, we take a closer look at this decay process at a few different experimental settings. A few observations are made, based on which the experimental data presented in [46] are selected.

First we look at some raw data obtained in the experiment reported in Fig. 3(a) of [46]. These data are taken in an experiment where atoms with initial momentum $k_y = 1.25q_K$ are loaded into lattices according to Eq. 5.13 to lattice depths $V_{\text{SW}}, V_{\text{LW}}$ = (5,2.5), (10, 5), (15, 7.5) and (20, 10) kHz in 1.2 ms. The atoms are then held in the lattice for a variable amount of hold time, before momentum space focused images are taken.

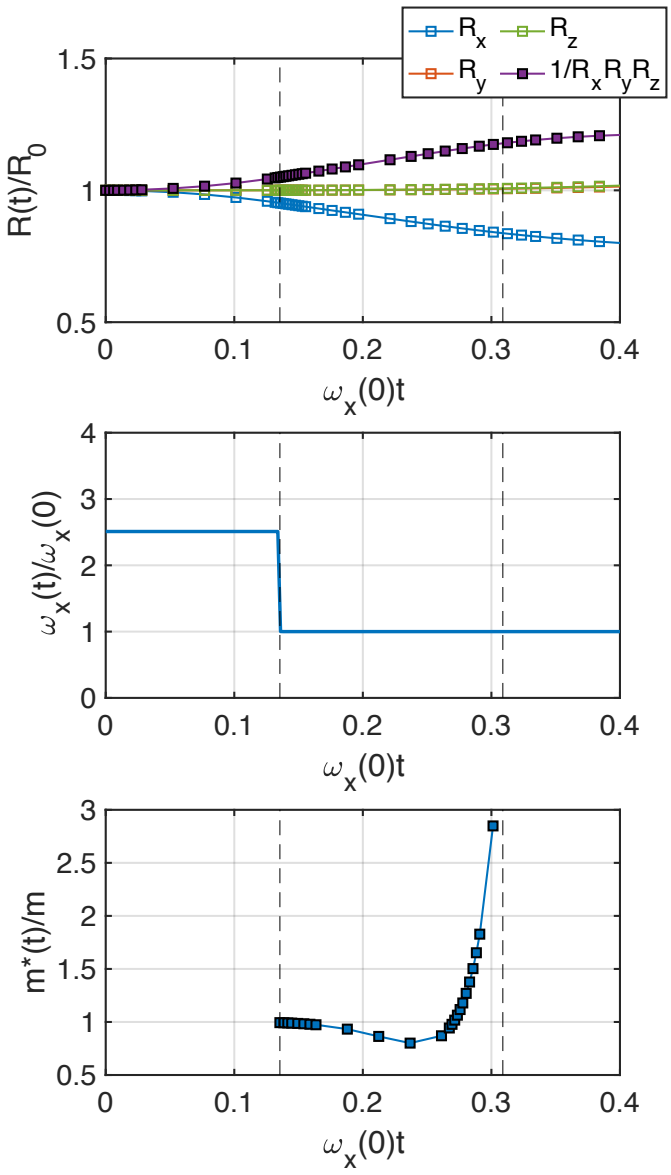

Figure 5.8: Results from solving the coupled equations of motion in Eq. 5.15 with experimental parameters. In the three plots, we show time variation of (a) $R_{x/y/z}$ and the scaling of peak density $1/(R_xR_yR_z)$, (b) trap frequency $\omega_x(t)$, and (c) effective mass tensor component $\partial_{k_x}^2 E$ of atoms, calculated from non-interacting band theory.

A set of representative raw images are shown in Fig. 5.9, We see that the diffraction pattern becomes more and more fuzzy with increasing hold time. More atoms show up as a diffused background and less in the coherent peaks. This decay is more obvious when the lattice is deeper.

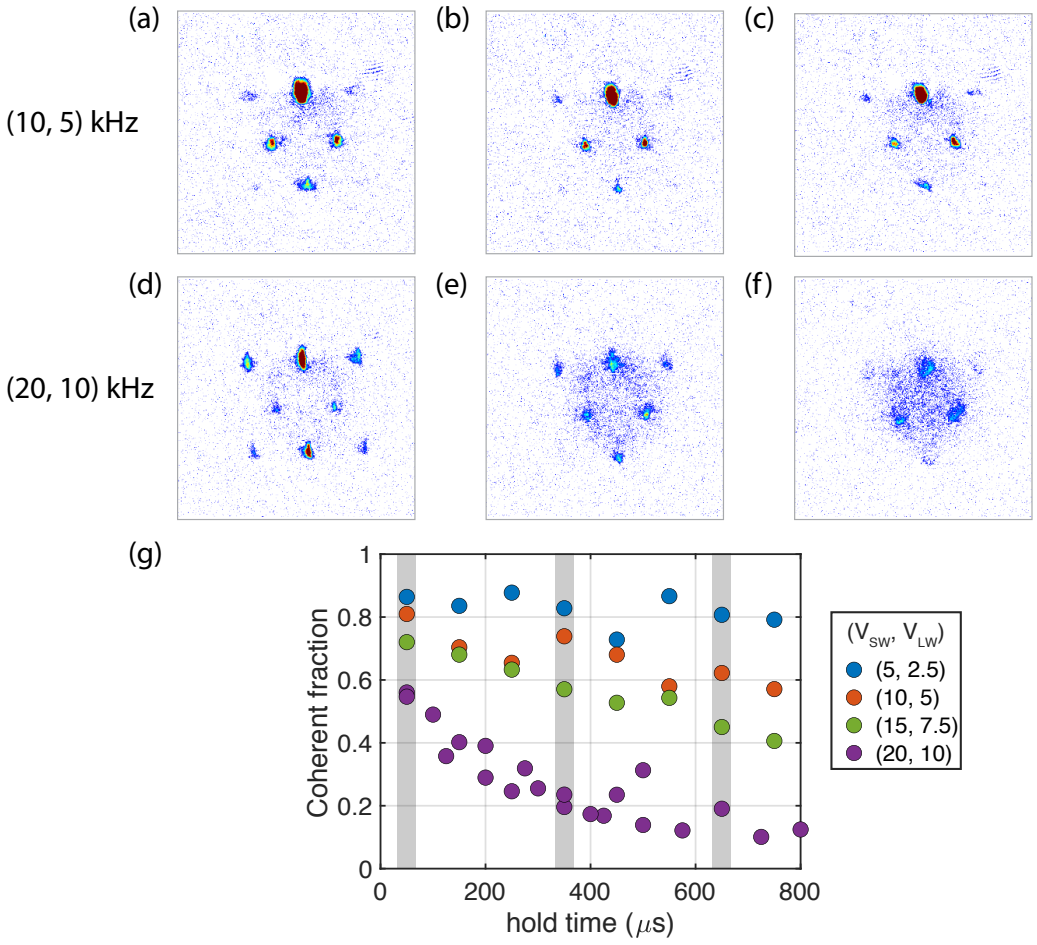

Figure 5.9: Atom decay at different lattice depths. Images shown are taken at hold times 50, 350 and 650 μs, at lattice depths (10, 5) kHz ((a)-(c)) and (20, 10) kHz ((d)-(f)) respectively. (g) Extracted coherent fraction as a function of time at different lattice depths.

We quantify this decay by the fraction of coherent atoms from these images. The fraction is calculated by dividing the sum of the number of atoms in each momentum peak extracted by Gaussian fitting (see the data analysis section) by the total number of atoms extracted by simple box counting with background subtraction. The result is plotted in Fig. 5.9 (g). The decay of coherent fraction is seen clearly from the plot. At (20, 10) kHz, where the $n = 3$ band becomes non-dispersive compared to other bands (see Fig. 5.3), atoms remain coherent only over a few hundred microseconds.

One practical consequence of the decay is that it leads to a background of diffused atoms which makes extracting the number of coherent atoms difficult. The background atoms have a non-trivial density profile which is not straightforward to model. When the density in the background becomes comparable to that in the coherent peaks, the Gaussian fit suffers

from systematic errors and gives biased fitted q_y and thus v_g. Specifically, the fitted center is biased towards the side with more background atoms. For our data, it implies a systematical shift of extracted v_g towards smaller values.

To get around this problem, we post-select data based on the extracted q_y. We only keep data with an extracted q_y that falls within a small range of $\pm 0.05 q_K$ around the nominal value determined by the acceleration time. This range is similar to the range of shot-to-shot random fluctuations of the BEC's momentum.

In Fig. 5.10 , we show the actual total and coherent atom numbers, as well as v_g of atoms for data post-selected as described above. Although the number of coherent atoms still shows the decaying trend (compared to the constant total atom number), the measured value of v_g is constant. It suggests that v_g is preserved under atom decay. This should not be surprising, as the momentum of the whole system is conserved. All the data in Fig. 5.10 are included in averaging and used to make Figure 3(a) of [46]. For other data sets reported in the paper, a hold time of 50 μs is used.

In the process of conducting the experiment and collecting several data sets, we were initially misled by this decay of the group velocity with hold time. We had been working initially with linear, rather than exponential, temporal ramps of the lattice intensity. Comparing the two ramp trajectories, the linear ramp brings atoms into a high-depth lattice for a longer period of time before the end of the ramp and the start of our analysis. Therefore, even atoms that are released from the lattice right at the end of the linear ramp had already decayed a substantial amount, leading to an apparent group velocity that is biased heavily toward zero. In later iterations of the experiment, where we used an exponential temporal ramp, we were able to study the Bloch state with much less decay, and were thus able to measure what is the correct value of the group velocity.

Another interesting aspect of the decay process is its dependence on which band the atoms are loaded into. Below we present some data obtained in the early phase of the project. Atoms are loaded into the kagome lattice with initial momenta $(k_x, k_y) = (1.3, 0), (0, 1.25)$ and $(0, 1.75)$, corresponding to the n = 2, 3 and 4 bands. The lattice is ramped up with a linear ramp function to (25, 15) kHz.

The coherent fraction as a function of lattice hold time is plotted in Fig. 5.11. The visibility has very different coherence times in the three different bands, with the shortest in the $n = 3$ band and the longest in the $n = 4$ band. We attribute the relatively long lifetime in the $n = 4$ band to spatial mismatch between the spatial wavefunction in that band [93], which is predominantly associated with the excluded D site of the lattice, and the lower bands, which is associated with the hybridization of s-orbitals in the A, B and C sites.

In the future, it would be interesting to look more closely at the decayed atoms. Band mapping technique can distinguish between inter- and intra-band decays.

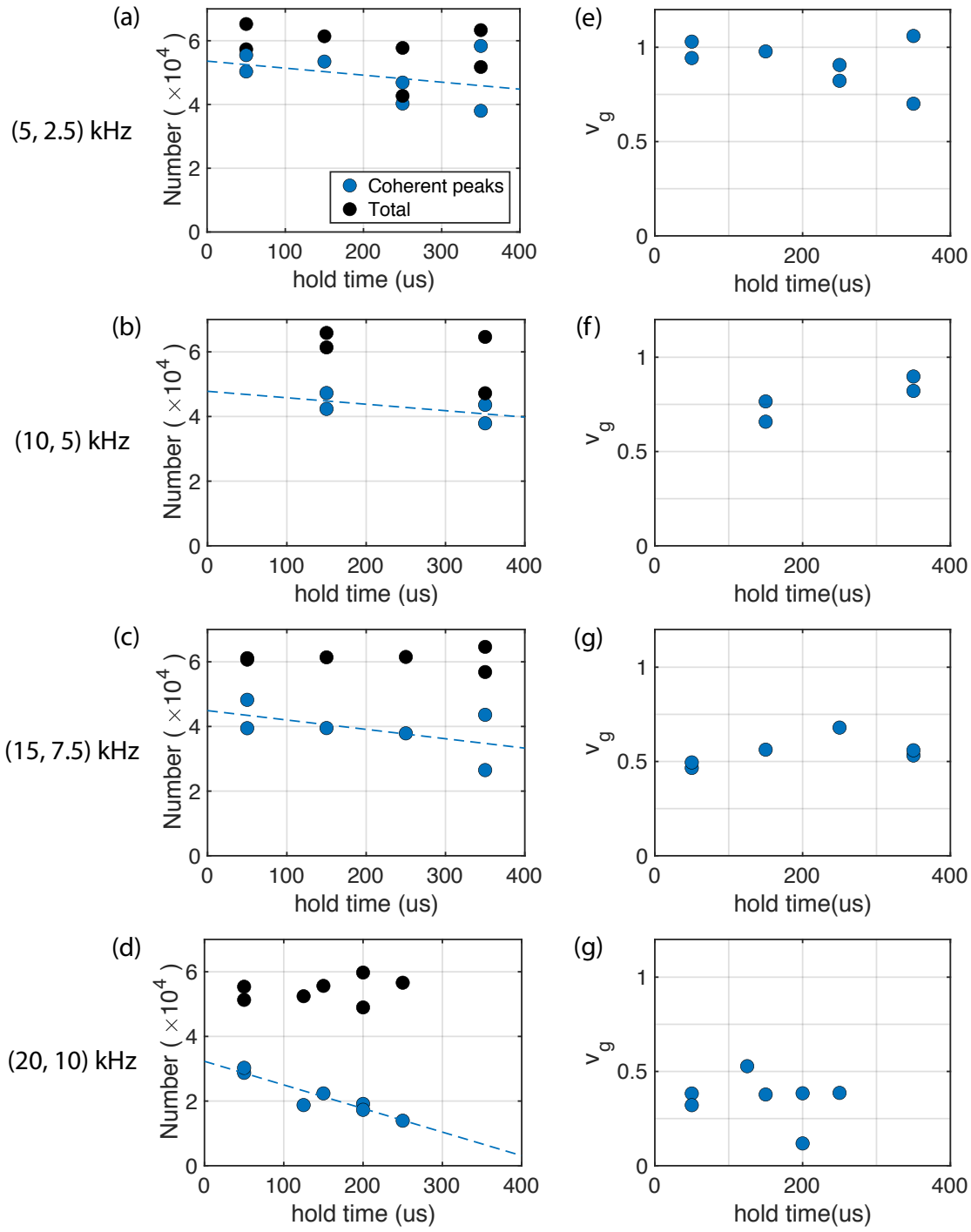

Figure 5.10: Total atom number, coherent atom number and v_g as a function of time at different lattice depths.

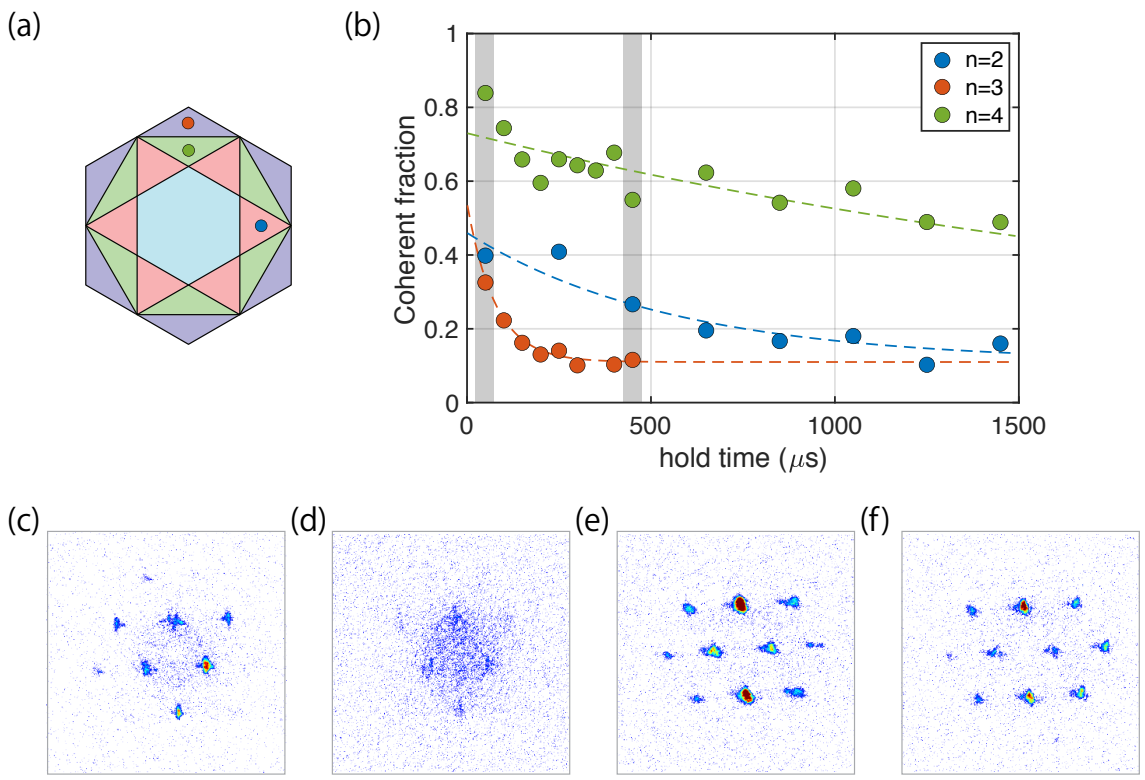

Figure 5.11: (a) A picture of the kagome Brillouin zone. The three dots indicate where in the k-space data shown in (b) are taken. (b) Decay of coherence in different bands. Exponential fits to the data give a $1/e$ lifetime of 560, 80, and 2500 μs for the $n = 2, 3$ and 4 bands respectively. Images taken at hold time = 50 μs and 450 μs in the $n = 3(4)$ are shown in (c) and (d) ((e) and (f)).

5.6 GPE simulations

Gross-Pitaevskii equation

To investigate the effects of mean-field interactions on the kagome band structure, we simulate the system probed in our experiments with the time-independent Gross-Pitaevskii equation. The equation reads

$$\left(\frac{-\nabla^2}{2m} + V(\mathbf{r}) + g|\Psi(\mathbf{r})|^2\right)\Psi(\mathbf{r}) = \mu\Psi(\mathbf{r}) \tag{5.17}$$

where symbols are defined in the same way as in Eq. 5.10. The normalization condition or the wavefunction is given by

$$\int |\Psi(\mathbf{r})|^2 d^2\mathbf{r} = N. \tag{5.18}$$

When dynamics of the system is concerned, Eq. 5.17 can be generalized to time-dependent GPE with the right hand side of the equation replaced by $i\hbar\partial_t\Psi(t)$. Such an equation is used to evaluate the fidelity of our lattice ramp in Section 5.3.

To solve Eq. 5.17, we assume that the solutions take the form of Bloch states. This is a self-consistent assumption, as a Bloch state has the same spatial periodicity of the lattice so the total effective potential supports solutions of Bloch states. Under this assumption, the solution can be expressed in the plane wave basis $\{\mathbf{G}_s\}$ as in the non-interacting case (Eq. 2.24 and 2.26). The interaction term is given by,

$$|\Psi(\mathbf{r})|^2 = \frac{N}{V}\sum_{\sigma,\sigma'} c^*_{\sigma'}c_\sigma \exp(-i(\mathbf{G}_\sigma - \mathbf{G}_{\sigma'})\cdot\mathbf{r}) \tag{5.19}$$

and the matrix element of the mean-field interaction term is

$$\langle \mathbf{G}_{s'}|g|\Psi(\mathbf{r})|^2|\mathbf{G}_s\rangle = \frac{gN}{V}\sum_{s,s',\sigma,\sigma'} c^*_{s'}c_s c^*_{\sigma'}c_\sigma \tag{5.20}$$

for $\mathbf{G}_{s'} - \mathbf{G}_s + \mathbf{G}_{\sigma'} - \mathbf{G}_\sigma = \mathbf{0}$. The state dependence of this interaction term comes in explicitly through the coefficients c_σ and $c^*_{\sigma'}$. For example, when the lattice is weak, the wavefunction is still approximately a plane wave and only $\mathbf{G}_0$ is strongly occupied. In that case the interaction term does not significantly couple different momentum states. As the lattice becomes deeper, the wavefunction is strongly modulated by the lattice potential. More momentum states are populated. As a result the interaction term serves as an effective lattice for the atoms themselves and couples different momentum states.

There are a couple of experimental parameters that need to be determined. The lattice depths ($V_{\mathrm{SW}}, V_{\mathrm{LW}}$) are determined by modulation spectroscopy [50, 47]. The average density N/V is determined based on results from the previous sections. We first extract from our analysis routine the total atom number (not just coherent number). From Eq. 5.14, we calculate the peak density in the crossed ODT. Based on the modeling detailed in section 5.4, we estimate the average density of the gas when the lattice is fully ramped up to be the peak density in the crossed ODT increased by 15%.

To numerically solve for the self-consistent solution of Eq. 5.17, we work in a truncated basis with $-4 \le s_1, s_2 \le 4$. We write Eq. 5.17 as $(2\times 4+1)^2 = 81$ nonlinear equations. This system of nonlinear equations, together with the normalization condition Eq. 5.18, is solved using the *root* function in the scipy.optimize Python package. The function takes an initial guess from the user and tries to find a solution in the nearby parameter space. Our strategy is the following:

1. Pick a value of $\mathbf{q}$ where the state concerned is well separated from other bands as to avoid convergence to unwanted solutions.

2. Use the eigenstate in the non-interacting case as an initial guess and solve for the interacting eigenstate.

3. Use the interacting eigenstate obtained as an initial guess, vary $\mathbf{q}$ or E to find solutions nearby in k-space.

4. Repeat the above step to explore trajectories in k-space.

The code for this root finding routine is developed by another graduate student Shao-Wen Chang.

The above procedure is sometimes complicated by the fact that the nonlinear interaction term allows the emergence of extra solutions (in which case the number of solutions can be larger than the dimension of the Hilbert space) and looped structure near band touching points. At strong interactions, the distortion of the band structure can be so significant that it leads to crossings and hybridization between bands. This effect is particularly important for non-primitive lattices, where the spacing between bands within each orbital manifold is much smaller than recoil energies. Such physics will be further discussed in Chapter 6 with the tight-binding model. In this work, we focus on the solutions that smoothly connect to the non-interacting eigenstates.

With the numerically calculated self-consistent solutions, we can calculate v_g by Eq. 5.12, as well as the real space wavefunction by Eq. 2.24 and 2.26.

Momentum distribution

In our publication, we compare the measured v_g under different conditions with values calculated with GPE to confirm the interaction effects on the band structure. In fact, we can also directly compare the calculated momentum distribution of atoms with the data. The agreement between the two is, however, not as good, as described below.

We consider the $n = 3, k_y = 1.25 \times q_K$ Bloch state at the two lattice depths explored in this experiment: $(V_{\mathrm{SW}}, V_{\mathrm{LW}}) = (25, 15)$ and $(20, 10)$ kHz [3]. We compare the momentum distribution of atoms (2) calculated from non-interacting band theory, (2) calculated from GPE and (3) measured in the experiments reported in [46]. We focus specifically on the eight most populated momentum peaks that together make up $> 95\%$ of the total population (see Fig. 5.12 (a)).

From Fig. 5.12 (b) and (c), we see how the momentum distribution of atoms is changed by interactions. Comparing the predictions by band theory and GPE, there is a significant increase in the population of the $\mathbf{G}_0$ peak. In both cases, the GPE momentum distribution can essentially be reproduced scaling the $\mathbf{G}_0$ peak by a factor of ~ 2 and re-normalizing the state. In this case, the $\mathbf{G}_0$ peak has a positive contribution to v_g. Therefore this population

[3] To be precise, the Bloch state considered at $(V_{\mathrm{SW}}, V_{\mathrm{LW}}) = (25, 15)$ kHz is at $n = 3, k_y = 1.32 \times q_K$ so that comparison with our experimental data can be made. See Fig. 5.6 (a).

redistribution in momentum space is consistent with our understanding that v_g increases as a result of interactions.

Our data show an population increase in the $\mathbf{G}_0$ peak. However, the increase is not as much as predicted by GPE. Also, the changes in other peaks do not follow the GPE predictions very well.

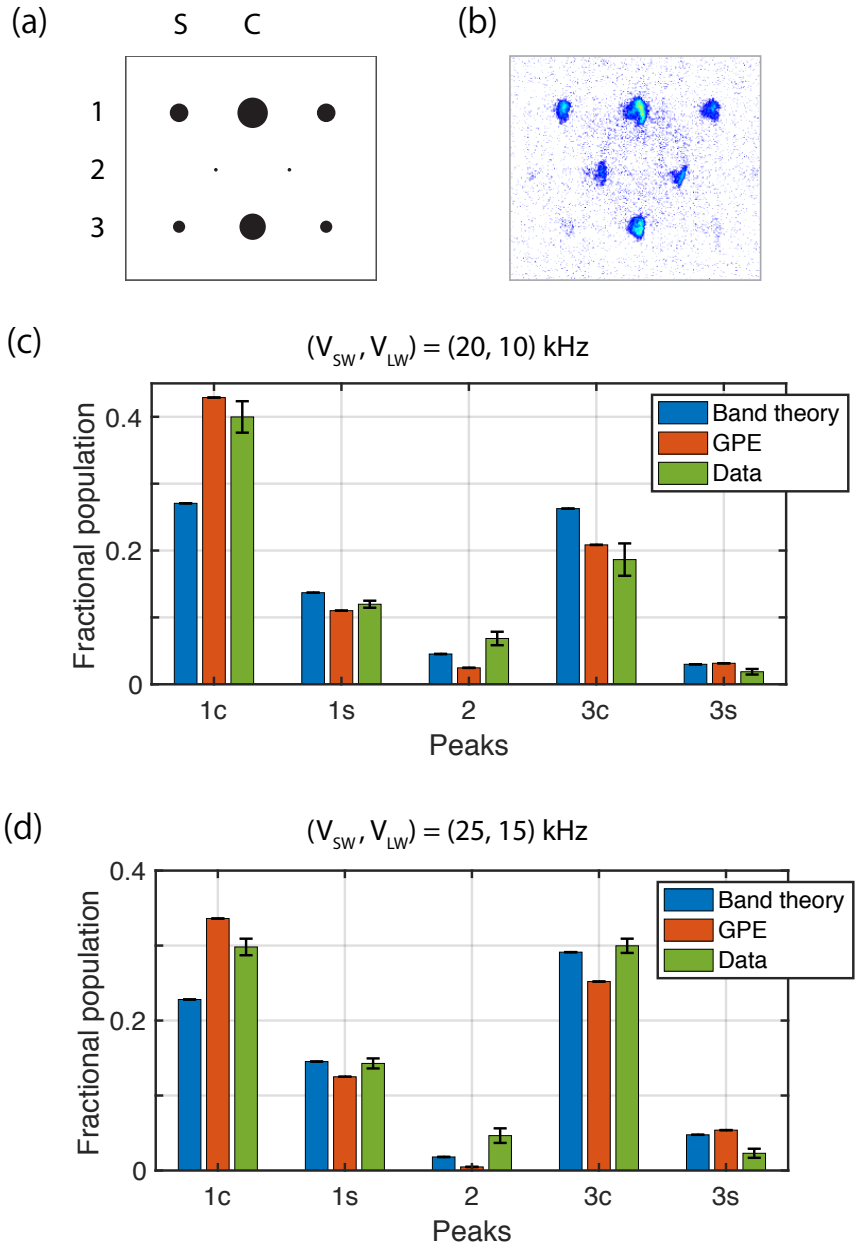

Figure 5.12: Fractional population of different momentum components of the $n = 3, k_y = 1.25 \times q_K$ Bloch state. (a) Labeling of peaks in momentum space. The eight peaks shown make up for $> 95\%$ of the population. (b) Single-shot image of atoms loaded to the corresponding Bloch state. In (c) and (d), fractional population in each momentum peaks calculated with band theory (blue) and GPE (orange) at $(V_{\mathrm{SW}}, V_{\mathrm{LW}}) = (20, 10)$ and (25,15) kHz are shown respectively. In both cases, the $\mathbf{G}_0$ population (peak 1c) is enhanced with interactions, increasing v_g.

Chapter 6

Towards Exploring the Quadratic Band Touching Point

After reporting the details of our work studying the flat $n = 3$ kagome band and its distortion due to interaction effects in Chapter 5, we now look at another interesting aspect of the kagome band structure, namely the quadratic band touching point (QBTP) at Γ in the $n = 2$ and 3 bands.

In the cold atom community, many remarkable experimental works have been done to explore the physics of another, perhaps more widely known, type of band touching point – the Dirac point. This includes the measurement of its topological charge [94], the observation of annihilation of two Dirac points [41], and the study of the topological Haldane model through the opening and closing of the Dirac points [95] etc. However, to the best of our knowledge, QBTPs have never been studied in this field, despite all the theoretical interest they has attracted in recent years [96, 97, 98, 9, 99]. One possible reason is that QBTPs are less accessible as they show up only in the excited bands for common lattice geometries (honeycomb, kagome, checkerboard).

With the newly developed arbitrary phase lock system reported in Chapter 3, we have the capability to put bosons up to $n = 3$ band and move them around in k-space in arbitrary directions. This allows us to explore the kagome QBTP, at least in an out-of-equilibrium fashion. The purpose of this chapter is to present what we have come to understand about the kagome QBTP so far, propose possible experiments and sketch out ideas that might be worth pursuing in the future.

We first go through some theoretical basics under the framework of non-interacting tight-binding model. We propose a simple experiment to demonstrate the singular nature of the QBTP, and demonstrate the idea by showing results from preliminary experiments performed with Dirac points of the honeycomb lattice. Motivated by the experimental findings of [46], we consider how interaction effects could change the properties of the QBTP. Finally, a method of Bloch state reconstruction for characterizing the QBTP and possible interaction effects is outlined.

6.1 Basics

Origin of touching point

To begin with, lets try to understand why there is a touching point at the Γ point of the kagome band structure at all. The non-interacting tight-binding Hamiltonian at Γ is given by

$$H_\Gamma = -2J \begin{pmatrix} 0 & 1 & 1 \\ 1 & 0 & 1 \\ 1 & 1 & 0 \end{pmatrix} \tag{6.1}$$

This matrix has has three-fold rotation (C_3) symmetry. Explicitly, we can write down the C_3 rotation operator as

$$C_3 = \begin{pmatrix} 0 & 1 & 0 \\ 0 & 0 & 1 \\ 1 & 0 & 0 \end{pmatrix} \tag{6.2}$$

which corresponds to the cyclic operation $A \to B \to C \to A$. We can see that $[H_\Gamma, C_3] = 0$, therefore there exists a set of simultaneous eigenstates for the two operators. Those eigenstates are

$$\begin{aligned} |\psi_0\rangle &= \frac{1}{\sqrt{3}}(1,1,1)^T \\ |\psi_{\mathrm{R}}\rangle &= \frac{1}{\sqrt{3}}(1, e^{+i2\pi/3}, e^{+i4\pi/3})^T \\ |\psi_{\mathrm{L}}\rangle &= \frac{1}{\sqrt{3}}(1, e^{-i2\pi/3}, e^{-i4\pi/3})^T \end{aligned} \tag{6.3}$$

The above eigenstates have energies $E_0 = -4J$ and $E_{\mathrm{R/L}} = 2J$ respectively. The two chiral states $\left|\psi_{\mathrm{L/R}}\right\rangle$ are degenerate in energy, leading to a band touching point at Γ. From this perspective, we can see that the touching point is protected by C_3 rotational symmetry and time reversal (T) symmetry – the touching point is robust to any perturbations that respect these two symmetries. For example, for the trimerized kagome lattice, the inversion symmetry is broken but the C_3 and T symmetries are kept. Therefore, its band structure also has a touching point at Γ.

Apart from the symmetry perspective, one can also understand the existence of QBTP through analyzing the completeness of the basis formed by compact local states (CLS). As explained in [10] and mentioned in Chapter 2 of this thesis, states in the flat band can be

written in the basis of CLS. Simple counting argument shows that, in a kagome lattice of N unit cells, only $N-1$ CLS are linearly independent. Therefore a complete eigenbasis cannot be formed with CLS only. It turns out that there are two extra eigenstates for the flat band, known as the non-contractible loop states (NCLS), which are topologically different than CLS [10]. This pair of NCLS must be shared with another band through band touching to avoid over-completeness. Therefore, band touching is required. From this perspective, the existence of a band touching point is enforced by the flatness of the $n = 3$ band [9].

Incidentally, the regular kagome lattice also possesses another type of band touching point, namely the Dirac point, at the K points of the $n = 1$ and $n = 2$ bands. This should not be too surprising given the same underlying Bravais lattice and the shared inversion symmetry for the kagome lattice and the honeycomb lattice – the lattice in which Dirac points are famously known to exist and studied. At the K points, the Hamiltonian (Eq. 5.2) does not have C_3 symmetry but inversion (I) symmetry. Noting that the inversion center is at the center of a hexagon (see Chapter 2), We can write the inversion operator ($A \leftrightarrow B$) for the kagome lattice as

$$I = \begin{pmatrix} 1 & 0 & 0 \\ 0 & 0 & 1 \\ 0 & 1 & 0 \end{pmatrix} \tag{6.4}$$

Again, we can check that $[H_K, I] = 0$. The lower two eigenstates of H_K have two-fold degeneracy, which is protected by I symmetry.

Effective psuedospin-1/2 model

After showing that there is a touching point at Γ for the $n = 2$ and $n = 3$ bands, we now consider its properties. In the neighborhood of the touching point where the ground $n = 1$ band is very far away in energy from the two touching bands, the system can be described with a SO(2) Hilbert subspace spanned by a set of two linearly independent eigenstates at the touching point. There is flexibility in choosing exactly which basis states to work with. One option is to work with the chiral basis introduced in Eq. 6.3. Alternatively, we can choose to work with a basis of real eigenvectors

$$\begin{aligned} |\psi_+\rangle &= \frac{1}{2}(|\psi_R\rangle + |\psi_L\rangle) = \frac{1}{\sqrt{6}}(2,-1,-1)^T \\ |\psi_-\rangle &= \frac{1}{2i}(|\psi_R\rangle - |\psi_L\rangle) = \frac{1}{\sqrt{2}}(0,1,-1)^T \end{aligned} \tag{6.5}$$

To derive the effective Hamiltonian, we rewrite the tight-binding Hamiltonian Eq. 2.5 in the basis defined in Eq. 6.5. We perform an unitary transformation: $H \to U^\dagger H U$, where

$$U = \frac{1}{\sqrt{6}} \begin{pmatrix} \sqrt{2} & 0 & 2 \\ \sqrt{2} & \sqrt{3} & -1 \\ \sqrt{2} & -\sqrt{3} & -1 \end{pmatrix} \tag{6.6}$$

We then truncate the matrix to keep only the subspace associated with the touching bands. Taking the limit of $k \to 0$, we obtain

$$\begin{aligned} H_{\text{QBTP}} &= \begin{pmatrix} 2 - q_y^2 & q_x q_y \\ q_x q_y & 2 - q_x^2 \end{pmatrix} \\ &= B_I \hat{I} + (q_x q_y)\hat{\sigma}_x + (q_x^2/2 - q_y^2/2)\hat{\sigma}_z \\ &\to B_I \hat{I} + (q_x q_y)\hat{\sigma}_y + (q_x^2/2 - q_y^2/2)\hat{\sigma}_x \\ &= B_I \hat{I} + \mathbf{B} \cdot (\hat{\sigma}_x, \hat{\sigma}_y) \end{aligned} \tag{6.7}$$

where $B_I = (2 - q_x^2/2 - q_y^2/2)J$, $\mathbf{B} = (B_x, B_y)$ with $B_x = (q_x^2/2 - q_y^2/2)J$ and $B_y = q_x q_y J$, σ_x, σ_y are Pauli matrices and $\hat{I}$ is the identity matrix. In the second last line the basis is rotated again so that the Cartesian axis labels are cyclically swapped ($X \to Y \to Z \to X$). This does not change the physics but provides us a neat picture to describe the touching point. Now, the Hamiltonian is written in the basis of $|\psi_\uparrow\rangle = (|\psi_+\rangle + |\psi_-\rangle)/\sqrt{2}$ and $|\psi_\downarrow\rangle = (|\psi_+\rangle - |\psi_-\rangle)/\sqrt{2}$. These two states form a psuedospin-1/2 system.

The effective Hamiltonian provides an intuitive picture to understand the physics around the touching point: the system is equivalent to a spin-1/2 particle placed in a spatially varying, in-plane magnetic field in k-space. We can immediately apply well-known results for such a system to learn something about the touching point. The eigenstates of the system at an arbitrary position (q_x, q_y) in k-space is a superposition of the two pseudospin states with a relative phase of $\tan^{-1}(B_y/B_x)$. In the Bloch sphere representation, the ground (excited) state simply points opposite to (along the same direction as) the field. For example, if $q_y = 0$, the field is pointing along x direction, and the Hamiltonian is reduced to the $\hat{\sigma}_x$ operator. In this case, the ground state is $(|\psi_\uparrow\rangle - |\psi_\downarrow\rangle)/\sqrt{2} = |\psi_-\rangle$, and the excited state is $(|\psi_\uparrow\rangle + |\psi_\downarrow\rangle)/\sqrt{2} = |\psi_+\rangle$.

Moreover, the energy of the ground state is $B_I - |\mathbf{B}| = (2 - |k|^2)J$. From this we see explicitly the quadratic dependence of the ground state energy on $|k|$. For the excited state, the energy is $B_I + |\mathbf{B}| = 2J$, independent of $\mathbf{q}$. This is consistent with the fact that the higher energy band is the flat band.

The fictitious field is plotted in Fig. 6.1. Note that the field has a winding number of 2 around the QBTP (which can also be seen by observing that the off-diagonal terms of H_{QBTP} are in the form of $(q_x \pm i q_y)^2$). Therefore, the Berry flux through an area enclosing the QBTP is 2π, which cannot be distinguished from zero with established interferometric techniques that have been used to measure the Berry flux through a Dirac point with a winding number

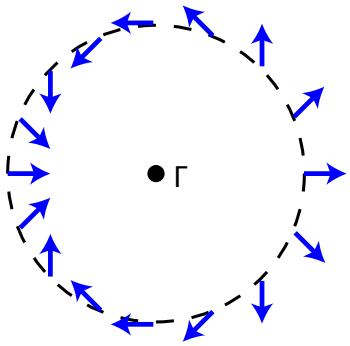

Figure 6.1: Fictitious magnetic field (blue arrows) experienced by the psuedospin in the effective model near QBTP. The field is inversion symmetric about the QBTP. The magnitude of the field increases quadratically as $|\mathbf{q}|^2$.

of 1 and a Berry phase of π (cite duca15). However, a QBTP can be split into two Dirac points if perturbations of certain types are introduced to reduce the symmetry of the kagome lattice (cite kai09). In that case, the total Berry flux of a QBTP can be measured via the two daughter Dirac points.

6.2 Diabatic state transfer

Exactly at the QBTP, the fictitious field vanishes. The psuedospin can point in any direction at this point and remain an eigenstate. This is because the two psuedospin states are degenerate at QBTP, therefore any combination of them is an eigenstate. In other words, the eigenstate at the QBTP is not well-defined. The actual state of the system at the QBTP depends on the trajectory it took to get there.

Let's consider what happens if the system takes a trajectory in momentum space that crosses the QBTP. For example, suppose the system takes a linear trajectory, i.e. it undergoes one dimensional acceleration. In this case, crossing the QBTP does not lead to any state transfer. In the pseudospin picture, the fictitious field along such a trajectory points to the same direction on both sides of the QBTP. Therefore, the orientation of the spin respective to the field is the same before and after crossing the QBTP.

Now, suppose the system takes a different trajectory that it makes a turn, say at an angle of $\pi/2$, at the QBTP. In this case, as we can see from Fig. 6.1, the fictitious field direction flips upon crossing the QBTP. As a result, the ground and excited states of the system swap – the psuedospin state that is aligned (anti-aligned) with the field before crossing the QBTP becomes anti-aligned (aligned) with the field after doing so. The system therefore undergoes a complete, diabatic change of state. Note that it has nothing to do with how slow the above

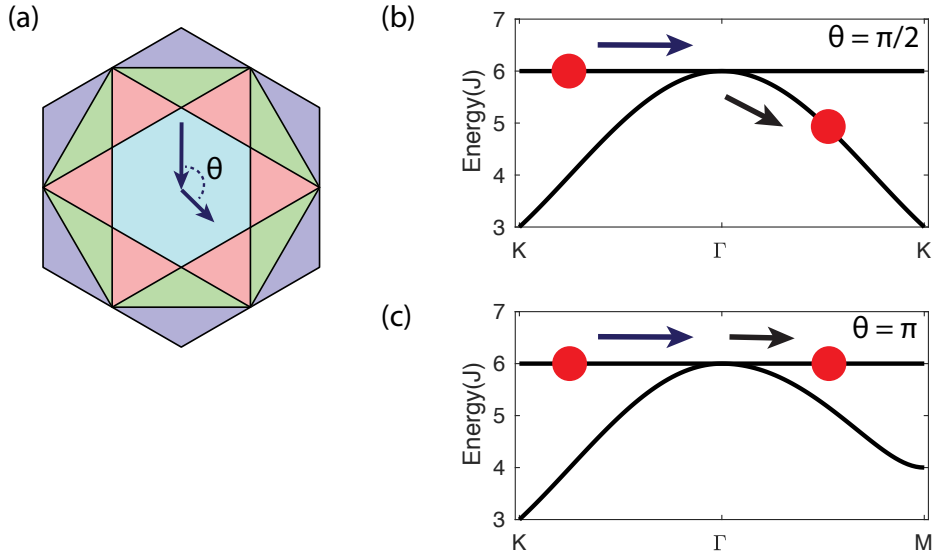

Figure 6.2: Path dependent band transfer at the QBTP. (a) A map of Brillouzin zones. Two paths crossing the QBTP are considered here. Starting from a K point, (b) one goes straight through the QBTP to the opposite K point, (c) one makes a right-angled turn towards M. There is no band transfer in the former case, and complete band transfer in the latter.

process takes place. Such a change in the state of the system reveals the singular nature of the QBTP.

Based on the above observations, we propose an experiment to indirectly measure the Berry flux through the QBTP. The idea is as follows. We begin with loading atoms into either the $n = 2$ or $n = 3$ band. Then we perform two-step acceleration, which first takes the atoms exactly to the QBTP (entry path), and then away from it at a variable angle θ (exit path). See Fig. 6.2. The population that remains in the original band should vary as $\cos^2(\theta)$. For instance, as explained above, at $\theta = \pi$ the system remains in the same band ($\cos^2(\theta) = 1$), while at $\theta = \pi/2$, the system undergoes a complete band transfer ($\cos^2(\theta) = 0$). The population in the two bands can be measured by the standard band mapping technique.

Measuring band transfer at Dirac point

The experiment proposed above is preliminarily tested in a simpler setting with a Dirac point of our LW honeycomb lattice. In this section, we will briefly discuss the experimental protocol, show the data and discuss how we analyze them.

Similar to the case of QBTP, an effective pseudospin model can be derived for describing the physics in the neighborhood of the Dirac points. We omit the derivations here, as they can be found easily in the literature [100] and various pedagogical materials available online.

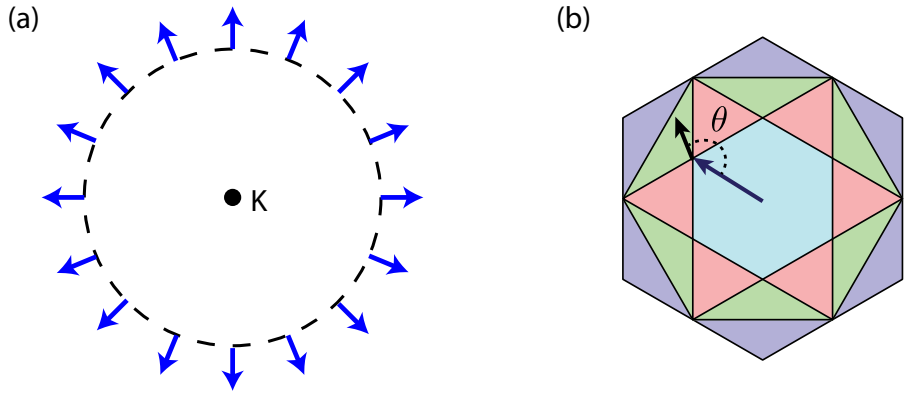

Figure 6.3: (a) Fictitious magnetic field (blue arrows) experienced by the pseudospin in the effective model near a Dirac point. The field is inversion-asymmetric about the Dirac point. The magnitude of the field increases linearly with $|\mathbf{q}|$. (b) Experimental scheme with two-step acceleration. Atoms are first accelerated from Γ to a Dirac point, and then are accelerated again to a quasimomentum away from the Dirac point along a path at an angle θ to the entry path.

We point out that the fictitious field in the case of Dirac points has a winding number of 1. Therefore, the band population measured in the proposed experiment should vary as $\cos^2(\theta/2)$ (see Fig. 6.3 (a)).

Experimental Protocol In this experiment, acceleration of atoms happens in the reference frame of a moving lattice. Employing the arbitrary phase lock system described in Chapter 3, we can frequency-detune the LW lattice beams to accelerate the honeycomb lattice along any direction in the lattice plane.

After loading atoms into the ground state of the LW honeycomb lattice, we accelerate the lattice by linearly increasing the frequency detuning of one lattice beam from zero to a value corresponding to $\mathbf{v}_K$ in 300 μs. The atoms are thus taken to a K point in the lattice frame. Immediately after that, we accelerate the lattice again by linearly increasing the frequency detunings of two lattice beams in 300 μs. The ratio of the final detunings is determined by the desired final quasimomentum $\mathbf{q}$ of atoms in the lattice frame (see Chapter 3.4.5). For this experiment we choose to perform measurements at quasimomenta $|\mathbf{q}/m - \mathbf{v}_K| = 0.3|\mathbf{v}_K|$ away from the Dirac point at various angles $\theta = \pi/6 + n \times \pi/4$, where n is an integer. To measure the band populations, we ramp down our lattices with the reversed ramp function in Eq. 5.13. Images are taken with the momentum space focusing technique.

Data Analysis The bandmapping pictures obtained in the experiment are shown in Fig. 6.4. In each picture, atoms show up as density peaks at a few different locations related by

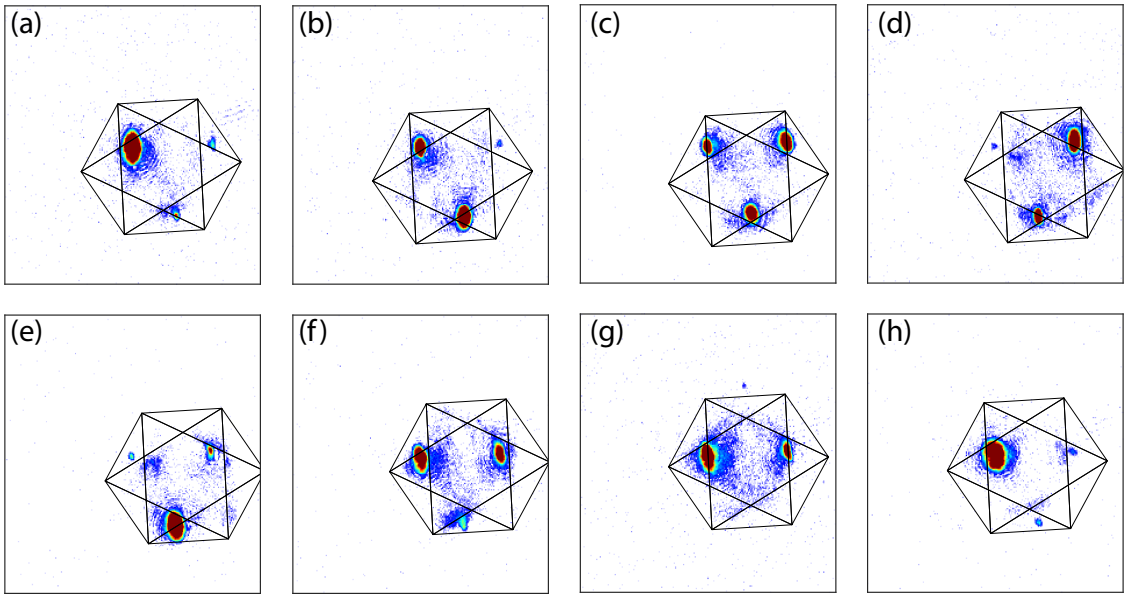

Figure 6.4: Band mapping images, with a map of Brillouin zones overlaid, taken in the experiments performed at different angles $\theta = \pi/6$ plus increments of $\pi/4$. A density peak within the n-th Brillouin zone represents the system's population in the n-th band in the lattice. The locations of the peaks are determined by their centers. For (c) and (g), band mapping is performed on a boundary of two Brillouin zones and therefore population in each band cannot be unambiguously determined.

the reciprocal lattice vectors. The number of atoms in these peaks represent the population in different bands. A density peak at specific location can represent different bands in different images, depending on the quasimomentum of the atoms in the lattice frame. To find out which band each peak represent, we overlay a map of Brillouin zones on top of each image. The center of the map is placed at a position that corresponds to the velocity at which the LW lattice is moving, such that the images are analyzed in the lattice frame. In general, the density peaks show up in different Brillouin zones. A peak that shows up in the n-th Brillouin zone represent the population in the n-th band. In this experiment, some data are taken on a boundary of Brillouin zones. There, the two bands represented by the Brillouin zones on the two sides of the boundary have a vanishing gap when the lattice is turned off. As a result, band transfer can happen during the band mapping procedure, and the number of atoms in the on-boundary density peaks does not uniquely represent population in a single band.

The bond populations extracted from the band mapping images (excluding the ones measured on the boundaries of Brillouin zones) are shown plotted in Fig. 6.5. The data show qualitatively the right behavior we expect. At θ around 0 and 2π, the direction of the

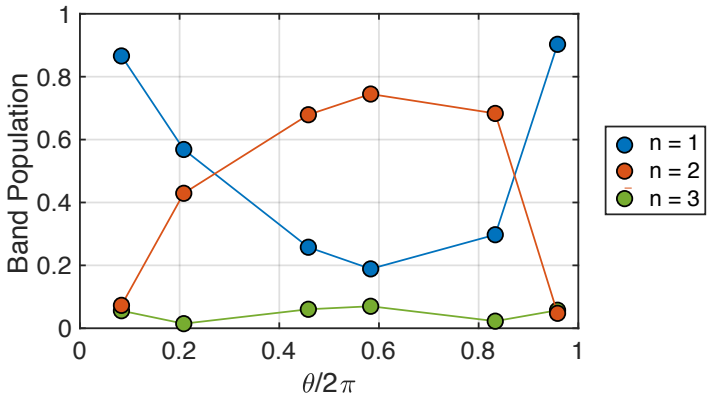

Figure 6.5: Band populations extracted from band mapping images at different exit path angle θ. Data taken on a boundary of Brillouin zones are not plotted as band populations can not be extracted from band mapping images.

fictitious field is similar to that along the entry path. Therefore the atoms mostly remain in the ground band of the system. Near $\theta = \pi$, however, the fictitious field points in an opposite direction. Atoms undergo a diabatic transition into the upper band upon crossing the Dirac point.

This preliminary result is promising. Yet, many questions need to be addressed. For example, how does the time scale of acceleration change the measurement outcome? Ideally we want to do the measurement slowly as long as instability is not a problem to reveal the touching-point singularity effect. Another question concerns the cause of the imperfect contrast at $\theta = \pi$ in Fig. 6.5. It would be interesting to investigate whether it comes from interaction effects which are known to significantly modify the band structure around the Dirac point [71]. In fact, interactions can significantly complicate the interpretation of these band mapping pictures. This will be the focus of the next section.

6.3 Interaction effects

It is natural to ask, especially in the light of our experimental findings about the distorted $n = 3$ band, how much of the discussion about the QBTP in the last section is still valid in the presence of interactions. In this section, we take a closer look at the mean-field tight-binding Hamiltonian $H_{\mathrm{MF}} = H_0 + H_{\mathrm{I}}$ in Eq. 5.1 and investigate how interactions could modify the QBTP.

Let's begin by examining the effects of interactions on the eigenstates at Γ. In general, the eigenstates of a system in the non-interacting limit are no longer eigenstates when interactions are present. However, in some cases, they are. Consider the simultaneous eigenstates of the non-interacting Hamiltonian H_0 and the C_3 operator: $|\psi_0\rangle$ and $|\psi_{\mathrm{L/R}}\rangle$ (Eq. 6.5). The

density distribution of all these three states are uniform, with a fraction population of $1/\sqrt{3}$ in each of the three sites in a unit cell. The mean-field interaction matrix is then given by $(U/3)\hat{I}$. Therefore, all these three states are eigenstates of both H_0 and H_{I} of the total Hamiltonian (Eq. 5.1), and therefore remain eigenstates of the system. The mere effect of interactions on these states is that their energies are increased by $U/3$.

This is not the end of the story. Because of the nonlinear interacting term, the system can have more solutions than allowed in the non-interacting case. Consider the two superposition states $|\psi_{\pm}\rangle$ (Eq. 6.5). For $|\psi_{-}\rangle = \frac{1}{\sqrt{2}}(0,1,-1)^T$ the density is uniform among the two sites that are occupied, and H_{I} takes the form of an identity matrix within the subspace spanned by the two occupied sites. Therefore, ψ_{-} is an eigenstate of both H_0 and H_{I}, and also an eigenstate of the total Hamiltonian. Note that its energy scales as $U/2$, which is different from $|\psi_0\rangle$ and $\left|\psi_{\mathrm{L/R}}\right\rangle$. Moreover, as the system is C_3 symmetric, we can immediately find two more eigenstates by rotating $|\psi_{-}\rangle$ by $2\pi/3$ and $4\pi/3$. In other words, $\frac{1}{\sqrt{2}}(0,1,-1)^T$ and its two cyclic permutations form a set of C_3-related degenerate eigenstates.

Finally, let's look at $|\psi_{+}\rangle = \frac{1}{\sqrt{6}}(2,-1,-1)^T$. This state has non-uniform density distribution among the three sites in a unit cell. Unlike the other states we have looked at, it is not an eigenstate of H_I. It is also not an eigenstate of the total Hamiltonian H_{MF}. This demonstrates that the principle of superposition does not hold for nonlinear systems, as both $|\psi_{\mathrm{R}}\rangle$ and $|\psi_{\mathrm{L}}\rangle$ are eigenstates of H_{MF} but $|\psi_{+}\rangle = |\psi_{\mathrm{R}}\rangle + |\psi_{\mathrm{L}}\rangle$ is not. From what we have learned about the $n = 3, k_y = 1.25 \times q_K$ Bloch state in section 5.1, we expect that with interactions, atoms will redistribute to enhance density difference which already exists in the non-interacting limit. With increasing interactions, $|\psi_{+}\rangle$ should approach $(1,0,0)$. This makes sense, as $(1,0,0)$ is an eigenstate of the system in the strong interaction limit of $J/U \to 0$. Again, because of C_3 symmetry, we have a set of C_3-related eigenstates that occupies mostly one site ($(1,0,0)$ and its cyclic permutations). The energy of these states with single-site occupancy scales as U.

The eigenstates at Γ, their energy dependence scaling and the degeneracy are summarized in Table 6.1. Instead of having three solutions as in the non-interacting limit, we have nine different solutions. We have numerically solved Eq. 5.1 to confirm that we have exhausted all the solutions. Clearly, the pseudospin picture is no longer an adequate description of the system.

Nonlinear band structure

We have seen that at Γ new eigenstates emerge as a result of non-zero interactions. If we zoom out and look at the full band structure, we will see new energy bands and a lot of subtle details around places where different bands touch and cross. Band structure cut-throughs numerically calculated by solving Eq. 5.1 at a few values of U/J are shown in Fig. 6.6.

As we have already seen in the previous section (Table 6.1), for nonzero U/J, four different eigenenergies can be found at Γ. They correspond to nine different eigenstates with four different energy scalings with U. However, if we move away from Γ, the C_3 rotational symmetry is broken and, depending on the specific value of quasimomentum,

Eigenstates	Energy	Degeneracy
$\frac{1}{\sqrt{3}}(1,1,1)^T$	-4J+U/3	1
$\frac{1}{\sqrt{3}}(1, e^{\pm i2\pi/3}, e^{\pm i4\pi/3})$	2J+U/3	2
$\frac{1}{\sqrt{2}}(1,-1,0)^T$ and C_3 partners	2J+U/2	3
$\frac{1}{\sqrt{6}}(2,1,1) \rightarrow (1,0,0)$ and C_3 partners	$2J \rightarrow U$	3

Table 6.1: All eigenstates of the interacting tight-binding Hamiltonian H_{MF} (Eq. 5.1) at Γ.

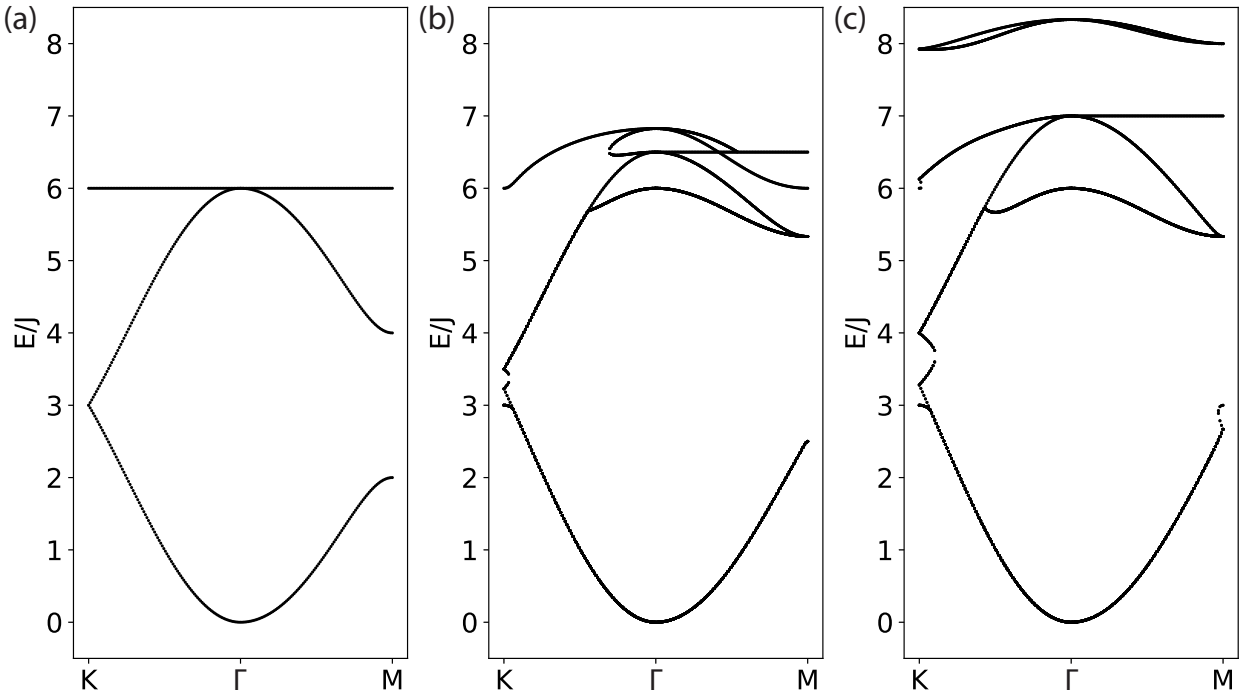

Figure 6.6: Band structure cut-through numerically calculated with H_{MF} (Eq. 5.1) at (a) $U/J = 0$, (b) $U/J = 3$ and (c) $U/J = 6$.

more or less eigenenergies can be found. Note that in Fig. 6.6 we plot the band structure along the symmetry line $K - \Gamma - M$, so mirror symmetry is kept and some bands are still doubly degenerate. When $U/J = 3$, excited bands cross or merge into each other at various quasimomenta away from Γ. When $U/J = 6$, the difference in energy scaling with U completely separates the bands associated with states that occupy two sites and those associated with states that occupy mostly one site.

Consider again what happens if we accelerate atoms from K to Γ in the highest band and make a turn to M (Fig. 6.2). At $U/J = 0$, atoms undergo diabatic transfer once to the second band at Γ as explained before. At $U/J = 3$, atoms undergo band transfer twice. The first transfer takes place at Γ with the other two degenerate C_3 related bands, and the second transfer takes place some distance away with a band that stems from a $|\psi_-\rangle$ state at Γ. At stronger interactions $U/J = 6$, the two sets of bands stemming from $|\psi_-\rangle$ and $|\psi_+\rangle$ completely separate. There is only one band transfer at Γ, again with the other two degenerate C_3 related bands.

It is unclear how band mapping exactly works for an interacting systems. Bands emerging from interactions cease to exist below certain interaction strengths. Therefore in the process of ramping down the lattice, such bands disappear and do not smoothly connect to the free particle dispersion curve. In this regard, band mapping may not be a useful tool to examine what is happening in the system.

6.4 Quantum state reconstruction

In this final section, we discuss the possibility of reconstructing the full quantum state of atoms near the QBTP. The capability to do so will let us directly probe the geometry of the band around the QBTP, perform a direct measurement of the quantum distance [99], and study interaction effects.

In section 2.5, we derived the momentum distribution of atoms for a generic state (Eq. 2.31). In general, we can make no assumptions about the populations and the phases of different Wannier states $|\alpha\rangle$. Clearly it is not possible to reconstruct the full quantum state by just looking at diffraction patterns, as some information of the system is lost when only the density of the momentum distribution is measured. However, if we combine momentum and real-space density distributions, then it is possible. While the momentum density distribution is measured with time-of-flight images of atoms, the real space density distribution can be measured by a technique called site mapping [101]. In this technique, the lattice depth is suddenly deepened to freeze out the motion of atoms. An extra potential (e.g. an additional lattice, or external magnetic field) is applied to introduce large and different energy offsets to lattice sites. If the differences in the offsets are large enough that there is no coupling between different sites, each site is then exclusively associated with a single band. The population in each site can then be measured by standard band mapping measurements.

Combining these two measurements, we show that it is possible to perform a full reconstruction of the quantum state. We focus on the case where the superlattice has the kagome geometry ($P_D = 0$). Also, for the purpose of measuring the quantum distance, we only concern small values of $\mathbf{q}$, such that we can make the following approximation: $|\tilde{W}(\mathbf{q}_0 + \mathbf{G})|^2 \simeq 1 - |\mathbf{q}_0 + \mathbf{G}|^2/a_w^2$. As the population in each site is measured by site mapping, we only have 3 unknown variables: θ_{AB}, θ_{BC} and θ_{AC}. We combine equations (2.35) to (2.37) and obtain the following expression for each pair of i and j:

$$\begin{aligned}
&\frac{n(\mathbf{q}_0+\mathbf{G}_i)+n(\mathbf{q}_0-\mathbf{G}_i)}{n(\mathbf{q}_0+\mathbf{G}_j)+n(\mathbf{q}_0-\mathbf{G}_j)} \\
&= \underbrace{\left(\frac{|\tilde{W}(\mathbf{q}_0+\mathbf{G}_i)|^2+|\tilde{W}(\mathbf{q}_0-\mathbf{G}_i)|^2}{|\tilde{W}(\mathbf{q}_0+\mathbf{G}_j)|^2+|\tilde{W}(\mathbf{q}_0-\mathbf{G}_j)|^2}\right)}_{\simeq 1} \frac{1+\sum_{i>j} 2\cos(\mathbf{G}_i\cdot(\mathbf{R}_i-\mathbf{R}_j))\cos(\theta_{ij})\sqrt{P_iP_j}}{1+\sum_{i>j} 2\cos(\mathbf{G}_j\cdot(\mathbf{R}_i-\mathbf{R}_j))\cos(\theta_{ij})\sqrt{P_iP_j}}
\end{aligned} \tag{6.8}$$

All the populations $n(\mathbf{q}_0 \pm \mathbf{G})$ are measured in diffraction images. Hence, Eq. 6.8 represents a solvable system of three equations and three unknowns.

Bibliography

[1] P. W. ANDERSON. "The Resonating Valence Bond State in La2CuO4 and Superconductivity". In: *Science* 235.4793 (1987), pp. 1196–1198. ISSN: 0036-8075. DOI: 10.1126/science.235.4793.1196. eprint: https://science.sciencemag.org/content/235/4793/1196.full.pdf. URL: https://science.sciencemag.org/content/235/4793/1196.

[2] Leon Balents. "Spin liquids in frustrated magnets". In: *Nature* 464.7286 (2010), pp. 199–208. DOI: 10.1038/nature08917. URL: https://doi.org/10.1038/nature08917.

[3] Yi Zhou, Kazushi Kanoda, and Tai-Kai Ng. "Quantum spin liquid states". In: *Rev. Mod. Phys.* 89 (2 Apr. 2017), p. 025003. DOI: 10.1103/RevModPhys.89.025003. URL: https://link.aps.org/doi/10.1103/RevModPhys.89.025003.

[4] Ying Ran et al. "Projected-Wave-Function Study of the Spin-1/2 Heisenberg Model on the Kagomé Lattice". In: *Phys. Rev. Lett.* 98 (11 Mar. 2007), p. 117205. DOI: 10.1103/PhysRevLett.98.117205. URL: https://link.aps.org/doi/10.1103/PhysRevLett.98.117205.

[5] Michael Hermele et al. "Properties of an algebraic spin liquid on the kagome lattice". In: *Phys. Rev. B* 77 (22 June 2008), p. 224413. DOI: 10.1103/PhysRevB.77.224413. URL: https://link.aps.org/doi/10.1103/PhysRevB.77.224413.

[6] A. Olariu et al. "^{17}O NMR Study of the Intrinsic Magnetic Susceptibility and Spin Dynamics of the Quantum Kagome Antiferromagnet $ZnCu_3(OH)_6Cl_2$". In: *Phys. Rev. Lett.* 100 (8 Feb. 2008), p. 087202. DOI: 10.1103/PhysRevLett.100.087202. URL: https://link.aps.org/doi/10.1103/PhysRevLett.100.087202.

[7] P. Khuntia et al. "Gapless ground state in the archetypal quantum kagome antiferromagnet ZnCu3(OH)6Cl2". In: *Nature Physics* 16.4 (2020), pp. 469–474. DOI: 10.1038/s41567-020-0792-1. URL: https://doi.org/10.1038/s41567-020-0792-1.

[8] C. Broholm et al. "Quantum spin liquids". In: *Science* 367.6475 (2020). ISSN: 0036-8075. DOI: 10.1126/science.aay0668. eprint: https://science.sciencemag.org/content/367/6475/eaay0668.full.pdf. URL: https://science.sciencemag.org/content/367/6475/eaay0668.

[9] Jun-Won Rhim and Bohm-Jung Yang. "Classification of flat bands according to the band-crossing singularity of Bloch wave functions". In: *Phys. Rev. B* 99 (4 Jan. 2019), p. 045107. DOI: 10.1103/PhysRevB.99.045107. URL: https://link.aps.org/doi/10.1103/PhysRevB.99.045107.

[10] Doron L. Bergman, Congjun Wu, and Leon Balents. "Band touching from real-space topology in frustrated hopping models". In: *Phys. Rev. B* 78 (12 Sept. 2008), p. 125104. DOI: 10.1103/PhysRevB.78.125104. URL: https://link.aps.org/doi/10.1103/PhysRevB.78.125104.

[11] Sebastian D. Huber and Ehud Altman. "Bose condensation in flat bands". In: *Phys. Rev. B* 82 (18 Nov. 2010), p. 184502. DOI: 10.1103/PhysRevB.82.184502. URL: https://link.aps.org/doi/10.1103/PhysRevB.82.184502.

[12] Yi-Zhuang You et al. "Superfluidity of Bosons in Kagome Lattices with Frustration". In: *Phys. Rev. Lett.* 109 (26 Dec. 2012), p. 265302. DOI: 10.1103/PhysRevLett.109.265302. URL: https://link.aps.org/doi/10.1103/PhysRevLett.109.265302.

[13] A Mielke. "Ferromagnetic ground states for the Hubbard model on line graphs". In: *Journal of Physics A: Mathematical and General* 24.2 (Jan. 1991), pp. L73–L77. DOI: 10.1088/0305-4470/24/2/005. URL: https://doi.org/10.1088/0305-4470/24/2/005.

[14] A Mielke. "Exact ground states for the Hubbard model on the Kagome lattice". In: *Journal of Physics A: Mathematical and General* 25.16 (Aug. 1992), pp. 4335–4345. DOI: 10.1088/0305-4470/25/16/011. URL: https://doi.org/10.1088/0305-4470/25/16/011.

[15] N. B. Kopnin, T. T. Heikkilä, and G. E. Volovik. "High-temperature surface superconductivity in topological flat-band systems". In: *Phys. Rev. B* 83 (22 June 2011), p. 220503. DOI: 10.1103/PhysRevB.83.220503. URL: https://link.aps.org/doi/10.1103/PhysRevB.83.220503.

[16] Hoi Chun Po et al. "Origin of Mott Insulating Behavior and Superconductivity in Twisted Bilayer Graphene". In: *Phys. Rev. X* 8 (3 Sept. 2018), p. 031089. DOI: 10.1103/PhysRevX.8.031089. URL: https://link.aps.org/doi/10.1103/PhysRevX.8.031089.

[17] Bitan Roy and Vladimir Juri či ć. "Unconventional superconductivity in nearly flat bands in twisted bilayer graphene". In: *Phys. Rev. B* 99 (12 Mar. 2019), p. 121407. DOI: 10.1103/PhysRevB.99.121407. URL: https://link.aps.org/doi/10.1103/PhysRevB.99.121407.

[18] Leon Balents et al. "Superconductivity and strong correlations in moiréflat bands". In: *Nature Physics* 16.7 (2020), pp. 725–733. DOI: 10.1038/s41567-020-0906-9. URL: https://doi.org/10.1038/s41567-020-0906-9.

[19] Evelyn Tang, Jia-Wei Mei, and Xiao-Gang Wen. "High-Temperature Fractional Quantum Hall States". In: *Phys. Rev. Lett.* 106 (23 June 2011), p. 236802. DOI: 10.1103/PhysRevLett.106.236802. URL: https://link.aps.org/doi/10.1103/PhysRevLett.106.236802.

[20] Kai Sun et al. "Nearly Flatbands with Nontrivial Topology". In: *Phys. Rev. Lett.* 106 (23 June 2011), p. 236803. DOI: 10.1103/PhysRevLett.106.236803. URL: https://link.aps.org/doi/10.1103/PhysRevLett.106.236803.

[21] Titus Neupert et al. "Fractional Quantum Hall States at Zero Magnetic Field". In: *Phys. Rev. Lett.* 106 (23 June 2011), p. 236804. DOI: 10.1103/PhysRevLett.106.236804. URL: https://link.aps.org/doi/10.1103/PhysRevLett.106.236804.

[22] Oleg Derzhko, Johannes Richter, and Mykola Maksymenko. "Strongly correlated flat-band systems: The route from Heisenberg spins to Hubbard electrons". In: *International Journal of Modern Physics B* 29.12 (2015), p. 1530007. DOI: 10.1142/S0217979215300078. eprint: https://doi.org/10.1142/S0217979215300078. URL: https://doi.org/10.1142/S0217979215300078.

[23] Daniel Leykam, Alexei Andreanov, and Sergej Flach. "Artificial flat band systems: from lattice models to experiments". In: *Advances in Physics: X* 3.1 (2018), p. 1473052. DOI: 10.1080/23746149.2018.1473052. eprint: https://doi.org/10.1080/23746149.2018.1473052. URL: https://doi.org/10.1080/23746149.2018.1473052.

[24] I. M. Georgescu, S. Ashhab, and Franco Nori. "Quantum simulation". In: *Rev. Mod. Phys.* 86 (1 Mar. 2014), pp. 153–185. DOI: 10.1103/RevModPhys.86.153. URL: https://link.aps.org/doi/10.1103/RevModPhys.86.153.

[25] Immanuel Bloch, Jean Dalibard, and Wilhelm Zwerger. "Many-body physics with ultracold gases". In: *Rev. Mod. Phys.* 80 (3 July 2008), pp. 885–964. DOI: 10.1103/RevModPhys.80.885. URL: https://link.aps.org/doi/10.1103/RevModPhys.80.885.

[26] Christian Gross and Immanuel Bloch. "Quantum simulations with ultracold atoms in optical lattices". In: *Science* 357.6355 (2017), pp. 995–1001. ISSN: 0036-8075. DOI: 10.1126/science.aal3837. eprint: https://science.sciencemag.org/content/357/6355/995.full.pdf. URL: https://science.sciencemag.org/content/357/6355/995.

[27] Florian Schäfer et al. "Tools for quantum simulation with ultracold atoms in optical lattices". In: *Nature Reviews Physics* 2.8 (2020), pp. 411–425. DOI: 10.1038/s42254-020-0195-3. URL: https://doi.org/10.1038/s42254-020-0195-3.

[28] R. Blatt and C. F. Roos. "Quantum simulations with trapped ions". In: *Nature Physics* 8.4 (2012), pp. 277–284. DOI: 10.1038/nphys2252. URL: https://doi.org/10.1038/nphys2252.

[29] Andrew A. Houck, Hakan E. Türeci, and Jens Koch. "On-chip quantum simulation with superconducting circuits". In: *Nature Physics* 8.4 (2012), pp. 292–299. DOI: 10.1038/nphys2251. URL: https://doi.org/10.1038/nphys2251.

[30] Alán Aspuru-Guzik and Philip Walther. "Photonic quantum simulators". In: *Nature Physics* 8.4 (2012), pp. 285–291. DOI: 10.1038/nphys2253. URL: https://doi.org/10.1038/nphys2253.

[31] William D. Phillips. "Nobel Lecture: Laser cooling and trapping of neutral atoms". In: *Rev. Mod. Phys.* 70 (3 July 1998), pp. 721–741. DOI: 10.1103/RevModPhys.70.721. URL: https://link.aps.org/doi/10.1103/RevModPhys.70.721.

[32] Claude N. Cohen-Tannoudji. "Nobel Lecture: Manipulating atoms with photons". In: *Rev. Mod. Phys.* 70 (3 July 1998), pp. 707–719. DOI: 10.1103/RevModPhys.70.707. URL: https://link.aps.org/doi/10.1103/RevModPhys.70.707.

[33] E. A. Cornell and C. E. Wieman. "Nobel Lecture: Bose-Einstein condensation in a dilute gas, the first 70 years and some recent experiments". In: *Rev. Mod. Phys.* 74 (3 Aug. 2002), pp. 875–893. DOI: 10.1103/RevModPhys.74.875. URL: https://link.aps.org/doi/10.1103/RevModPhys.74.875.

[34] Wolfgang Ketterle. "Nobel lecture: When atoms behave as waves: Bose-Einstein condensation and the atom laser". In: *Rev. Mod. Phys.* 74 (4 Nov. 2002), pp. 1131–1151. DOI: 10.1103/RevModPhys.74.1131. URL: https://link.aps.org/doi/10.1103/RevModPhys.74.1131.

[35] K. B. Davis et al. "Bose-Einstein Condensation in a Gas of Sodium Atoms". In: *Phys. Rev. Lett.* 75 (22 Nov. 1995), pp. 3969–3973. DOI: 10.1103/PhysRevLett.75.3969. URL: https://link.aps.org/doi/10.1103/PhysRevLett.75.3969.

[36] M. H. Anderson et al. "Observation of Bose-Einstein Condensation in a Dilute Atomic Vapor". In: *Science* 269.5221 (1995), pp. 198–201. ISSN: 0036-8075. DOI: 10.1126/science.269.5221.198. eprint: https://science.sciencemag.org/content/269/5221/198.full.pdf. URL: https://science.sciencemag.org/content/269/5221/198.

[37] B. DeMarco and D. S. Jin. "Onset of Fermi Degeneracy in a Trapped Atomic Gas". In: *Science* 285.5434 (1999), pp. 1703–1706. ISSN: 0036-8075. DOI: 10.1126/science.285.5434.1703. eprint: https://science.sciencemag.org/content/285/5434/1703.full.pdf. URL: https://science.sciencemag.org/content/285/5434/1703.

[38] J Hecker Denschlag et al. "A Bose-Einstein condensate in an optical lattice". In: *Journal of Physics B: Atomic, Molecular and Optical Physics* 35.14 (July 2002), pp. 3095–3110. DOI: 10.1088/0953-4075/35/14/307. URL: https://doi.org/10.1088/0953-4075/35/14/307.

[39] Markus Greiner et al. "Quantum phase transition from a superfluid to a Mott insulator in a gas of ultracold atoms". In: *Nature* 415.6867 (2002), pp. 39–44. DOI: 10.1038/415039a. URL: https://doi.org/10.1038/415039a.

[40] C Becker et al. "Ultracold quantum gases in triangular optical lattices". In: *New Journal of Physics* 12.6 (June 2010), p. 065025. DOI: 10.1088/1367-2630/12/6/065025. URL: https://doi.org/10.1088%2F1367-2630%2F12%2F6%2F065025.

[41] Leticia Tarruell et al. "Creating, moving and merging Dirac points with a Fermi gas in a tunable honeycomb lattice". In: *Nature* 483.7389 (2012), pp. 302–305. DOI: 10.1038/nature10871. URL: https://doi.org/10.1038/nature10871.

[42] J. Sebby-Strabley et al. "Lattice of double wells for manipulating pairs of cold atoms". In: *Phys. Rev. A* 73 (3 Mar. 2006), p. 033605. DOI: 10.1103/PhysRevA.73.033605. URL: https://link.aps.org/doi/10.1103/PhysRevA.73.033605.

[43] Shintaro Taie et al. "Coherent driving and freezing of bosonic matter wave in an optical Lieb lattice". In: *Science Advances* 1.10 (2015). DOI: 10.1126/sciadv.1500854. eprint: https://advances.sciencemag.org/content/1/10/e1500854.full.pdf. URL: https://advances.sciencemag.org/content/1/10/e1500854.

[44] Gyu-Boong Jo et al. "Ultracold Atoms in a Tunable Optical Kagome Lattice". In: *Phys. Rev. Lett.* 108 (4 Jan. 2012), p. 045305. DOI: 10.1103/PhysRevLett.108.045305. URL: https://link.aps.org/doi/10.1103/PhysRevLett.108.045305.

[45] Thomas H. Barter et al. "Spatial coherence of a strongly interacting Bose gas in the trimerized kagome lattice". In: *Phys. Rev. A* 101 (1 Jan. 2020), p. 011601. DOI: 10.1103/PhysRevA.101.011601. URL: https://link.aps.org/doi/10.1103/PhysRevA.101.011601.

[46] Tsz-Him Leung et al. "Interaction-Enhanced Group Velocity of Bosons in the Flat Band of an Optical Kagome Lattice". In: *Phys. Rev. Lett.* 125 (13 Sept. 2020), p. 133001. DOI: 10.1103/PhysRevLett.125.133001. URL: https://link.aps.org/doi/10.1103/PhysRevLett.125.133001.

[47] Thomas H. Barter. "Quantum Simulation of the Bose-Hubbard Model with Ultracold Atoms in Triangular Optical Superlattices". PhD thesis. University of California, Berkeley, 2018.

[48] R. Walters et al. "Ab initio derivation of Hubbard models for cold atoms in optical lattices". In: *Phys. Rev. A* 87 (4 Apr. 2013), p. 043613. DOI: 10.1103/PhysRevA.87.043613. URL: https://link.aps.org/doi/10.1103/PhysRevA.87.043613.

[49] Jennie S. Guzman. "Explorations of Magnetic Phases in F=1 $^{87}RbSpinorCondensates$". PhD thesis. University of California, Berkeley, 2012.

[50] Claire K. Thomas. "Quantum Simulation of Triangular, Honeycomb and Kagome Crystal Structures using Ultracold Atoms in Lattices of Laser Light". PhD thesis. University of California, Berkeley, 2017.

[51] John Prodan et al. "Stopping Atoms with Laser Light". In: *Phys. Rev. Lett.* 54 (10 Mar. 1985), pp. 992–995. DOI: 10.1103/PhysRevLett.54.992. URL: https://link.aps.org/doi/10.1103/PhysRevLett.54.992.

[52] E. L. Raab et al. "Trapping of Neutral Sodium Atoms with Radiation Pressure". In: *Phys. Rev. Lett.* 59 (23 Dec. 1987), pp. 2631–2634. DOI: 10.1103/PhysRevLett.59.2631. URL: https://link.aps.org/doi/10.1103/PhysRevLett.59.2631.

[53] Y.-J. Lin et al. "Rapid production of ^{87}Rb Bose-Einstein condensates in a combined magnetic and optical potential". In: *Phys. Rev. A* 79 (6 June 2009), p. 063631. DOI: 10.1103/PhysRevA.79.063631. URL: https://link.aps.org/doi/10.1103/PhysRevA.79.063631.

[54] R. W. Boyd. *Nonlinear optics*. Second. Boston: Academic Press, 2003.

[55] Sergey V. Tovstonog, Sunao Kurimura, and Kenji Kitamura. "Continuous-Wave 2 W Green Light Generation in Periodically Poled Mg-Doped Stoichiometric Lithium Tantalate". In: *Japanese Journal of Applied Physics* 45.No. 34 (Aug. 2006), pp. L907–L909. DOI: 10.1143/jjap.45.l907. URL: https://doi.org/10.1143/JJAP.45.L907.

[56] F. J. Kontur et al. "Frequency-doubling of a CW fiber laser using PPKTP, PPMgSLT, and PPMgLN". In: *Opt. Express* 15.20 (Oct. 2007), pp. 12882–12889. DOI: 10.1364/OE.15.012882. URL: http://www.opticsexpress.org/abstract.cfm?URI=oe-15-20-12882.

[57] A. Browaeys et al. "Transport of atoms in a quantum conveyor belt". In: *Phys. Rev. A* 72 (5 Nov. 2005), p. 053605. DOI: 10.1103/PhysRevA.72.053605. URL: https://link.aps.org/doi/10.1103/PhysRevA.72.053605.

[58] D. O. Hogenboom et al. "Three-dimensional images generated by quadrature interferometry". In: *Opt. Lett.* 23.10 (May 1998), pp. 783–785. DOI: 10.1364/OL.23.000783. URL: http://ol.osa.org/abstract.cfm?URI=ol-23-10-783.

[59] Daniel O. Hogenboom and Charles A. DiMarzio. "Quadrature detection of a Doppler signal". In: *Appl. Opt.* 37.13 (May 1998), pp. 2569–2572. DOI: 10.1364/AO.37.002569. URL: http://ao.osa.org/abstract.cfm?URI=ao-37-13-2569.

[60] F. Mila. "Low-Energy Sector of the $S = 1/2$ Kagome Antiferromagnet". In: *Phys. Rev. Lett.* 81 (11 Sept. 1998), pp. 2356–2359. DOI: 10.1103/PhysRevLett.81.2356. URL: https://link.aps.org/doi/10.1103/PhysRevLett.81.2356.

[61] M. Mambrini and F. Mila. "RVB description of the low-energy singlets of the spin 1/2 kagoméantiferromagnet". In: *The European Physical Journal B - Condensed Matter and Complex Systems* 17.4 (2000), pp. 651–659. DOI: 10.1007/PL00011071. URL: https://doi.org/10.1007/PL00011071.

[62] Robert Schaffer et al. "Quantum spin liquid in a breathing kagome lattice". In: *Phys. Rev. B* 95 (5 Feb. 2017), p. 054410. DOI: 10.1103/PhysRevB.95.054410. URL: https://link.aps.org/doi/10.1103/PhysRevB.95.054410.

[63] L. Santos et al. "Atomic Quantum Gases in Kagomé Lattices". In: *Phys. Rev. Lett.* 93 (3 July 2004), p. 030601. DOI: 10.1103/PhysRevLett.93.030601. URL: https://link.aps.org/doi/10.1103/PhysRevLett.93.030601.

[64] B. Damski et al. "Atomic Fermi Gas in the Trimerized Kagomé Lattice at 2/3 Filling". In: *Phys. Rev. Lett.* 95 (6 Aug. 2005), p. 060403. DOI: 10.1103/PhysRevLett.95.060403. URL: https://link.aps.org/doi/10.1103/PhysRevLett.95.060403.

[65] B. Damski et al. "Quantum gases in trimerized kagomé lattices". In: *Phys. Rev. A* 72 (5 Nov. 2005), p. 053612. DOI: 10.1103/PhysRevA.72.053612. URL: https://link.aps.org/doi/10.1103/PhysRevA.72.053612.

[66] Farida H. Aidoudi et al. "An ionothermally prepared S = 1/2 vanadium oxyfluoride kagome lattice". In: *Nature Chemistry* 3.10 (2011), pp. 801–806. DOI: 10.1038/nchem.1129. URL: https://doi.org/10.1038/nchem.1129.

[67] L. Clark et al. "Gapless Spin Liquid Ground State in the S=1/2 Vanadium Oxyfluoride Kagome Antiferromagnet $[NH_4]_2[\mathbf{C}_7\mathbf{H}_{14}\mathbf{N}][\mathbf{V}_7\mathbf{O}_6\mathbf{F}_{18}]$". In: *Phys. Rev. Lett.* 110 (20 May 2013), p. 207208. DOI: 10.1103/PhysRevLett.110.207208. URL: https://link.aps.org/doi/10.1103/PhysRevLett.110.207208.

[68] Biao Wu and Qian Niu. "Nonlinear Landau-Zener tunneling". In: *Phys. Rev. A* 61 (2 Jan. 2000), p. 023402. DOI: 10.1103/PhysRevA.61.023402. URL: https://link.aps.org/doi/10.1103/PhysRevA.61.023402.

[69] Dmitri Diakonov et al. "Loop structure of the lowest Bloch band for a Bose-Einstein condensate". In: *Phys. Rev. A* 66 (1 July 2002), p. 013604. DOI: 10.1103/PhysRevA.66.013604. URL: https://link.aps.org/doi/10.1103/PhysRevA.66.013604.

[70] Biao Wu and Qian Niu. "Superfluidity of Bose–Einstein condensate in an optical lattice: Landau–Zener tunnelling and dynamical instability". In: *New Journal of Physics* 5 (July 2003), pp. 104–104. DOI: 10.1088/1367-2630/5/1/104. URL: https://doi.org/10.1088/1367-2630/5/1/104.

[71] Yu-Ao Chen et al. "Many-body Landau–Zener dynamics in coupled one-dimensional Bose liquids". In: *Nature Physics* 7.1 (2011), pp. 61–67. DOI: 10.1038/nphys1801. URL: https://doi.org/10.1038/nphys1801.

[72] Hoi-Yin Hui et al. "Loop-structure stability of a double-well-lattice Bose-Einstein condensate". In: *Phys. Rev. A* 86 (6 Dec. 2012), p. 063636. DOI: 10.1103/PhysRevA.86.063636. URL: https://link.aps.org/doi/10.1103/PhysRevA.86.063636.

[73] L. Fallani et al. "Optically Induced Lensing Effect on a Bose-Einstein Condensate Expanding in a Moving Lattice". In: *Phys. Rev. Lett.* 91 (24 Dec. 2003), p. 240405. DOI: 10.1103/PhysRevLett.91.240405. URL: https://link.aps.org/doi/10.1103/PhysRevLett.91.240405.

[74] B. Eiermann et al. "Dispersion Management for Atomic Matter Waves". In: *Phys. Rev. Lett.* 91 (6 Aug. 2003), p. 060402. DOI: 10.1103/PhysRevLett.91.060402. URL: https://link.aps.org/doi/10.1103/PhysRevLett.91.060402.

[75] D. Clément et al. "Exploring Correlated 1D Bose Gases from the Superfluid to the Mott-Insulator State by Inelastic Light Scattering". In: *Phys. Rev. Lett.* 102 (15 Apr. 2009), p. 155301. DOI: 10.1103/PhysRevLett.102.155301. URL: https://link.aps.org/doi/10.1103/PhysRevLett.102.155301.

[76] N. Fabbri et al. "Excitations of Bose-Einstein condensates in a one-dimensional periodic potential". In: *Phys. Rev. A* 79 (4 Apr. 2009), p. 043623. DOI: 10.1103/PhysRevA.79.043623. URL: https://link.aps.org/doi/10.1103/PhysRevA.79.043623.

[77] Philipp T. Ernst et al. "Probing superfluids in optical lattices by momentum-resolved Bragg spectroscopy". In: *Nature Physics* 6.1 (2010), pp. 56–61. DOI: 10.1038/nphys1476. URL: https://doi.org/10.1038/nphys1476.

[78] X Du et al. "Bragg spectroscopy of a superfluid Bose–Hubbard gas". In: *New Journal of Physics* 12.8 (Aug. 2010), p. 083025. DOI: 10.1088/1367-2630/12/8/083025. URL: https://doi.org/10.1088/1367-2630/12/8/083025.

[79] Christian Schori et al. "Excitations of a Superfluid in a Three-Dimensional Optical Lattice". In: *Phys. Rev. Lett.* 93 (24 Dec. 2004), p. 240402. DOI: 10.1103/PhysRevLett.93.240402. URL: https://link.aps.org/doi/10.1103/PhysRevLett.93.240402.

[80] O. Morsch et al. "Bloch Oscillations and Mean-Field Effects of Bose-Einstein Condensates in 1D Optical Lattices". In: *Phys. Rev. Lett.* 87 (14 Sept. 2001), p. 140402. DOI: 10.1103/PhysRevLett.87.140402. URL: https://link.aps.org/doi/10.1103/PhysRevLett.87.140402.

[81] M. Jona-Lasinio et al. "Asymmetric Landau-Zener Tunneling in a Periodic Potential". In: *Phys. Rev. Lett.* 91 (23 Dec. 2003), p. 230406. DOI: 10.1103/PhysRevLett.91.230406. URL: https://link.aps.org/doi/10.1103/PhysRevLett.91.230406.

[82] Q. Guan et al. "Nonexponential Tunneling due to Mean-Field-Induced Swallowtails". In: *Phys. Rev. Lett.* 125 (21 Nov. 2020), p. 213401. DOI: 10.1103/PhysRevLett.125.213401. URL: https://link.aps.org/doi/10.1103/PhysRevLett.125.213401.

[83] S. B. Koller et al. "Nonlinear looped band structure of Bose-Einstein condensates in an optical lattice". In: *Phys. Rev. A* 94 (6 Dec. 2016), p. 063634. DOI: 10.1103/PhysRevA.94.063634. URL: https://link.aps.org/doi/10.1103/PhysRevA.94.063634.

[84] Hideki Ozawa et al. "Interaction-Driven Shift and Distortion of a Flat Band in an Optical Lieb Lattice". In: *Phys. Rev. Lett.* 118 (17 Apr. 2017), p. 175301. DOI: 10.1103/PhysRevLett.118.175301. URL: https://link.aps.org/doi/10.1103/PhysRevLett.118.175301.

[85] S. Burger et al. "Superfluid and Dissipative Dynamics of a Bose-Einstein Condensate in a Periodic Optical Potential". In: *Phys. Rev. Lett.* 86 (20 May 2001), pp. 4447–4450. DOI: 10.1103/PhysRevLett.86.4447. URL: https://link.aps.org/doi/10.1103/PhysRevLett.86.4447.

[86] Biao Wu and Qian Niu. "Landau and dynamical instabilities of the superflow of Bose-Einstein condensates in optical lattices". In: *Phys. Rev. A* 64 (6 Nov. 2001), p. 061603. DOI: 10.1103/PhysRevA.64.061603. URL: https://link.aps.org/doi/10.1103/PhysRevA.64.061603.

[87] L. Fallani et al. "Observation of Dynamical Instability for a Bose-Einstein Condensate in a Moving 1D Optical Lattice". In: *Phys. Rev. Lett.* 93 (14 Sept. 2004), p. 140406. DOI: 10.1103/PhysRevLett.93.140406. URL: https://link.aps.org/doi/10.1103/PhysRevLett.93.140406.

[88] Gretchen K. Campbell et al. "Parametric Amplification of Scattered Atom Pairs". In: *Phys. Rev. Lett.* 96 (2 Jan. 2006), p. 020406. DOI: 10.1103/PhysRevLett.96.020406. URL: https://link.aps.org/doi/10.1103/PhysRevLett.96.020406.

[89] A. Isacsson and S. M. Girvin. "Multiflavor bosonic Hubbard models in the first excited Bloch band of an optical lattice". In: *Phys. Rev. A* 72 (5 Nov. 2005), p. 053604. DOI: 10.1103/PhysRevA.72.053604. URL: https://link.aps.org/doi/10.1103/PhysRevA.72.053604.

[90] I. B. Spielman et al. "Collisional deexcitation in a quasi-two-dimensional degenerate bosonic gas". In: *Phys. Rev. A* 73 (2 Feb. 2006), p. 020702. DOI: 10.1103/PhysRevA.73.020702. URL: https://link.aps.org/doi/10.1103/PhysRevA.73.020702.

[91] Torben Müller et al. "State Preparation and Dynamics of Ultracold Atoms in Higher Lattice Orbitals". In: *Phys. Rev. Lett.* 99 (20 Nov. 2007), p. 200405. DOI: 10.1103/PhysRevLett.99.200405. URL: https://link.aps.org/doi/10.1103/PhysRevLett.99.200405.

[92] Y. Castin and R. Dum. "Bose-Einstein Condensates in Time Dependent Traps". In: *Phys. Rev. Lett.* 77 (27 Dec. 1996), pp. 5315–5319. DOI: 10.1103/PhysRevLett.77.5315. URL: https://link.aps.org/doi/10.1103/PhysRevLett.77.5315.

[93] Georg Wirth, Matthias Ölschläger, and Andreas Hemmerich. "Evidence for orbital superfluidity in the P-band of a bipartite optical square lattice". In: *Nature Physics* 7.2 (2011), pp. 147–153. DOI: 10.1038/nphys1857. URL: https://doi.org/10.1038/nphys1857.

[94] L. Duca et al. "An Aharonov-Bohm interferometer for determining Bloch band topology". In: *Science* 347.6219 (2015), pp. 288–292. ISSN: 0036-8075. DOI: 10.1126/science.1259052. eprint: https://science.sciencemag.org/content/347/6219/288.full.pdf. URL: https://science.sciencemag.org/content/347/6219/288.

[95] Gregor Jotzu et al. "Experimental realization of the topological Haldane model with ultracold fermions". In: *Nature* 515.7526 (2014), pp. 237–240. DOI: 10.1038/nature13915. URL: https://doi.org/10.1038/nature13915.

[96] Kai Sun et al. "Topological Insulators and Nematic Phases from Spontaneous Symmetry Breaking in 2D Fermi Systems with a Quadratic Band Crossing". In: *Phys. Rev. Lett.* 103 (4 July 2009), p. 046811. DOI: 10.1103/PhysRevLett.103.046811. URL: https://link.aps.org/doi/10.1103/PhysRevLett.103.046811.

[97] Stefan Uebelacker and Carsten Honerkamp. "Instabilities of quadratic band crossing points". In: *Phys. Rev. B* 84 (20 Nov. 2011), p. 205122. DOI: 10.1103/PhysRevB.84.205122. URL: https://link.aps.org/doi/10.1103/PhysRevB.84.205122.

[98] Liang Du, Xiaoting Zhou, and Gregory A. Fiete. In: *Phys. Rev. B* 95 (3 Jan. 2017), p. 035136. DOI: 10.1103/PhysRevB.95.035136. URL: https://link.aps.org/doi/10.1103/PhysRevB.95.035136.

[99] Jun-Won Rhim, Kyoo Kim, and Bohm-Jung Yang. "Quantum distance and anomalous Landau levels of flat bands". In: *Nature* 584.7819 (2020), pp. 59–63. DOI: 10.1038/s41586-020-2540-1. URL: https://doi.org/10.1038/s41586-020-2540-1.

[100] A. H. Castro Neto et al. "The electronic properties of graphene". In: *Rev. Mod. Phys.* 81 (1 Jan. 2009), pp. 109–162. DOI: 10.1103/RevModPhys.81.109. URL: https://link.aps.org/doi/10.1103/RevModPhys.81.109.

[101] Shintaro Taie et al. "Spatial adiabatic passage of massive quantum particles in an optical Lieb lattice". In: *Nature Communications* 11.257 (Jan. 2020). DOI: 10.1038/s41467-019-14165-3. URL: https://www.nature.com/articles/s41467-019-14165-3.